Master's thesis

NTNU
Norwegian University of Science and Technology
Faculty of Information Technology and Electrical Engineering
Department of Electric Power Engineering

Samuel Oladeji
Kazi Shoffiuddin Roni

Active Front End Converter with Virtual Damping and Inertia

Master's thesis in Renewable Energy in the Marine Environment
Supervisor: Roy Nilsen
June 2022

NTNU
Norwegian University of Science and Technology

Samuel Oladeji
Kazi Shoffiuddin Roni

Active Front End Converter with Virtual Damping and Inertia

Master's thesis in Renewable Energy in the Marine Environment
Supervisor: Roy Nilsen
June 2022

Norwegian University of Science and Technology
Faculty of Information Technology and Electrical Engineering
Department of Electric Power Engineering

NTNU
Norwegian University of
Science and Technology

ABSTRACT

Recently, power networks are advancing from synchronous machine-based systems to converter-control systems, with a high proliferation of renewable energy sources (RESs) such as wind and solar photovoltaic sources. The present-day RESs devices comprise a significant proportion of the generation, and the conventional method of making these sources follow the grid can cause frequency instability. In literature, different strategies have been deployed for emulating virtual synchronous machines in voltage source inverters to manage frequency events and maintain grid stability. However, this master thesis investigates the implementation of the latest virtual inertia control techniques in an Active Front End Converter with damping. The implementation was conducted in various coordinate systems to comprehend research methods and explore challenges. Through literature review and several simulations, it has been established that the virtual inertia machine's desired frequency response can be obtained by balancing the frequency, voltage, and phase across the filter capacitor with that of the grid. Also, the appropriate frequency response was achieved through time constants, damping coefficients, and inertia constants. In the cases considered, active power was delivered during grid-connected, islanding, and under/over frequency operations. The system's functionality depended on the designed control architecture and mimicking the dynamics of a synchronous machine. A discussion of the results and challenges of the integration of virtual inertia control for the Active Front End converter is accomplished.

Sammendrag

Nylig har kraftnettverk utviklet seg fra synkrone maskinbaserte systemer til omformer-kontrollsystemer, med en høy spredning av fornybare energikilder (RES) som vind- og solcellekilder. Dagens RESs-enheter utgjør en betydelig andel av generasjonen, og den konvensjonelle metoden for å få disse kildene til å følge nettet kan forårsake frekvensustabilitet. I litteraturen har forskjellige strategier blitt brukt for å emulere virtuelle synkrone maskiner i spenningskildeomformere for å håndtere frekvenshendelser og opprettholde nettstabilitet. Denne masteroppgaven undersøker imidlertid implementeringen av de nyeste virtuelle treghetkontrollteknikkene i en Active Front End Converter med demping. Implementeringen ble gjennomført i ulike koordinatsystemer for å forstå forskningsmetoder og utforske utfordringer. Gjennom litteraturgjennomgang og flere simuleringer er det fastslått at den virtuelle treghetsmaskinens ønskede frekvensrespons kan oppnås ved å balansere frekvens, spenning og fase over filterkondensatoren med nettets. Den passende frekvensresponsen ble også oppnådd gjennom tidskonstanter, dempningskoeffisienter og treghetskonstanter. I de vurderte tilfellene ble det levert aktiv kraft under netttilkoblede, øy- og under-/overfrekvensdrift. Systemets funksjonalitet var avhengig av den utformede kontrollarkitekturen og etterligningen av dynamikken til en synkron maskin. En diskusjon av resultatene og utfordringene ved integreringen av virtuell treghetkontroll for Active Front End-omformeren er gjennomført.

PREFACE

The research understudied in this write-up was conducted under some constraints and unforeseen contingencies. The Active Front End Converter with virtual inertia and damping was meant to have been done using a processor board and Xilinx software. However, it was postponed due to internal considerations and decisions made within the department. The work has been under the supervision of Roy Nilsen from the Department of Electrical Power Engineering. Also, initial simulations were meant to have been handled in the 2021 Autumn semester, but the research students in question are exchange students, which posed some limitations. More so, the entire research team tested positive for COVID-19 in February 2022, which affected the research progress. We would like to show our sincere appreciation to our supervisor Roy Nilsen for the tremendous guidance in completing this thesis.

Table of contents

Contents

Chapter 7

List of Figures

List of Tables

List of Abbreviations and Symbols

PV	Photo Voltaic
RES	Renewable Energy Sources
AFE	Active Front End
$TSOS/DSOS$	Transmission system operator / Distribution system operators
RoCoF	Rate of Change of Frequency
VISMA	Virtual Synchronous Machine
SG	Synchronous Generator
P_m	Mechanical Power
f_0	Rated frequency
K_D	Damping Coefficient
ω_r	Angular velocity
ω_0	Rated angular velocity
δ	Rotor angle, phase of the angle
n	The speed of the rotor
T_m	Mechanical time constant
ω_n	Nominal angular velocity
f_s	Reference frequency
i_{ref}^*	Current reference
PLL	Phase Locked Loop
PID	Proportional-Integral-Derivative
THD	Total Harmonic Distortion
m_p	Proportional coefficient
m_d	Derivative coefficient
n_d	Derivative coefficient of reactive power
i_0	Inverter output current
v_0	Inverter output voltage
LPF	Low Pass Filter
HPF	High Pass Filter
VSC	Voltage Source Converter
k_d	Derivative constant
k_p	Proportional constant
T_i	Integral time constant
β	Damping factor
T_{sum}	Time constant
RFT	Reference frame theory
DC	Direct Current
$BESS$	Battery energy storage system
ASD	Adjustable speed drive
$IGBT$	Insulated gate bipolar transistor
V_{dc}	DC Voltage
V_{m1}	Fundamental peak phase voltage
m_f	Modulation frequency index
f_{cr}	Carrier frequency
f_s	Reference frequency to calculate modulation frequency index
m_a	Amplitude modulation index
PWM	Pulse width modulation
δ	phase angle between the converter and the point of common coupling

$SPWM$	Sinusoidal pulse width modulation
PCC	Point of common coupling
w	Angular speed
V_{ref_peak}	Peak reference voltage amplitude
V_{cr_peak}	Peak carrier voltage amplitude
PD	Phase detector
θ_g	Grid angle
SRF	Synchronous reference frame
V_a^*	Phase A reference voltage signal for SPWM operation
V_b^*	Phase B reference voltage signal for SPWM operation
V_c^*	Phase C reference voltage signal for SPWM operation
V_{mA}	Phase A modulating voltage signal for SPWM operation
V_{mB}	Phase B modulating voltage signal for SPWM operation
V_{mC}	Phase C modulating voltage signal for SPWM operation
C	Capacitance
P_R	Rated Power of the Converter
w_1	Angular frequency at fundamental frequency
V_N	Rated voltage
I_N	Rated Current
L_1	Converter side inductor of an LCL filter
L_2	Grid side inductor of an LCL filter plus grid inductance
L_g	Grid inductance
K_{res}	Resonant factor of an LCL filter
f_{res}	Resonant frequency
ω_{res}	Resonant angular frequency
L_s	Line Inductance
C_f	Filter capacitor
e_{af}	Internal voltage of the synchronous machine
$\underline{u_c^s}$	Filter capacitor voltage in stator coordinate system
x_c	Filter capacitor impedance
U_{dc}	DC Link voltage
δ_c^s	Capacitor voltage angle
$f_{\_ref}$, f_{sref}	frequency set point which determines how much power will be delivered
ω_N	Nominal angular frequency
RoCoF	Rate of Change of Frequency

Chapter 1

1.0 Introduction

1.1 Theoretical Background of Virtual Inertia

In modern power systems, the need to utilize clean energy sources for industrial and residential consumption is rapidly increasing owing to some determinants such as fuel costs, laws, and regulatory frameworks. There is a trend of high proliferation of renewable energy sources (RESs) like solar PV and wind in generation systems which are replacing conventional sources like coal and nuclear power plants. The integration of RESs into the present energy mix is done to achieve a just energy transition and carbon footprint reduction. Since 2015 the global wind energy and PV generation capacity are more that 0.4TW and 0.2 TW respectively [1]. Countries like Denmark, Ireland and Germany have renewable energy penetrations capacity between 20% to 40%. In Norway, wind power accounts for 10% in production capacity and it is said to dominate the energy stream in the coming years [2]. With the high-speed development of offshore wind projects such as the Hywind Tampen, power grids are gravitating towards converter-dominated technologies from rotational generator-based systems, as depicted in Figure 1. The connection of Solar PV systems and wind turbines to utility networks are achieved through inverters. Despite the numerous benefits of these non-depleting energy sources, the inverter-based generation has no mechanical inertia response feature, and thus jeopardizes frequency stability [3]–[5].

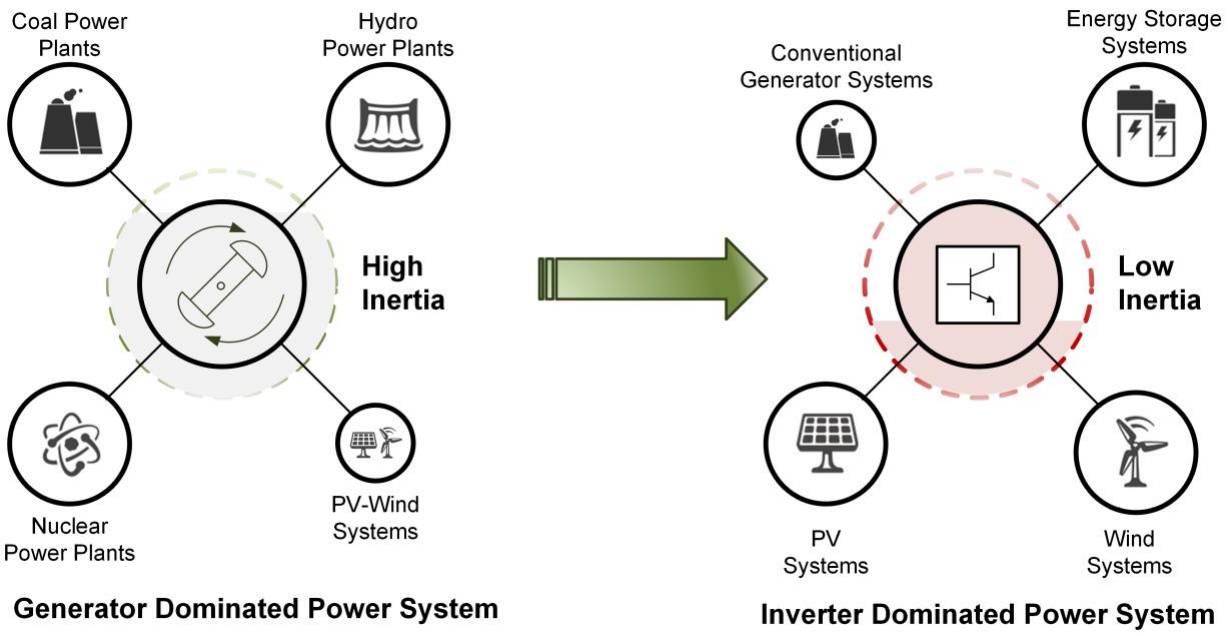

Figure 1: Progression towards an inverter dominated power system [1]

The dramatic change in modern power networks due to the intermittent nature of inverter-based generation, and sudden load fluctuations have created a shortage of inertia. Earlier on, power system inertia supplied by the rotational masses of synchronous generators is becoming less available to maintain stability. However, a heavy presence of inertia in power systems, i.e., substantial kinetic buffer, is commonly solicited for minimizing the frequency changes, which can curtail the impacts of unnecessary load-shedding, cascading failures, or large-scale blackouts during frequency scenarios [6], [7].

Recent studies have hinted the problem of low-inertia and emphasis have been laid on the importance of maintaining frequency stability with increasing absence of inertia response from RESs. For instance, concerns have been raised by the Electricity Reliability Council of Texas (ERCOT) about continuous decline in the inertia response and possible solutions to mitigate this challenge. [8] points out the increase in ratio of frequency changes to power production loss on an annual basis because of RESs concentration. Likewise, the European Network of Transmission System Operators for Electricity (ENTSO-E) have flagged destabilizing effects of frequency volatility and suggested frequency containment strategies in the Nordic grid [9]. The frequency stability of power systems is dependent on the balance of active power between consumption and generation. Large amounts of RESs penetration pose a threat to the reliability of power grids, and it is usually the underlying inducement for frequency and voltage unreliability [10].

As mentioned earlier, the reliability of power systems rest on the capacity of TSOs/DSOs to maintain equilibrium between power generation and load variations. This can be achieved by the implementation of various control actions over multiple time intervals as shown in Figure 2. In the occurrence of any frequency event, the governor response is the primary control action that is activated within the first few seconds (usually 10-30s) to minimize the frequency deviation. If the deviation persists between 10-30 minutes, the automatic generation/secondary control takes action to restore the system frequency to the nominal value. The tertiary control action represents the reserve restoration capable of handling current and future disturbances in the system. In the case of a shift in power systems equilibrium, generators connected give slow response to adjust the imbalance. The kinetic buffer in the rotors is used for offsetting this unbalance via inertial response until the primary frequency control takes over. The displacement of synchronous generators in the power systems by RESs, diminishes the inertia response. This results to an increased rate-of-change-of-frequency (ROCOF), and a low frequency nadir (lowest frequency point) in a very short time. At this time (typically 10s), the primary frequency control is incapacitated to give any suitable response to limit the system frequency change. This timeframe is highlighted as section AB in Figure 2. It can be deduced from the Figure 2 that in systems with reduced inertia, the frequency nadir is consistently lower along with a high ROCOF. Such scenarios can result to tripping of frequency relays (creating under-frequency load shedding (UFLS) and, in the worst circumstances, may eventually cause cascaded outages [11], [12]. An effective approach to resolving this problem is to integrate virtual inertia in the system. The minimum requirement of a virtual inertia is to operate within a short duration (approximately lower than 10s) in an autonomous manner. The deployment of virtual inertia will compensate for the challenges created by increased RESs penetration, hence enhance the power system stability.

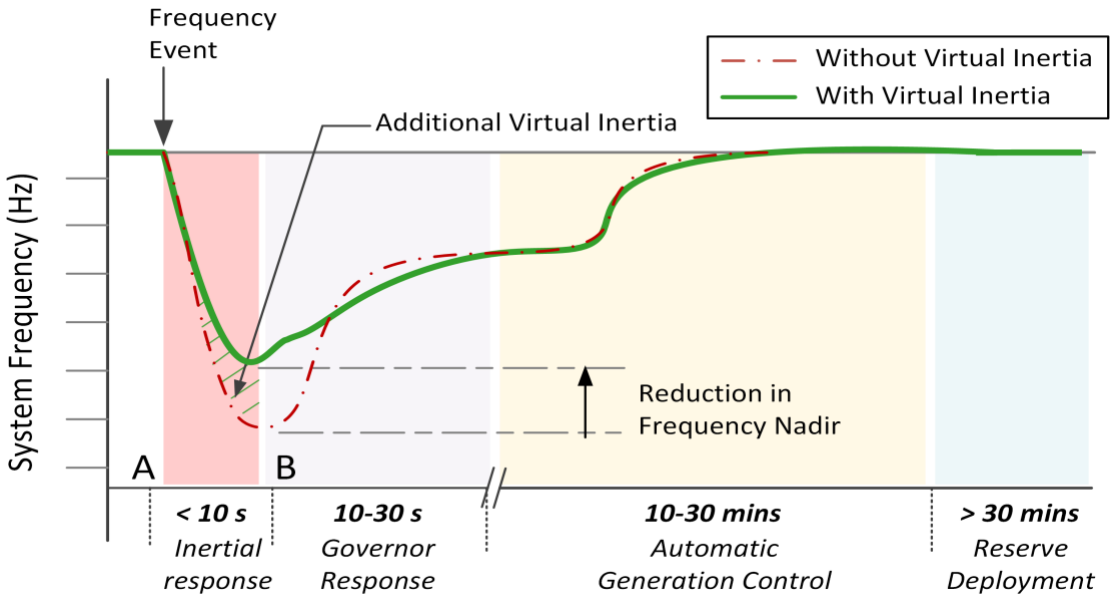

Figure 2: Multiple time-frame frequency response in a power system following a frequency event. [1]

However, the Nordic territory, particularly the Nordic Synchronous Area (NSA) has a roadmap of integrating large proportions of wind energy and European grid (ENSTO-E) into grid networks and ensuring flexible operation in transmission of power. This interconnection would increase the proliferation of renewable sources into the existing energy mix- hydropower plants, and pumped storage technology.

To achieve this RESs integration with virtual inertia response, various facets of these converter-based technology are being understudied at NTNU to support pump storage power plants.

«For some high-power applications, for instance, in Adjustable Speed Hydro (ASH), Active Front End Converters are used as grid-connected converters. This project is a part of the HydroCen project. The drive should operate both in generation mode and in pump mode (pump storage plant). This project is a continuation of a Master-project about an AFE. The same converter topology is used in Marine Drives and Off-shore Wind Turbine applications. The synchronous generator is controlled by an inverter and is feeding power into the DC-link. The AFE is a similar converter with an LCL filter connected to the AC grid, feeding the AC grid from the DC-link. The control of the AFE should include AC voltage and frequency droop, as well as virtual damping and inertia effects. This means that the AFE should behave as a generator in the AC grid. »

The Active Front End Converters are segments of frequency converters used in variable speed technologies. The presence of the DC-link allows the converter to be connected to variable speed generators by rectifying converters as shown in Figure 3.

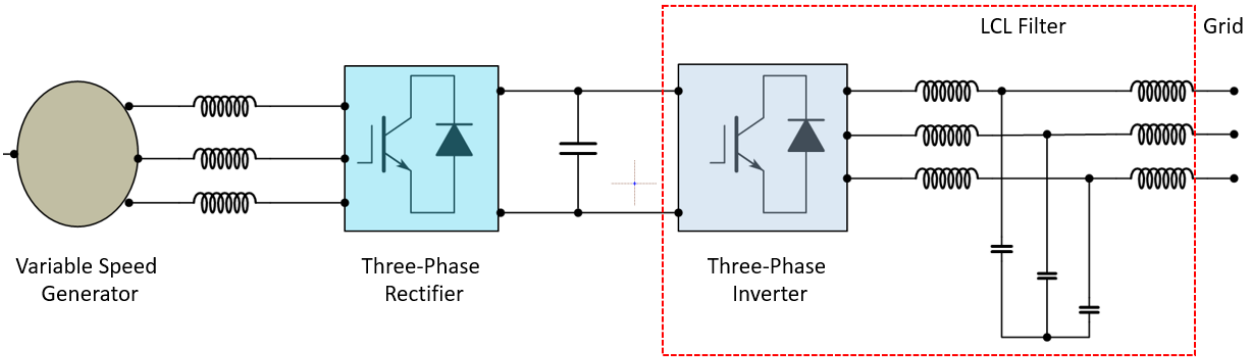

Figure 3: Full Frequency Converter.

The full frequency converter is used alongside variable-speed turbines which consist of the generation or motor side and grid side converters. The machine side is responsible for variations in the speed of the generator that supplies power to the DC bus, whereas the converter in charge of the grid inverts the power from the DC link to an AC grid signal/frequency which is sent to the main grid.

The machine side converter of the Adjustable Speed Hydro (ASH) ensures generator or motor mode operation at various rotational speeds which provides the flexibility of operation in either generation or pumping mode. At the rated head and specified frequency, Hydropower turbines perform optimally, and efficiency declines should there be adjustments to the head or frequency. The speed variations offer flexibility towards supplying the power plant with energy or deploying the energy for pumping operations at increased efficiency and heads below the rated value.

The grid side converter caters for the utility grid. The robustness of any electricity grid at any given time is highly dependent on the operation of the grid side. Hence, the investigation of its dynamic performance is of utmost interest if Norway is to achieve a stronger grid with wind energy prevalence.

As earlier stated, the AFE converts the DC link power into AC power which is made possible by the switching operations in the inverter. These operations are enabled by the control mechanisms designed to model the varying characteristics of the AFE.

The control of the AFE comprises of control loops, which include:

- Inner Current Control Loop, made up of a hysteresis current controller
- Voltage control (Amplitude and Angle), made up of PI controllers
- Outer Control Loops, which contain supplementary functions such as virtual impedance, active and reactive power frequency droop, harmonic compensation, synthetic inertia, unbalance control and so on.

1.2 Overview of the Master Thesis

In this research, the current and voltage controllers of the Inductor – capacitor – Inductor type inverter which is also referred as Active Front End converter have been studied, with specifications in the tuning of the controllers in $\alpha\beta 0$ and polar coordinates for stable operations, bearing in mind that the control mechanism should be adjusted to different variations in the system frequency that might arise due to grid perturbation.

Also, an emulation of the virtual inertia control with damping was implemented for the AFE. The tuning of the controllers was achieved by means of symmetrical optimum control procedure. The acceptability of the proposed methodology has been evaluated by means of simulations.

1.3 Master Thesis Report Outline

Section 2 gives the theoretical background of the control strategies for the implementation of the virtual inertia. It also discusses the different topologies for Virtual inertia, and typical droop control. A mathematical prove to show the similarities between droop control for microgrids and virtual synchronous machine (VSM) has been done in this section. Furthermore, it elaborates an alternative method for virtual synchronous machine through modified droop control. In addition to that a literature review of the tuning methodology for PI controllers was discussed.

Section 3 explains the literature review for modelling of Active Front End converter with LCL filters and its operation in different reference frames. Also, the proposed method of damping oscillations in the system is discussed.

Section 4 presents the methodology for filter capacitor in relation with Synchronous generator and a simple modelling of virtual synchronous machine in Simulink.

Section 5 presents the control loops for AFE with virtual inertia and damping implemented in Simulink and synchronization unit. Also, Symmetrical optimum approach for the tuning of the voltage amplitude and angle PI Controllers.

Section 6 presents the result of the simulations done in $\alpha\beta 0$ and dq control for different scenarios such as grid connected and Islanded mode. Also, the behavior of the Virtual Synchronous Machine has been analyzed in different grid frequency events.

Section 7 is the conclusion of this thesis and the recommendations for future study that can be implemented for the operation of AFE.

Chapter 2

2.0 control strategies for implementation of virtual inertia

The increasing penetration of renewable energy sources in the power systems decreases the overall system inertia. As power electronics-based devices have no rotating mass, they cannot provide inertia support inherently like a traditional SG (Synchronous Generator) does [13]. Inertia is closely related to the frequency stability of the system [3], [4], [14]. From Figure 4 the interdependency of inertia and frequency stability can be seen; frequency nadir is lower for a lower inertia system. Therefore, to continuously integrate renewable energy sources in power systems a new control strategy is developed which will virtually provide the inertia support. This virtual inertia control concept provides virtual inertia using an inverter, energy storage system and effective control. This entirety is also known as a virtual synchronous generator (VSG) [15] or synchronverter, Virtual synchronous machine (VISMA). All these topologies are designed for a common objective: to feed extra inertia into energy systems.

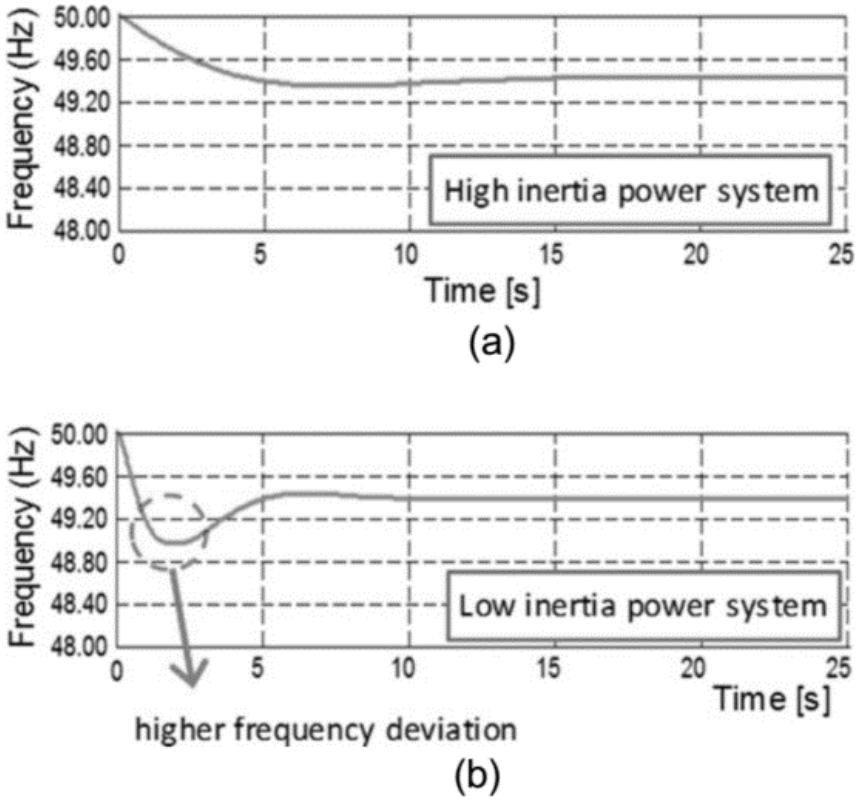

Figure 4: a) Response to frequency event in high inertia power system and (b) low inertia power system. [16]

To emulate virtual inertia there are several topologies available and it is summarized in [1], [17]. Figure 5 shows the available topologies for virtual inertia. The main objective of these topologies is to provide virtual inertia through power electronics control. In general, the energy source for virtual inertia is the energy storage system, but wind turbines can also be used as the energy source for virtual inertia; in that case, the virtual inertia will be referred to as synthetic inertia.

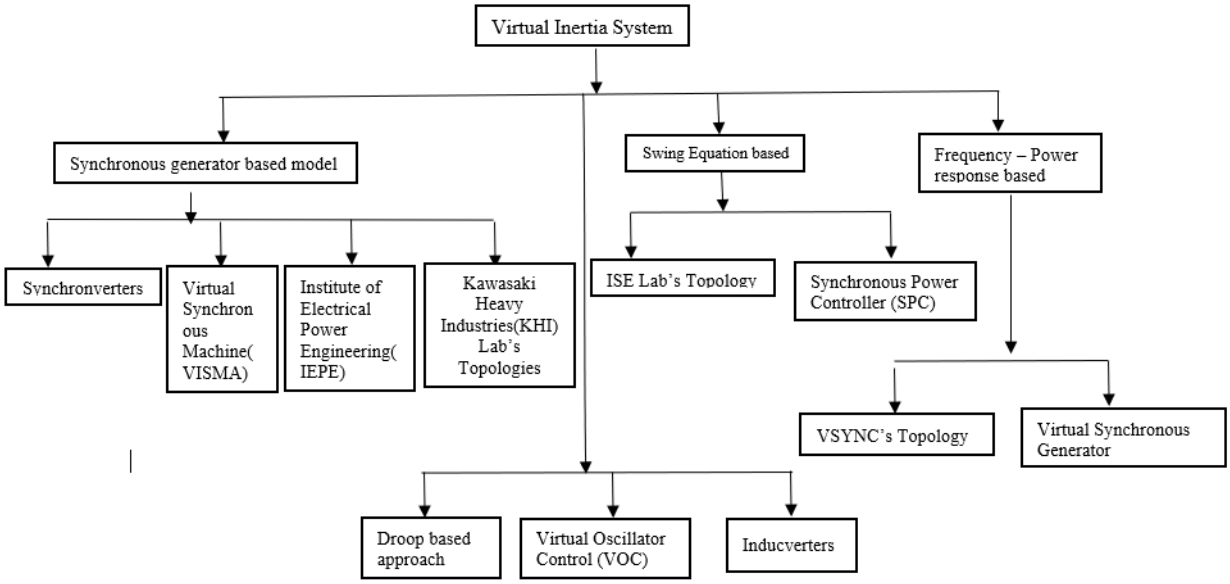

Figure 5:Different Topologies used for virtual inertia. [16]

However, the three main topologies for virtual inertia emulation are briefly discussed below, and their control mechanisms are elaborated in subsequent sections:

Synchronous Generator Model-Based Topology: In this topology, the whole dynamics of the synchronous generator are modelled to provide virtual inertia. The electrical and mechanical parts of the SG are modelled so that the dynamics of the generator are perfectly replicated.

Swing Equation Topology: The virtual inertia is provided using the swing equation in this topology. Here only the swing equation is implemented rather than the modelling of the full dynamics of the SG. The functionality of this topology is according to the measurement of the active power output of the inverter and grid frequency.

Frequency-Power Response-Based Topology: In this topology, the frequency response change is used to emulate virtual inertia. It measures the derivative of the frequency change to provide virtual inertia.

2.1 Virtual Synchronous Machine

The concept of the VSM is to emulate the essential behavior of a real SM, which can be actualized through the control of the frequency converter. In essence, the VSM concept is a mathematical representation of an actual synchronous machine (SM). The model of SM and choice of its parameters is arbitrary and can be specified by design requirements. Nevertheless, the standard features of a VSM are an emulation of virtual inertia and damping of the electromechanical oscillations. Additional features like the transient and sub-transient dynamics can also be added or eliminated based on the intended level of complexity and reliability in implementing the SM dynamics. To achieve a full dynamic of a synchronous machine in VSM model, the entire order model of the SM must be implemented in the converter control system. A full order SM is a combination of 5th order electrical model with stator winding represented in d-q co-ordinates, field, and damper windings with a 2nd order mechanical model hence, making up a 7th order model [16].

When the goal is to provide only virtual inertia and damping, the modelling of a full order SM will make the control algorithm complex [18]. The swing equation can be implemented to avoid complexity as both the inertia and damping are presented in equation 1 [19]. The virtual inertia and damping control are the implementations of the traditional swing equation of the SG unit in the control of the inverter. The swing equation is;

$$P_m - P_e = P_a = \frac{2Jd^2\delta}{w_0 dt^2} = \frac{2J}{w0}\frac{d\Delta w_r}{dt} \tag{1}$$

Here P_m denotes the per-unit input mechanical power, P_e is the electrical power output in p.u., P_a is the acceleration power in p.u., J is the system inertia constant in MW.s/ MVA, w_0 is the rated angular velocity of the rotor in rad/s, w_r is the angular velocity of the rotor in rad/s, δ is the rotor angle in rad and t is the time in seconds. P_m is the power supplied by the synchronous generator and P_e is the power demanded by the load. If the damping term is added with the swing equation, then it becomes,

$$P_m - P_e = \frac{2J}{w0}\frac{d\Delta w_r}{dt} + K_D\frac{\Delta w_r}{w_0} \tag{2}$$

Here K_D is the damping coefficient. The swing equation can also be represented in terms of frequency (Hz)

$$P_m - P_e = \frac{2J}{f_0}\frac{d\Delta f}{dt} + K_D\frac{\Delta f}{f_0} \tag{3}$$

Here f_0 is the rated frequency of the power system in Hz and f is the frequency of the power system in Hz. $\frac{d\Delta f}{dt}$ is the rate of change of frequency (RoCof) of the system. The active power and the angular rotor velocity of an SG is closely related to each other in the swing equation. The swing equation is also corelated with the frequency of the system because $\frac{d^2\delta}{dt^2}$ term is the

rate of change of system frequency or the angular rotor velocity of the system. The frequency can increase or decrease depending on the mechanical and electrical power balance in the swing equation. The acceleration power is positive if the difference between mechanical and electrical power is positive, which increases the system frequency. The system frequency will drop if the difference is negative. In a traditional SG power system, the frequency is maintained by controlling the generation and load balance using a speed governing system in the synchronous generator unit [16]. If the swing equation is represented in terms of torque and frequency, it can be expressed as;

$$T_m \cdot s \cdot w_n + d_{DQ}(w_n - w_{grid}) = \tau_{turbin} - \tau_{e,g} \tag{4}$$

The integral of the frequency w_n will give the virtual rotor angular position of the VSM. This rotor angular position is the phase angle of the VSM model induced voltage. The equation then can be written in terms of rotor angle,

$$T_m \cdot \frac{dn}{dt} + \frac{d_{DQ}}{w_n} \cdot \frac{d\delta}{dt} = \tau_{turbin} - \tau_{e,g} \tag{5}$$

Here,

$$\frac{d\delta}{dt} = w_n(n - f_s) \tag{6}$$

In the equation 6 above, n is the frequency or rotor speed, T_m is the mechanical time constant, δ is the phase angle of the VSM voltage, w_n is the nominal angular frequency of the system, f_s is the reference frequency.

A lower-order electrical SM model or a separate reactive power control loop can be used for the amplitude of the VSM. The VSM active power is coupled with the frequency or speed and angular position of the virtual inertia with respect to the grid voltage. Hence the reactive power or the voltage control of the VSM is decoupled from the virtual inertia emulation.

Figure 6 depicts a simple representation Virtual inertia.

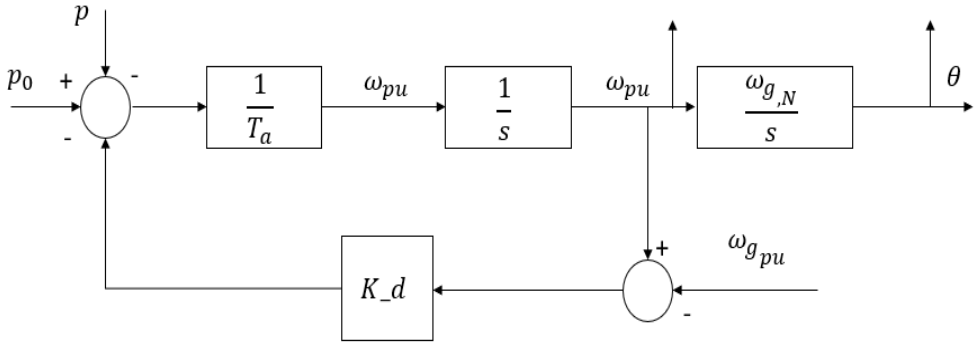

Figure 6: Inertia Emulation of VSM. [20]

2.2 Virtual Synchronous Machine Control Schemes

The VSM model will generate reference signals that need to be translated into gate signals for the converter through some additional controllers. Several control techniques [20] available, out of which three mains control techniques will be discussed here in this literature.

2.2.1 Current References from the SM model

In this scheme, the SM model generates the current reference i^*. A high-order electrical model of the SM can be implemented as it measures the voltage at the converter to the grid. The measured voltage can feed a simulation model by calculating currents, a replica in a real SM. This concept applied in the VISMA which was the very fast proposal for VSM implementation [21]. Below is the block diagram for this approach.

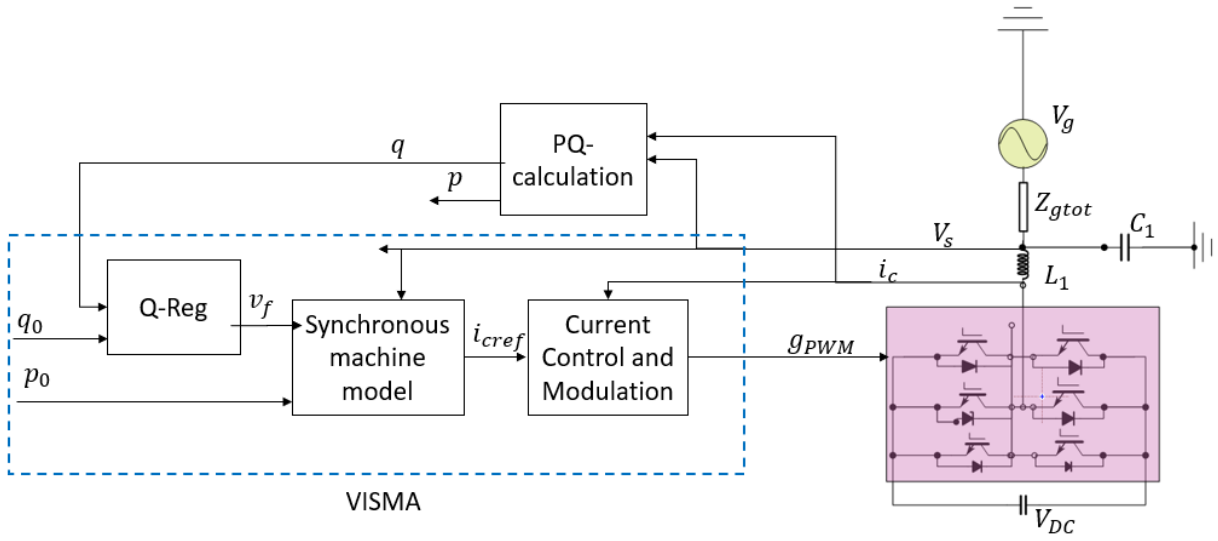

Figure 7: Visma Concept based on [21].

The current reference from the VSM will enter the current controller and that current controller can be a hysteresis current controller, PI- controllers [22] or any other traditional current controller. The current controllers can be in the stationary or synchronous reference frames. The current controllers, in general, can be tuned easily. At the same time, the saturation and limitations can be executed on the i^*, but this control scheme unsuitable for numerical stability for high-order SM models. This limitation requires extensive research to identify the root of this stability problem which has not been done yet. Also, practical discrete-time implementation of this control system requires special attention.

2.2.2 Voltage References from the SM model

As discussed in [23] the modelled SM will provide a voltage reference output in this control approach; here the voltage and current outputs were compared in the VISMA concept. If the implemented SM model is in reduced order, then the power flow is principally tied with the

inertia emulation, and the swing equation gives the phase angle. The amplitude of the voltage and the reactive power can be treated separately. This is shown in the below figures where the amplitude of the voltage comes from the reactive power control loop and the frequency and the phase angle of the VSM comes from the swing equation. Figure 8 is the simplest form of the VSM as the amplitude of the voltage and phase angle feed for PWM gate signals. The design of the synchronverter in [24] adopted this approach. However, this structure cannot readily and openly specify restrictions or controlled saturation of the converter's voltages and currents. At the hardware level, the protections can be implemented. The protections can also be implemented in parallel control loops, ignoring the references from the VSM. Still, in both cases, their reciprocation with the emulated inertia and reactive power control will be difficult to predict.

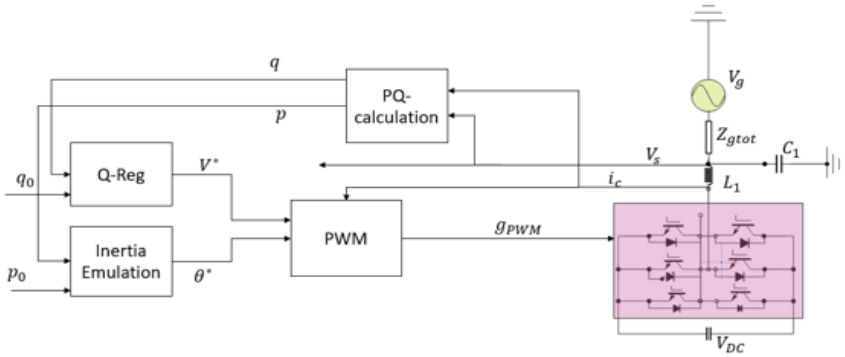

a) VSM with open Loop PWM control

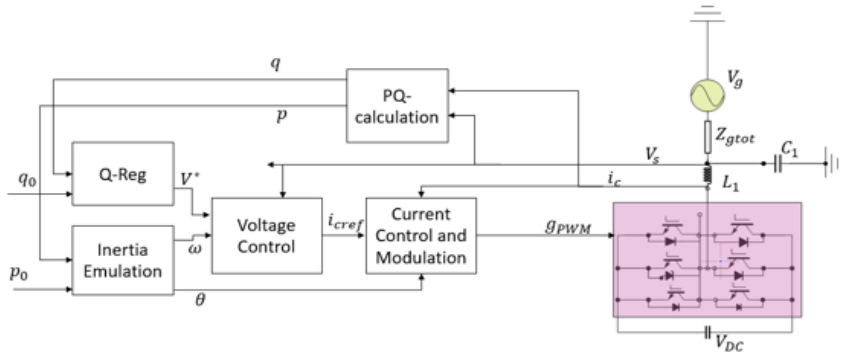

b) VSM with cascaded control

Figure 8: VSM open and cascaded controls.[20]

Furthermore, the controllability of the open-loop PWM control can be improved by using a traditional cascaded control method, in which the output voltage from the VSM serves as the reference for an external voltage loop cascaded with an internal current loop see Figure 8. Because both currents and voltages can be regulated by saturating the regulator's outputs, this technique provides more flexibility for integrating protective mechanisms. These control strategies are becoming more popular for controlling the microgrid. The droop controllers are responsible for providing voltage and current references [25]. The tuning for the controllers in this scheme is tough because of its cascaded control loops.

2.2.3 Power reference from the SM model

Another control approach for inertia emulation is tracking of the grid frequency rather than using a complete or lower order SM model. Figure 9 shows the control structure. The current reference for a particular power reference can be calculated from the measured grid voltage. This inertia emulation scheme can be combined for any current-controlled operation of the converters. The scheme has been used in the European Union VSYNC project because of its simplicity. This scheme needs a Phase-Locked Loop (PLL) to synchronize with the grid. Also, it requires an external grid with rotating inertia for synchronization. As a result, operation in fragile grids can be risky, and the control system will lack any intrinsic capability for black-start or islanded operations.

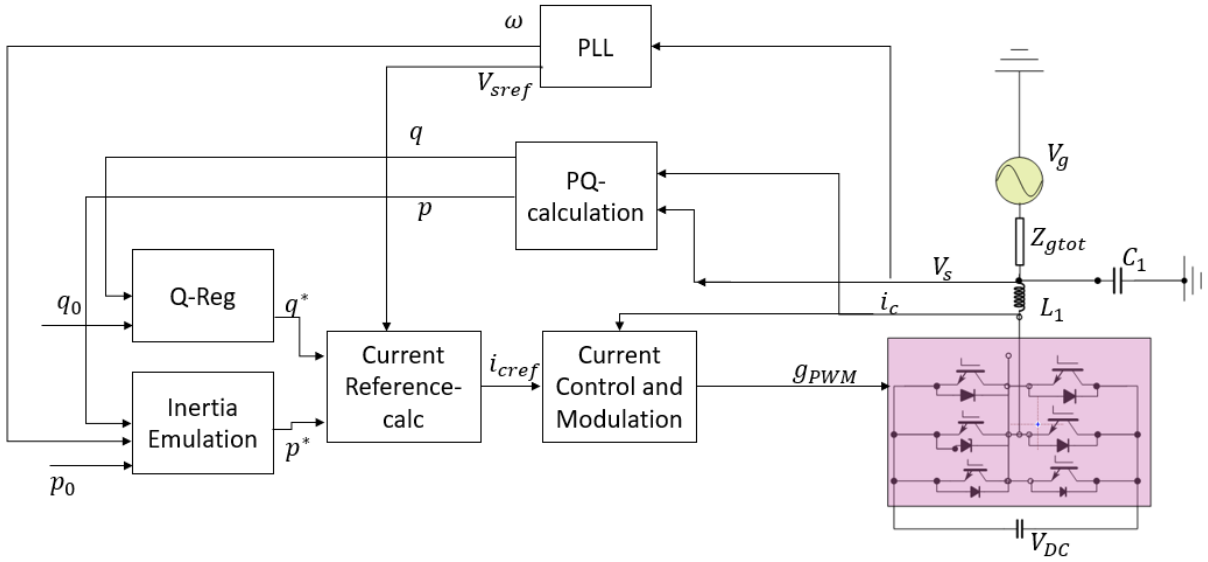

Figure 9: VSM with Power reference control scheme. [20]

2.3 Droop control

VSM has the advantage of load sharing in parallel connected units, with an intrinsic ability for stand-alone and microgrid operations. Among all the proposed control structures for microgrid operations, the droop controls for active and reactive power (Equation 7 and 8) is the easiest and most popular strategy [25].

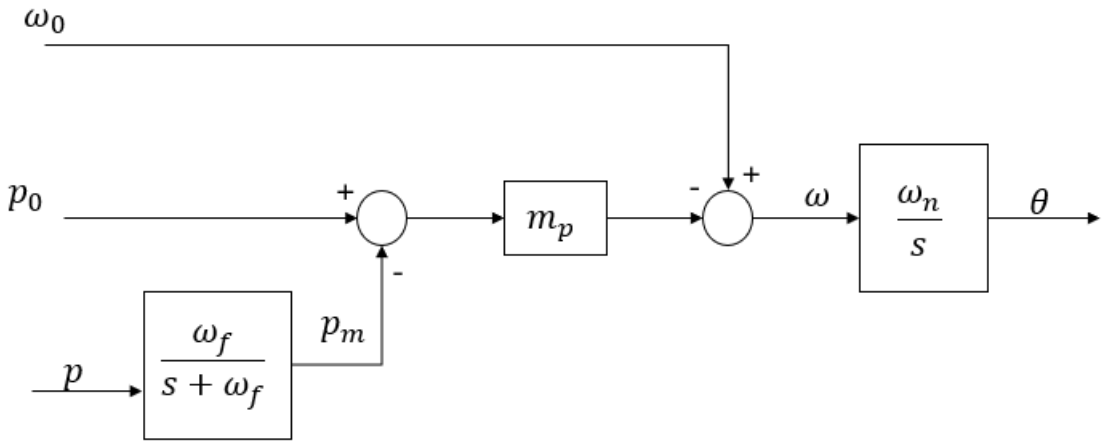

Figure 10:Active power droop control for Microgrid [20]**.**

$$\omega^*_{n,pu} = \omega_{grid,pu} - m_p\,(p_m - p_0) \qquad \theta = \frac{1}{s}\omega^*_{n,pu} \tag{7}$$

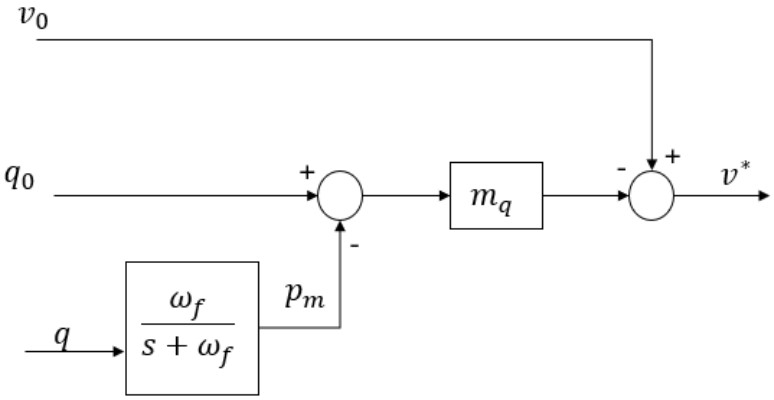

Figure 11:Reactive power droop control for microgrid [20]**.**

$$u^* = u_{grid} - m_q(q_m - q_0) \tag{8}$$

This control scheme determines the converter frequency by a droop gain m_p and the difference between the measured power and the power set-point. Likewise, the controller´s voltage is set by the droop gain m_q and the difference between the measured reactive power and the reactive power set-point. A low pass filter must filter the output active and reactive power from the converter for stable control loops and remove the disturbances and oscillations [20]. Equation 9 is the expression of the filtering of active and reactive power;

$$p_m = \frac{\omega_f}{s+\omega_f} p_{el} \;,\; q_m = \frac{\omega_f}{s+\omega_f} q_{el} \tag{9}$$

From the block diagrams of active and reactive power droop controls, the output of these controls is the phase angle and the voltage amplitude similar to the VSM control schemes, open-loop PWM and cascaded control previously discussed (Figure 8). The droop control is combined with these two control schemes. The active power flow gives the frequency and phase angle, while the reactive power flow gives the voltage amplitude in the control scheme of Figure 8. It is assumed that the control schemes are mainly inductive system impedance to decouple both the droop controllers.

2.3.1 Equivalence between the Microgrid droop control and VSM

There is a substantial similarity between the VSM implementation and the droop control for microgrids [20]. For a lower order SM, the frequency and the phase angle for VSM are provided by the swing equation in (4) and by (7) for the droop controller. When the grid frequency ω_{grid} and the active power reference p_0 are held constant, these two equations may be shown to be equal for small signal behavior around a steady-state operation.

From equation (7) and (9) we can get,

$$\omega_{n,pu}^{*} = \omega_{grid,pu} - m_p \left(\frac{\omega_f}{s + \omega_f} p_{el} - p_0 \right) \tag{10}$$

From equation (10) p_{el} can be calculated as,

$$p_{el} = \left(\frac{s}{\omega_f} + 1 \right) \left(\frac{1}{m_p} \left(\omega_{grid,pu} - \omega_{n,pu}^{*} \right) + p_0 \right) \tag{11}$$

$$p_{el} = \frac{\left(\cancel{s \cdot \omega_{grid,pu}} - s \cdot \omega_{n,pu}^{*} \right)}{\omega_f m_p} + \frac{\left(\omega_{grid,pu} - \omega_{n,pu}^{*} \right)}{m_p} + \cancel{\frac{s \cdot p_0}{\omega_f}} + p_0 \tag{12}$$

By removing the derivatives of constant terms from the above equation it can be simplified to:

$$\underbrace{\frac{1}{\omega_f m_p} s \cdot \omega}_{\text{Inertia term}} = p_0 - p_{el} - \underbrace{\frac{1}{m_p} \left(\omega_{n,pu}^{*} - \omega_{grid,pu} \right)}_{\text{Damping Term}} \tag{13}$$

The above equation (13) has the same form with the VSM equation in (4). By comparing equation (13) with equation (4) we get,

$$T_m = \frac{1}{\omega_f m_p}, \qquad d_{DQ} = \frac{1}{m_p} \tag{14}$$

The damping gain from the swing equation is inversely proportional to the active power droop gain. Furthermore, the virtual inertia is equivalent to the first-order low pass filter on active power. As a result, the droop regulator's parameters can be tuned to mimic the small-signal behavior of a specific synchronous machine. So, the low pass filter is not just for eliminating the high-frequency harmonics but also for providing inertia support.

2.3 Alternative Strategy to Virtual Synchronous Machine

As previously discussed, the droop control is a popular method used for fair power-sharing in frequency converters. In this section, the limitations of the conventional static droop characteristics and improvements will be discussed based on [26].

The control loop in the droop strategy configures the converter to limit its output voltage frequency and amplitude to compensate for active and reactive power variations. As power demand rises, synchronous generators may experience frequency drops, thus needing a droop control algorithm. With the proliferation of nonlinear loads into the distribution energy mix, existing droop algorithms struggle to strike a balance between voltage regulation and power-sharing due to low-pass filters connected to the system to handle the harmonic current. The power system's stability and dynamics are strongly impacted by the filters' behaviors and the magnitude of the droop coefficients, which are restricted by the maximum limits of the output voltage amplitude and frequency.

To improve the slow dynamic and transient response of frequency converters, a supplementary transient droop characteristics is added to the conventional droop method. According to [27] the active and reactive powers for a frequency converter can be represented as:

$$P = \frac{E.U}{X}.sin\delta \tag{15}$$

$$Q = \frac{E.Ucos\delta - U^2}{X} \tag{16}$$

Where X represents reactance at the converter output, δ is the phase angle between the converter and the point of common coupling. E and U are the amplitude of the voltage of the inverter and the load voltage, respectively.

Based on the equations (15) and (16), the active power P is entirely dependent on the power angle δ and the reactive power Q, relies on the output-voltage amplitude. The current droop approach introduces droop components in E and ω which are respective amplitude and frequency of the output voltage of the frequency converter.

$$\omega = \omega^* - mP \tag{17}$$

$$E = E^* - nQ \tag{18}$$

The ω^* and E^* are the voltage angular frequency and amplitude at no load. m and n represent droop coefficients for the frequency and amplitude, respectively.

[28] mentioned that an increased droop coefficient produces quality power to the grid or load but comes at the expense of ineffective voltage regulation. Figure 12 and Figure 13 show that the acceptable frequency and amplitude deviations limits are 2% and 5%, respectively. The inherent tradeoff of this control technique impedes the functionality of the coefficients mentioned above, which can impact transient response, power-sharing accuracy, and system stability.

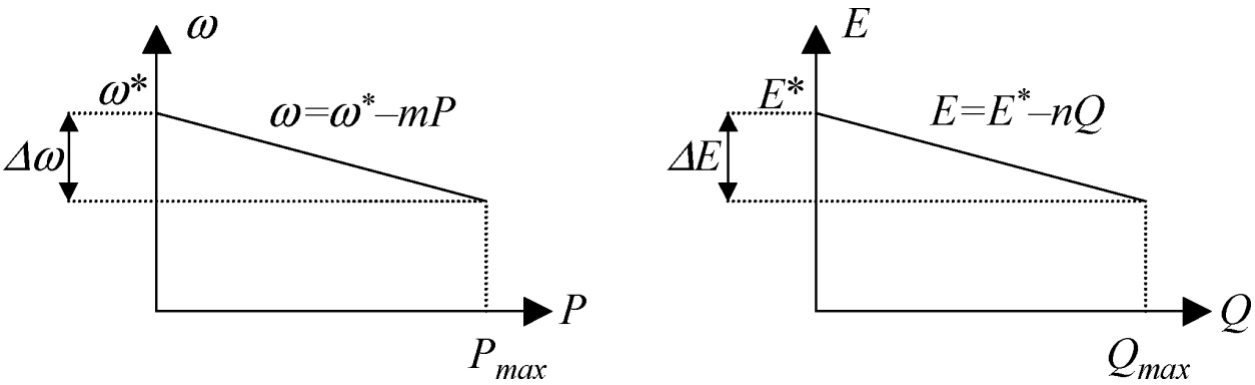

Figure 12: Conventional Droop Characteristics P- w and Q-E. [26]

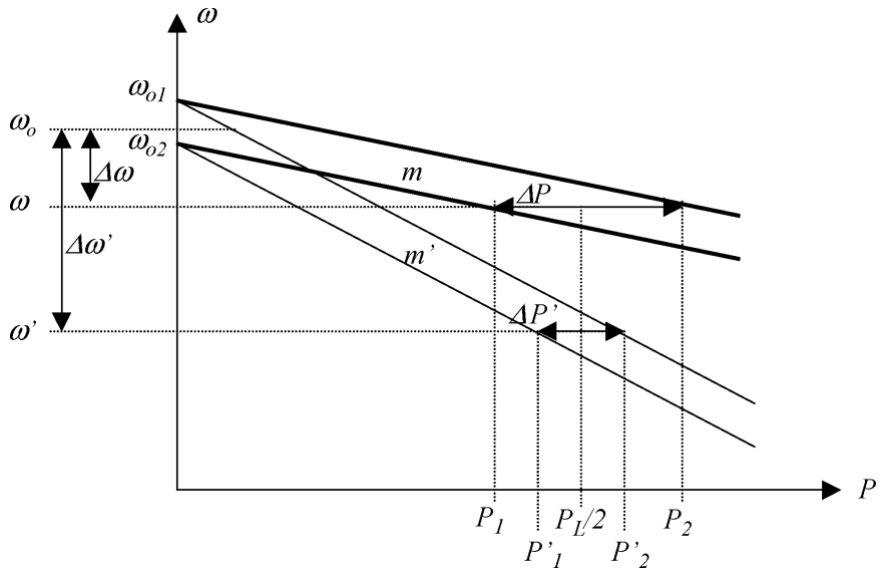

Figure 13: Tradeoff between frequency deviation and active power sharing (droop coefficient $m' > m$) [26].

From the droop equations above, the magnitude of the instantaneous active and reactive output powers over one line cycle are needed to execute the droop control. This can be achieved through the help of low-pass filters and droop with lower bandwidth than that of the closed-loop inverter. In consequence, the power calculation filters, and droop coefficients decide to a great extent, the dynamics and stability of frequency converters. Damping and

oscillations from phase shift differences could cause instabilities and a huge transient circulating that can overload and damage the system.

Nonetheless, the conventional droop strategy has many innate challenges related to its limited transient response since system dynamics heavily rely upon power calculations, filter characteristics, droop coefficients, and output impedance. These values are set on the line frequency, the maximum allocated frequency and amplitude deviations, and the nominal output power. Hence, the converter properties cannot be independently controlled by adopting the static droop method.

However, it is possible to address the challenges of the conventional droop strategy by improving the system's dynamics through a better droop-control scheme. These droop characteristics can be expressed as:

$$\emptyset = -m \int_{-\infty}^{t} P d\tau - m_p P - m_d \frac{dP}{dt} \tag{19}$$

$$E = E^* - nQ - n_d \frac{dQ}{dt} \tag{20}$$

Where n_d is the derivative coefficient of the reactive power Q; m, m_p and m_d are the integral, proportional, and derivative coefficients of the active power P. If we consider that $\omega = d\emptyset/dt$, the steady-state voltage and the frequency droops matches exactly those obtained with the conventional method, expressed by the equations (17) and (18).

The suggested control strategy offers flexibility towards the modification of transient response, control coefficients and, simultaneously, includes the static droop characteristics. Meanwhile, it reduces the transient circulating current in the components, and enhances the dynamic performance of the entire power system. Moreover, the coefficients m and n maintain the steady-state droop function while m_p, m_d, and n_d are for stability and appreciable transient response.

Figure 14 gives a diagrammatic representation of an alternative control scheme for virtual synchronous machine. The average active power P is generated by the product of inverter output voltage v_o and inverter output current i_o , and the result is sent to a low-pass filter. Similarly, the mean reactive power is calculated, but the output voltage must be delayed by $90°$.

To modify the phase voltage at the output, equation (19) is executed, which correlates with a PID controller applied over the average active power signal. The regulation of the output-voltage amplitude is made with the help of the static droop method with an addition of the reactive power derivative term as expressed in equation (20). Furthermore, the emulation of the output impedance of the inverter can be done using a high-pass filter to share linear and non-linear loads. An extra faster loop is included for the output impedance algorithm to achieve such a requirement. On the flip side, inductive output impedance can be achieved by

reducing the output voltage in proportion to the time-derivative of the fundamental output-current.

In contrast, the resistive-impedance should be achieved to distribute the harmonic current component without increasing output-voltage total harmonic distortion (THD). Hence, a high pass filter can easily handle both characteristics. More importantly, this filter's gain and pole value must be selected appropriately. To a large extent, an effective design of this output impedance can reduce the impact the line impedance has on the power-sharing accuracy.

In this thesis, the accuracy of this alternative virtual synchronous machine control strategy will be investigated.

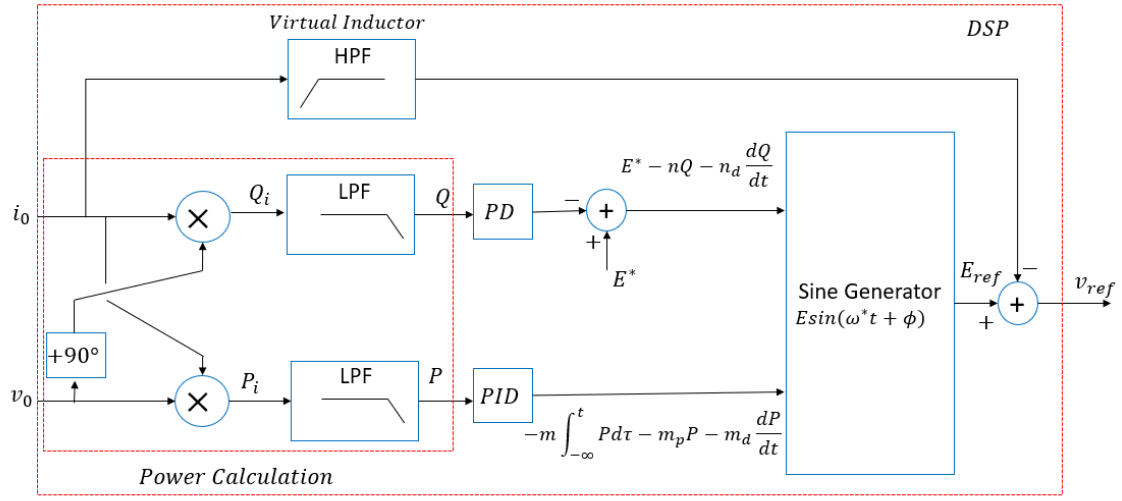

Figure 14: Block Diagram of Alternative Strategy for Virtual Synchronous Machine [26].

2.4 PID Controllers for Virtual Synchronous Machine Control

To effectively manage the VSM control of the two-level three-phase VSCs to handle hydropower and renewable energy integration disturbances, the concept of PID control must be considered for optimum operation. Discussions on virtual inertia control have been done in previous chapters.

When applying virtual inertia to the inner current control loop, a wrongful selection of its PID values can result in high-frequency deviation (over/under frequency), slow recovery time and instability. To prevent such inconsistencies in the control loops, PI controllers with adequate tuning techniques will have to be applied to the control algorithm to ensure system frequency stability and adjustments to variations in loads and generations.

In process control, the operation of PIDs is done in feedback control. A feedback control concept is used to achieve a desired response and performance for a control system. The initiative is accomplished with an open-loop system, where the controller defines the input signal to the process on the fundamental of the reference signal. In the case of closed loop

systems, the controller sets the input signal to the process using the measurement of the output, referred to as the feedback signal. Figure 15 shows a feedback control where P(s) is the process, C(s) is the controller, y_s is the reference signal (desired process output), F(s) is the feedforward filter, y is the process output, u is the controlled output, n is the measurement noise signal, and d is the disturbance signal [16].

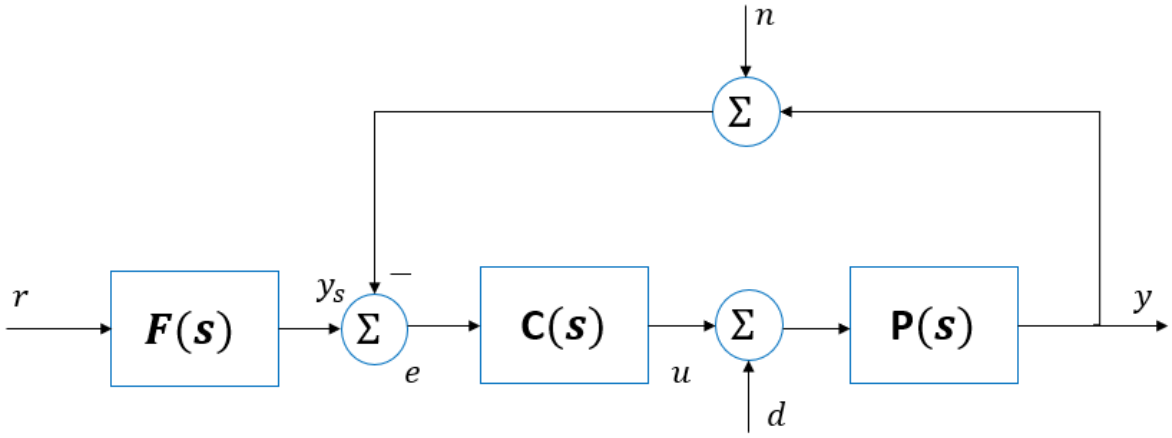

Figure 15: Dynamic Structure of a feedback control loop [16].

The PI or PID control is a form of feedback control mechanism. The Proportional (P), Integral (I), and Derivative (D) actions is summarized as follows:

2.4.1 Proportional Action

The proportional control connects to the present magnitude of its control error. According to Figure 15 the proportional action (u_p) is equivalent to the current control error expressed as:

$$u_p(t) = K_p e(t) = K_p(y_s(t) - y(t)) \quad (21)$$

Where K_p is the proportional control gain.

The transfer function of the proportional (P) controller in the Laplace domain is:

$$C(s) = K_p \quad (22)$$

The primary benefit of a proportional controller is being able to offer a minimal control variable whenever there is a little control error, thus preventing unnecessary control attempts. The main demerit of introducing a singular proportional controller is the generation of a steady-state error, which adjusts the action of the P control as:

$$u_p(t) = K_p e(t) + u_b \quad (23)$$

It can be stated that the magnitude of u_b is ascertained as constant or adjusted manually until the steady-state error is zero.

2.4.2 Integral Action

The integral control connects to the previous value of the system's control error.

$$u_i(t) = K_i \int_0^t e(t)\, dt \; = \int_0^t \big(y_s(t) \; - y(t)\big) \; dt \tag{24}$$

Where K_i is the integral control gain.

The integral action handles the past values of the control error. The transfer function of the integral controller in the Laplace domain is:

$$C(s) = \frac{K_i}{s} \tag{25}$$

Where,

$$K_i = \frac{K_p}{T_i} \tag{26}$$

By setting the pole at the origin of the complex plane, the steady-state error drops to 0 with the addition of a reference signal or the presence of a disturbance. The necessary integral action is done by an automatic setting of u_b in equation (23), hence putting the steady-state error to zero. The general PI transfer function in Laplace domain is:

$$C(s) = K_p \; + \frac{K_i}{s} \; = K_p \; (\frac{1}{s.T_i} \; + \; 1) \tag{27}$$

Where T_i is controller integral time. By varying the T_i, it impacts the proportional and integral control actions. When we vary the K_p, both control actions are also affected. The combination of both proportional and Integral (PI) action can correct the oscillatory response and the steady-state error compared to using only a proportional controller.

2.4.3 Derivative Action

The derivative control takes care of the predicted future value of its control error. The derivative action can be expressed as:

$$u_d(t) = K_d \frac{de(t)}{dt} = K_d \frac{d(y_s(t) - y(t))}{dt} \tag{28}$$

Where K_d is the derivative control gain and represented as:

$$K_d = \; K_p T_d \tag{29}$$

The transfer function of the derivative controller in the Laplace domain is:

$$C(s) = sK_d = s.K_pT_d \tag{30}$$

Where T_d is the controller derivative time. Also, the Proportional-derivative control in the time domain can be defined as:

$$C(s) = K_p(T_d\frac{de(t)}{dt} + e(t)) \tag{31}$$

The variation of T_d changes the behavior of the proportional and derivative control actions. Similarly, varying K_p has an impact on the dual control actions. Consequently, the derivative action predicts false trends of the control error and gives a corresponding reaction.

There are situations where a process control may require the PID control actions. The mathematical expression in the Laplace domain is:

$$C(s) = K_p + \frac{K_i}{s} + s.K_d \tag{32}$$

$$C(s) = K_p(1 + \frac{1}{s.T_i} + s.T_d) \tag{33}$$

The PID equation Laplace domain can be rewritten in time domain based on the control system in Figure 15.

$$u(t) = u_p(t) + u_i(t) + u_d(t) \tag{34}$$

In conclusion, the Proportional, Integral and Derivative Control actions can be represented in terms of the control output $u(t)$ of the PID controller as:

$$u(t) = (K_p\big(y_s(t) - y(t)\big) + \left(\frac{K_p}{T_i}\int_0^t (y_s - y(t)dt)\right) + (K_pT_d\frac{y_s(t) - y(t))}{dt}) \tag{35}$$

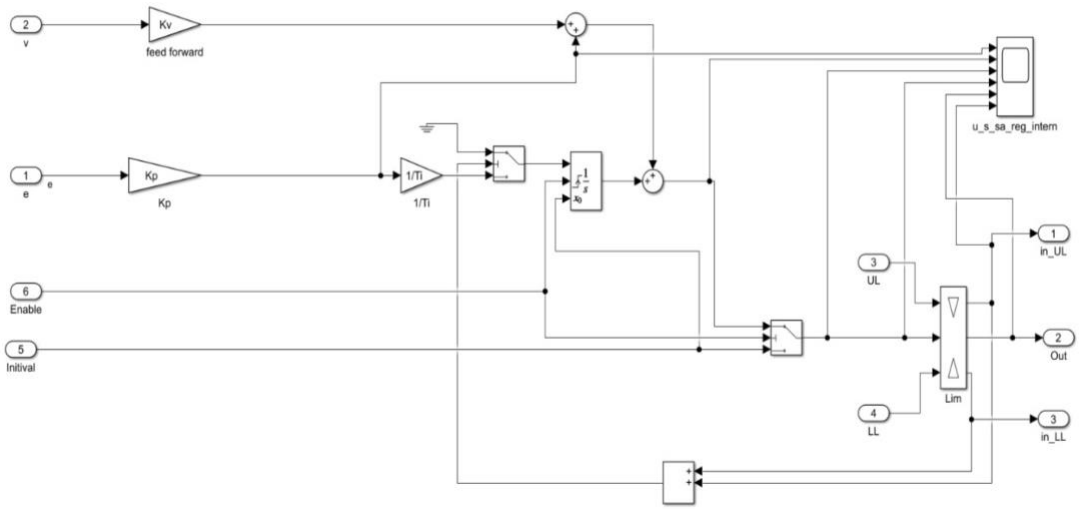

Figure 16: Line Diagram of a PI Controller in Simulink.

2.5 Tuning of PID Controllers

According to [16], [29] there are various classical and modern methodologies for tuning analogue/digital PI controllers to suitable control gains. Some of the common methods include:

2.5.1 Trial and Error Approach

This method is used in the absence of a systemic approach to track during the design control process. An adequate experience is required to set suitable control gains of K_p , and K_i to achieve compatibility with respect to speed and closed-loop stability. Every adjustment to each control gain affects the systems performance as shown in Table 1.

Table 1: System Performance after Increasing Control Gains

Parameter	Stability	Steady-state error	Speed
K_p	Decreased	Decreased	Increased
K_i	Increased	Eradicated	Decreased
K_d	Increased	Increased	Increased

2.5.2 Use of Bode Plot

Utilizing Bode-plots where a classic criterion is that the open loop transfer function will have a gain margin of at least 6 dB and a phase margin of $45°$. The open loop transfer function can be adopted for stability analysis of any system.

2.5.3 Pole location

This design technique is dependent on the transfer function of the systems. It involves the evaluation of the closed-loop pole positions on the complex plane by shifting the gains of a controller. It applies to first- or second-order systems.
For first-order plant, the system is represented as:

$$P(s) = \frac{K_s}{s.T_{sum} + 1} \tag{36}$$

Where T_{sum} is the time constant, and K_s is the gain of the system.

The PI control actions can be expresses as:

$$C(s) = K_p(\frac{K_s}{s.T_i} + 1) \tag{37}$$

The closed-loop transfer function of the system is:

$$G(s) = \frac{P(s)C(s)}{1 + P(s)C(s)} \tag{38}$$

For a second-order system:

$$Q(s) = s^2 + s\left(\frac{1 + K_s.K_p}{T_{sum}}\right) + \frac{K_s.K_p}{T_{sum}.T_i} \tag{39}$$

The second-order equation is represented in relation to its natural frequency (ω_n) and relative damping (ξ) as:

$$Q(s) = s^2 + 2\omega_n\xi s + \omega_n^2 \tag{40}$$

The respective K_p and T_i for a PI controlled can be computed as:

$$K_p = \frac{2\omega_n\xi.T_{sum} - 1}{K_s} \tag{41}$$

$$T_i = \frac{2\omega_n\xi.T_{sum} - 1}{\omega_n^2.T_{sum}} \tag{42}$$

2.5.4 Use of Modulus optimum and Symmetric optimum

For tuning the PI controllers for the AFE, the symmetric optimum will be adopted for calculating the control parameters based on the process parameters required for generating the I_d^* and I_q^* reference currents for the hysteresis controller.

The operation of the symmetrical optimum for a system is that there is an integration of the process transfer-function P(s). This adjustment makes it impossible to eliminate the time constant T_{sum} by the help of T_i in the PI controller. This creates a transfer function with two integrators, implying a system at the limit of instability.

The closed loop transfer function for a symmetric optimum control can be obtained as:

$$G(s) = \frac{1 + T_i.s}{1 + T_i.s + \frac{T_1 T_i.}{K_p K_s}.s^2 + \frac{T_1 T_i T_{eq}}{K_p K_s}.s^3} \tag{43}$$

$$G(s) = \frac{1 + \beta.T_{sum}.s}{1 + \beta.T_{sum}.s + \beta.\sqrt{\beta}.T_{sum}^2.s^2 + \beta.\sqrt{\beta}.T_{sum}^3.s^3} \tag{44}$$

From equations (43) and (44) one obtains the proportional and integral control gains as:

$$K_p = \frac{T_1}{K_s\sqrt{\beta}.T_{sum}} \tag{45}$$

$$T_i = \beta.T_{sum} \tag{46}$$

Based on the symmetric optimum approach, its open loop transfer function will have a phase margin of 0 when the amplitude of the open loop is 1.

Chapter 3

3.0 Modelling of active front end converter with lcl filter

3.1 Reference Frame for Control Operations

For several decades, there has been widespread acceptance of three-phase electrical systems for power generation, transmission, and distribution.

In modern engineering applications, electrical machines can convert electrical energy to mechanical energy and vice-versa. The main components of these machines are stators and rotors. These machines have three-phase winding in their stators because of the ease of obtaining three-phase sinusoidal signals $120°$ apart [30]. The machine configuration generates a rotating electromagnetic field with constant amplitude at the required frequency. Also, torque components can be generated from electrical machines, which are dependent on the strength of the rotor magnetic field, the strength of the external magnetic field, the sine of the angle in between them, and the machine geometry. In advanced power applications, electrical machines can be designed up to 6 and 9 phases, but the practicality of these machine types is usually complex compared to conventional three-phase electrical systems. Hence, the reason for the popularity of three-phase machines in present times.

However, there is a significant demerit to the three-phase machine despite its acceptability in the power industry. The numerical analysis of three-phase systems often becomes cumbersome due to their oscillating properties [30]. As the proliferation of converter-based renewable energy systems continues to increase, this significantly reduce the use of synchronous machines used for power generation [7], [20]. One may argue that such replacements might reduce the mathematical calculations of electrical machines; nevertheless, this extent of converter domination will indeed require the application of the reference frame theory (RFT) for its three-phase converter control. Previously, the reference frame concepts were developed for analyzing unbalanced three-phase faults. Still, they now have applications in electrical machine analysis and modelling [31], AFEs [32], multi-inverter modelling [25], microgrid simulation [33], Phase-Locked Loops (PLLs) [34], and active power filters [35]. To accurately model the control mechanism for the AFE converter, the geometry of the reference frame theorems-Clarke and Park transformations must be discussed. Figure 17 gives an overview of the transformations.

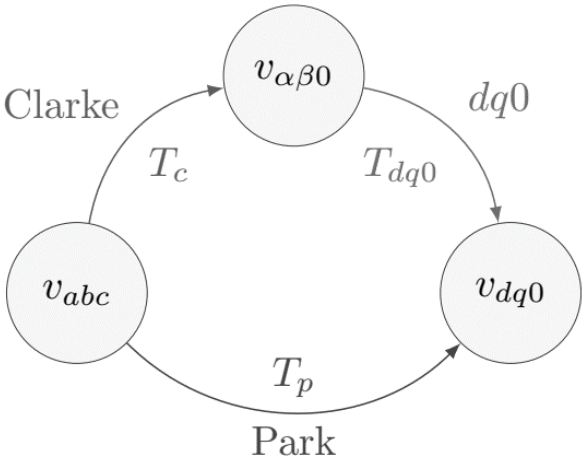

Figure 17: Reference Frame Theorem Overview [36]***.***

In power systems analysis, current and voltage are represented with space vectors in the stationary reference frame as shown in Figure 18. Assuming i_R, i_Y, and i_B are instantaneous balanced three-phase currents. Then,

$$i_R + i_Y + i_B = 0 \tag{47}$$

As regards the phase currents mentioned above, the space vectors can be represented as follows:

$$i = K\,(i_R + a i_Y + a^2 i_B) \tag{48}$$

Where $'a'$ and $'K = ⅔'$ are the operator and transformation constant respectively.

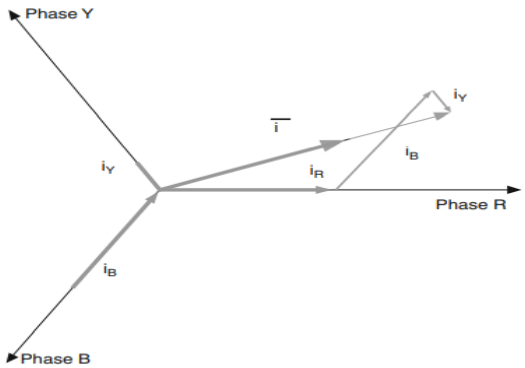

Figure 18: Current Space Vector Representation [37]***.***

The current space vector can also be expressed in a two-axis stationary reference frame in which the fundamental component of the current space vector is equivalent to the instantaneous magnitude of the direct-axis component i_α, and the imaginary segment is equal to the quadrature-axis section, i_β. The representation of three-phase currents vectors to two-phase fictitious currents components is termed Clarke transformation.

$$i = i_\alpha + i_\beta \tag{49}$$

Mathematically, the stator currents in a stationary reference frame can be expressed as:

$$\begin{bmatrix} i_\alpha \\ i_\beta \end{bmatrix} = \frac{2}{3} \times \begin{bmatrix} 1 & -\frac{1}{2} & -\frac{1}{2} \\ 0 & \frac{\sqrt{3}}{2} & -\frac{\sqrt{3}}{2} \end{bmatrix} \times \begin{bmatrix} i_R \\ i_Y \\ i_B \end{bmatrix} \tag{50}$$

Furthermore, current space vectors can be represented at rotating speeds w besides the stationary reference frame of the stator. Assuming a general reference plane is used, it becomes possible to transform current space vectors from alpha-beta to a direct-quadrature axes rotating at an instantaneous speed, $w = \frac{d\theta}{dt}$. θ represents the angular relationship of the d-axis of the stationary reference frame (alpha) and the real component of the general reference plane. The current space vector equation can be expressed as:

$$I = i \cdot e^{-j\theta} \tag{51}$$

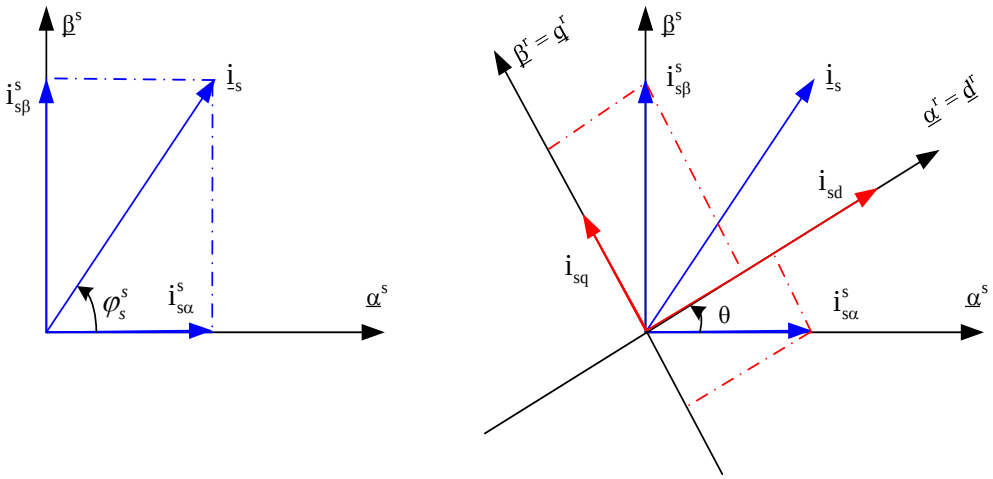

Figure 19:d-q Rotating Reference Frame [29]***.***

Then, it is possible to transform the alpha-beta stationary reference frame into a d-q rotating reference frame. The matrix components of the Clarke and Park transformations for current, voltage and flux space vectors are summarized in Table 2 and power calculations of these transformations are represented in Table 3 below:

Table 2: Transformations [38], [39]

	Standard Amplitude-Invariant	Power-Invariant
Clarke $abc\ to\ \alpha\beta 0$	$\frac{2}{3}\begin{bmatrix} 1 & -\frac{1}{2} & -\frac{1}{2} \\ 0 & \frac{\sqrt{3}}{2} & -\frac{\sqrt{3}}{2} \\ \frac{1}{2} & \frac{1}{2} & \frac{1}{2} \end{bmatrix}$	$\sqrt{\frac{2}{3}}\begin{bmatrix} 1 & -\frac{1}{2} & -\frac{1}{2} \\ 0 & \frac{\sqrt{3}}{2} & -\frac{\sqrt{3}}{2} \\ \frac{1}{\sqrt{2}} & \frac{1}{\sqrt{2}} & \frac{1}{\sqrt{2}} \end{bmatrix}$
Park $abc\ to\ dq0$	$\frac{2}{3}\begin{bmatrix} \cos(\theta) & \cos\left(\theta-\frac{2\pi}{3}\right) & \cos\left(\theta+\frac{2\pi}{3}\right) \\ -\sin(\theta) & -\sin\left(\theta-\frac{2\pi}{3}\right) & -\sin\left(\theta+\frac{2\pi}{3}\right) \\ \frac{1}{2} & \frac{1}{2} & \frac{1}{2} \end{bmatrix}$	$\sqrt{\frac{2}{3}}\begin{bmatrix} \cos(\theta) & \cos\left(\theta-\frac{2\pi}{3}\right) & \cos\left(\theta+\frac{2\pi}{3}\right) \\ -\sin(\theta) & -\sin\left(\theta-\frac{2\pi}{3}\right) & -\sin\left(\theta+\frac{2\pi}{3}\right) \\ \frac{1}{\sqrt{2}} & \frac{1}{\sqrt{2}} & \frac{1}{\sqrt{2}} \end{bmatrix}$
Inverse Clark $\alpha\beta 0\ to\ abc$	$\begin{bmatrix} 1 & 0 & 1 \\ -\frac{1}{2} & \frac{\sqrt{3}}{2} & 1 \\ -\frac{1}{2} & -\frac{\sqrt{3}}{2} & 1 \end{bmatrix}$	$\sqrt{\frac{2}{3}}\begin{bmatrix} 1 & 0 & \frac{1}{\sqrt{2}} \\ -\frac{1}{2} & \frac{\sqrt{3}}{2} & \frac{1}{\sqrt{2}} \\ -\frac{1}{2} & -\frac{\sqrt{3}}{2} & \frac{1}{\sqrt{2}} \end{bmatrix}$
Inverse Park $dq0\ to\ abc$	$\begin{bmatrix} \cos(\theta) & -\sin(\theta) & 1 \\ \cos\left(\theta-\frac{2\pi}{3}\right) & -\sin\left(\theta-\frac{2\pi}{3}\right) & 1 \\ \cos\left(\theta+\frac{2\pi}{3}\right) & -\sin\left(\theta+\frac{2\pi}{3}\right) & 1 \end{bmatrix}$	$\sqrt{\frac{2}{3}}\begin{bmatrix} \cos(\theta) & -\sin(\theta) & \frac{1}{\sqrt{2}} \\ \cos\left(\theta-\frac{2\pi}{3}\right) & -\sin\left(\theta-\frac{2\pi}{3}\right) & \frac{1}{\sqrt{2}} \\ \cos\left(\theta+\frac{2\pi}{3}\right) & -\sin\left(\theta+\frac{2\pi}{3}\right) & \frac{1}{\sqrt{2}} \end{bmatrix}$

Table 3:Power Transformations [40]

	Standard (Amplitude-Invariant)	Power-Invariant
$\alpha\beta 0$	$p(t) = \frac{3}{2}(v_\alpha i_\alpha + v_\beta i_\beta + 2v_0 i_0)$	$p(t) = v_\alpha i_\alpha + v_\beta i_\beta + v_0 i_0$
	$q(t) = \frac{3}{2}(v_\beta i_\alpha + v_\alpha i_\beta)$	$q(t) = (v_\beta i_\alpha - v_\alpha i_\beta)$
$dq0$	$p(t) = \frac{3}{2}(v_d i_d + v_q i_q + 2v_0 i_0)$	$p(t) = (v_d i_d + v_d i_d + v_0 i_0)$
	$q(t) = \frac{3}{2}(v_q i_d - v_d i_q)$	$q(t) = (v_q i_d - v_d i_q)$

3.2 Operation of Voltage Source Converters

In high power applications, the Voltage Source Converter (VSC) has been adjudged to be a reliable power electronic device capable of transitioning circuits from a DC voltage or current source to an AC voltage or current and vice-versa. In this manner, the inverter produces an output ac voltage with variations in amplitude and frequency different from the input [41].

In this research, the two-level Voltage Source Inverter (VSI) or AFE has been chosen to convert a DC voltage into a three-phase AC voltage at the output. Whenever power or voltage is required by the load or external grid, the DC bus of the VSI releases the stored energy through the alternate switching operations of the 6 power electronics components present in the converter. The IGBTs and diodes of the VSI are activated complementarily to ensure that the switches on the same bridge-leg are not switching simultaneously, as this will lead to a short circuit across the DC link and expose the converter switching devices to the likelihood of deterioration due to over-current [42].

As shown in Figure 20, the smooth operation of the VSI ensures that whenever the upper switch S1 turns ON, the lower switch S2 is OFF and vice versa. In practical application, a dead time is often introduced to the gate signals of the upper and lower switches to prevent simultaneous operation of both switches. The two-level, three-phase VSI absorbs the voltage in the DC link to produce three-phase voltage waveforms with $120°$ displacement in the time domain. While the voltage of the DC bus is being depleted, it must be replaced by an external source to maintain a constant voltage at every given time. BESS can supply the DC link voltage, or a result of a voltage source rectifier, or the DC circuit of an adjustable speed drive (ASD). The configuration of a VSI allows current and power to be sent bi-directionally through the connection of IGBTs and anti-parallel diodes.

Furthermore, a converter can be made to operate for half or one-third of its conduction cycle. At a constant DC link voltage, the VSI produces a higher-order component of the output voltage at $180°$ conduction Figure 21 unlike the output of the $120°$ conduction method. The converter output peak phase voltages can be expressed as

$$V_{m1} = (\frac{2}{\pi}) \times V_{dc}, \tag{52}$$

And,

$$V_{m1} = (\frac{3}{2\pi}) \times V_{dc} \tag{53}$$

where V_{dc} is the converter's dc voltage and V_{m1} is the fundamental peak phase voltage.

Moreover, the modulation index, m, which is the gain or amplitude of the converter output can be expressed mathematically as:

$$m = \left(\frac{V_{m1}}{\frac{1}{2} \times V_{dc}} \right) \tag{54}$$

The $120°$ and $180°$ conduction method have gain values of $\frac{4}{\pi}$ and $\frac{3}{2\pi}$ respectively. Due to further research efforts, these conduction methodologies have been faced out because they cannot produce the magnitude of fundamental voltage required, and they generate low-order harmonics which have high-cost implications if filtered [42].

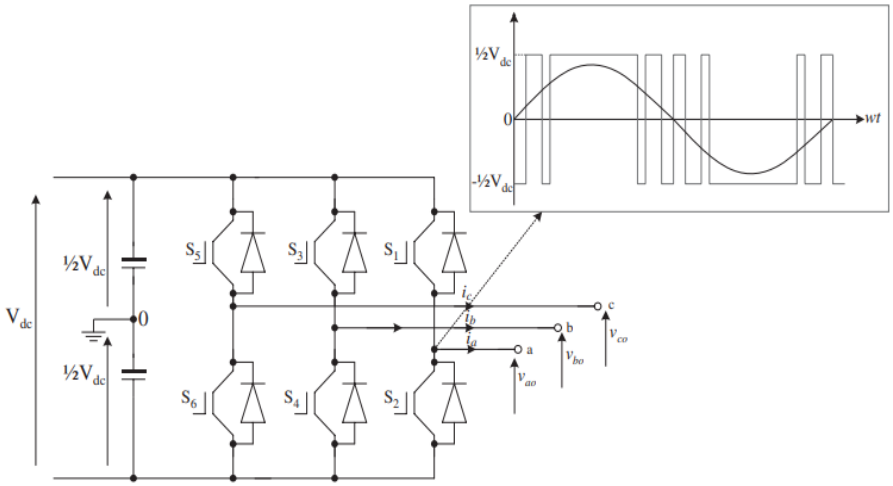

Figure 20: Grid or Network Side Converter (VSC) [42]***.***

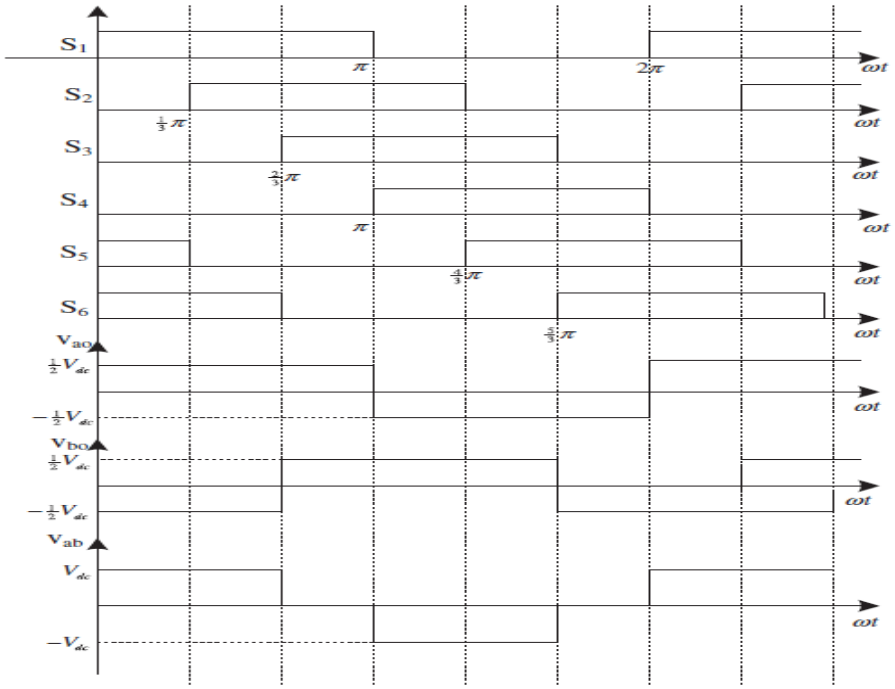

Figure 21:Gate signal mapping and converter output voltage for 180 degrees conduction method [42]***.***

3.3 Sinusoidal Pulse Width Modulation

When generating the desired output voltage, the switching technique is carefully chosen to control the VSI to ensure low power dissipation on power switches, low harmonic contents, and reduced electromagnetic interference (EMI) outputs [43]. An advanced switching strategy for VSCs is the Pulse Width Modulation method, in which a sinusoidal control signal serving as a signal reference is used in generating a sinusoidal output waveform. This method has widespread acceptance because it reduces the harmonics that accompany voltage or current signals. Selective Harmonic Elimination and Space Vector Modulation are the most common switching strategies. The Space Vector Pulse Width modulation methodology shall be highlighted for this research.

Before the Space Vector PWM can be treated, the Sinusoidal SPWM must be explained. The application of the Sinusoidal Pulse Width Modulation technique involves a comparison of a low-frequency reference signal with a high-frequency carrier signal. Its fundamental frequency must match its reference frequency to achieve the desired output voltage. The mathematical relationship between both signals can be represented as:

$$m_f = \frac{f_{cr}}{f_s} \tag{55}$$

Where m_f is the modulation frequency index, f_{cr} is the carrier frequency, and f_s is the reference frequency.

Similarly, the desired amplitude of the voltage waveform is controlled by the ratio of the peak reference voltage amplitude to the peak carrier voltage amplitude;

$$m_a = \frac{V_{ref\_peak}}{V_{cr\_peak}} \tag{56}$$

Where m_a is the amplitude modulation index.

For a three-phase two-level VSI converter, the three-phase voltage output waveform is achieved by the operations of the switches S1-S6 as indicated in Figure 20 and Figure 21. The activation of the switches is done by matching the modulating waves with the triangular carrier wave Figure 22. Considering phase, A, when V_{ma} is greater than V_{cr} the switch, S1 is turned ON. S2 operates complementary to the operation of S1 with the comparison of V_{ma} and V_{cr}.

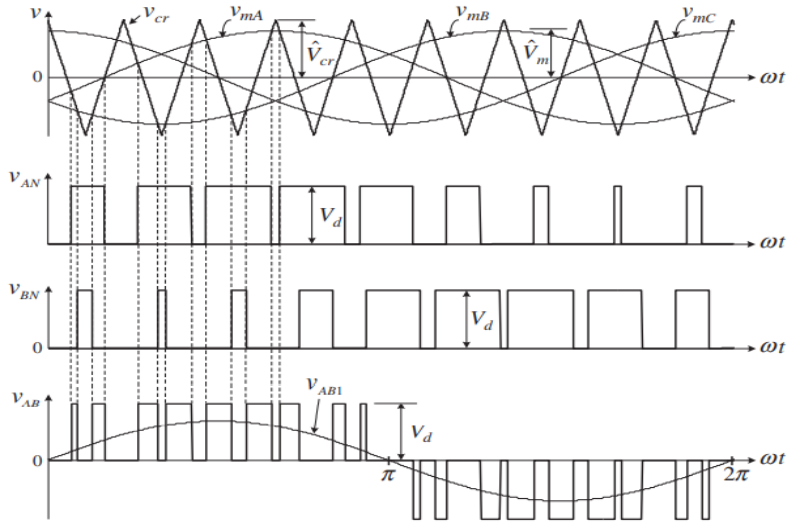

Figure 22: Sinusoidal Pulse Width Modulation [44].

During PWM switching operations, efforts are made to improve the converter output voltage at a fundamental frequency given any typical reference voltage signal.

$$V_{aref} = m \times \sin(wt + \delta) \tag{57}$$

A common strategy to achieve improved voltage waveform is usually to increase the modulation beyond the maximum attainable value (m_a >1) which certainly increases the peak of the reference signal beyond the peak of the high-frequency triangular carrier, causing over-modulation. An over-modulation technique is not advisable because it affects the linear relationship between the converter output voltage and the reference signal. It also creates difficulties in suppressing harmonics close to the carrier frequencies.

However, the modulation index constraints (range up to 1) of SPWM can be corrected by injecting 3rd harmonic sequence to the reference signals in a three-phase three-wire network. Such addition to the modulation range causes an improvement of 15.4%, implying that ample fundamental voltage waveform can be generated. Hence, the reference signals for a typical SPWM operation with 3rd harmonic (zero sequence) can be expressed as:

$$V_a^* = m_a \times \sin wt + (\frac{1}{6}) m_a \sin wt \tag{58}$$

$$V_b^* = m_a \times \sin(wt + \frac{4}{3\pi}) + (\frac{1}{6}) m_a \sin wt \tag{59}$$

$$V_c^* = m_a \times \sin(wt + \frac{2}{3\pi}) + (\frac{1}{6}) m_a \sin wt \tag{60}$$

Likewise, the modulating signals can be represented as [45]:

$$V_{mA} = \sin(wt) + \frac{1}{6}\sin(3wt) \tag{61}$$

$$V_{mB} = \sin\left(wt - \frac{2\pi}{3}\right) + \frac{1}{6}\sin(3wt) \tag{62}$$

$$V_{mB} = \sin\left(wt - \frac{4\pi}{3}\right) + \frac{1}{6}\sin(3wt) \tag{63}$$

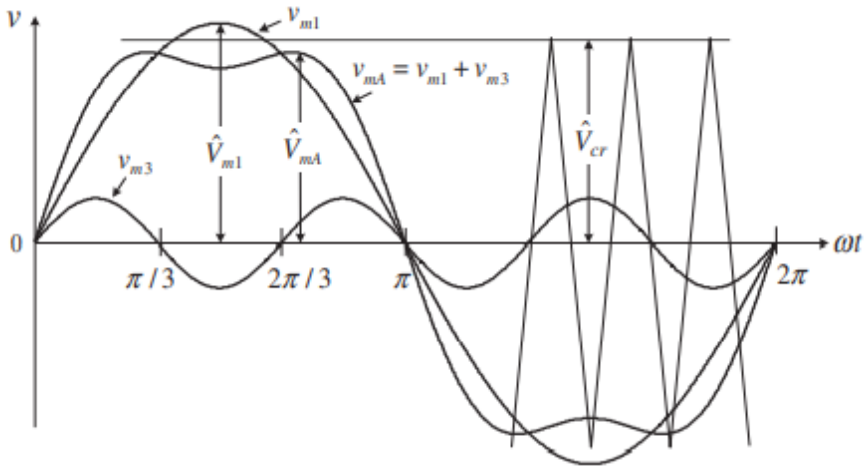

Figure 23: Modulating Signal V_{mA} with 3rd Harmonic Injection [44]**.**

Besides the two-level three-phase VSCs, there are other converter technologies dependent on the degree of voltage, current and power operations. The neutral-point clamped inverter is a popular technology for medium-voltage applications [42]. The modular multi-level inverters are recent technological improvements to VSCs. The pulse width modulation technique of VSCs incurs huge losses up to 2-3% leading to increased harmonic distortion, high transient stresses that can generate high frequency noise. Nevertheless, the MMC technology has a robust design that generates higher voltage magnitudes with reduced losses reaching 0.9-1% and little harmonic filtering requirements [46].

3.4 Hysteresis Controller

Hysteresis controller is a type of bang-bang control. Among all the methods available for generating switching pulse, hysteresis current control is the most noticed one because of its fast dynamic response, more straightforward implementation, and robustness to output load parameter variation [47]. It compares the actual measured signal with two references (upper and lower band) signals. If the measured signal is maximum or minimum than the upper and lower hysteresis band, it provides the switching signal for the inverter. The difference between the upper and lower band is known as the hysteresis band. If the measured signal exceeds the hysteresis band, the hysteresis controller makes an appropriate switching decision to

control the error within a preset band and send it for switching [48]. The hysteresis band can be fixed or adaptive.

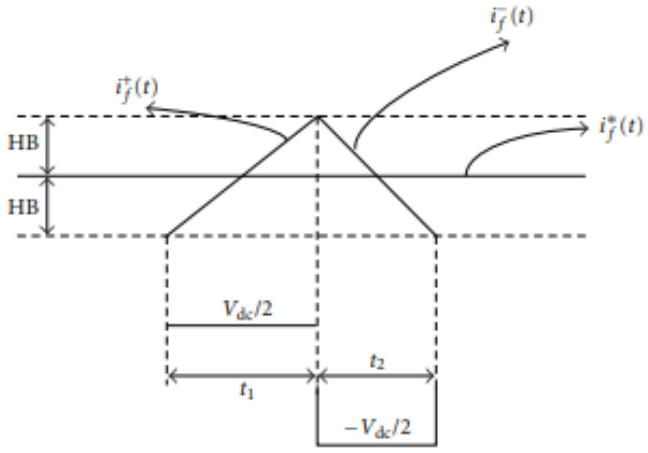

Figure 24: The upper and Lower bands of the reference compensation current [48]***.***

For fixed hysteresis bands the measured signal is compared with a fixed upper band and lower band, which generates switching signals. For fixed band hysteresis controllers, the switching signals generated are not uniform. Hence the switching frequency is not constant. This leads to high frequency components like audio noises in the source current waveform and variable switching frequency also increases the switching losses.

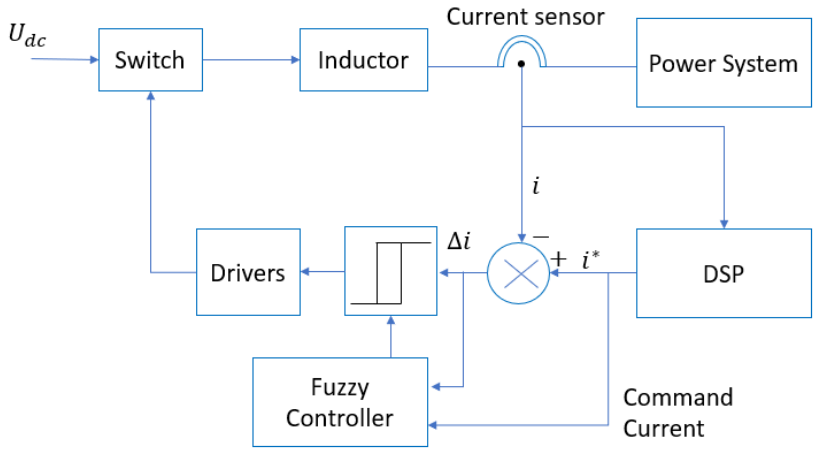

Figure 25:Block diagram of variable band hysteresis current control [49]***.***

An adaptive hysteresis control method can avoid the variable switching frequency. For this method, variable hysteresis bands can be defined for each phase so that the switching frequency remains almost the same [48]. Adaptive hysteresis control provides several advantages like better utilization of DC-bus voltage, low total harmonic distortion at the point of common coupling and simple filter design [47]. Hysteresis control is widely used for its design simplicity but to get constant frequency it can lose its simplicity. Adaptive hysteresis is extensively used in the systems where resonance occurs due to variable frequency.

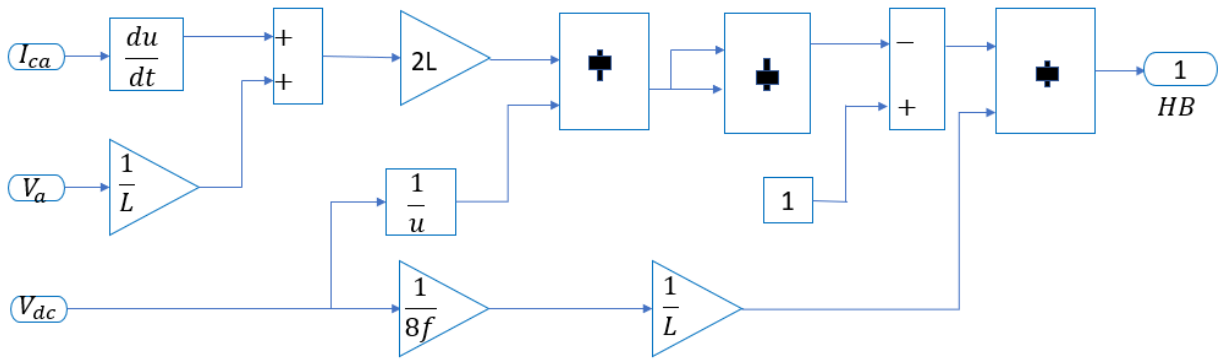

Figure 26:Block diagram of adaptive band hysteresis current control [50]***.***

The gate pulse should be generated as soon as the current reaches the upper and lower limit, but it is not possible in case of digital implementation. Also, the hysteresis current control is mostly used in a natural a-b-c frame for simplicity. Still, it is used in the stationary reference and synchronous reference frames. The switching frequency of the inverter should be as low as possible to reduce the switching losses. So, in the case of a hysteresis controller, the LCL filter design should be such a way that the average switching frequency is about 3 kHz. For this, a fixed hysteresis band of 0.1 p.u. is typically chosen.

3.5 LCL Filters

The grid side filter gives the inductive behavior necessary to work correctly when the VSC is connected to the grid. This enables the inverter to filter the harmonics generated by the voltage and current controllers in the inverter. There are stringent and specific limitations on how much harmonics can be fed into the grid at the point of common coupling. IEEE has several international standards like IEEE 519, IEEE 929, and IEEE 1547 [51] on the harmonics level that can be fed into the grid at the PCC. High switching frequency generates high switching losses by the power electronics devices. This generates low order harmonics with high currents and to eliminate this, it requires large inductors which will introduce more cost and space. To avoid such constraints, the standard way is to design a low pass filter to remove high order harmonics. A Filter with only an Inductor may work, but a combination of a capacitor may increase the performance. However, there is a high possibility of low impedance in high frequencies for the converter capacitor. That may cause problems if there are harmonics created somewhere else in the grid. An LCL filter combination will be a good consideration to avoid all this. LCL filters is a combination of a grid side Inductor, a shunt capacitor, and a converter side Inductor.

The LCL filter, according to [52], includes adequate inductor and capacitor sizes. Figure 2.9 gives a visual representation of an LCL filter's Bode Plot:

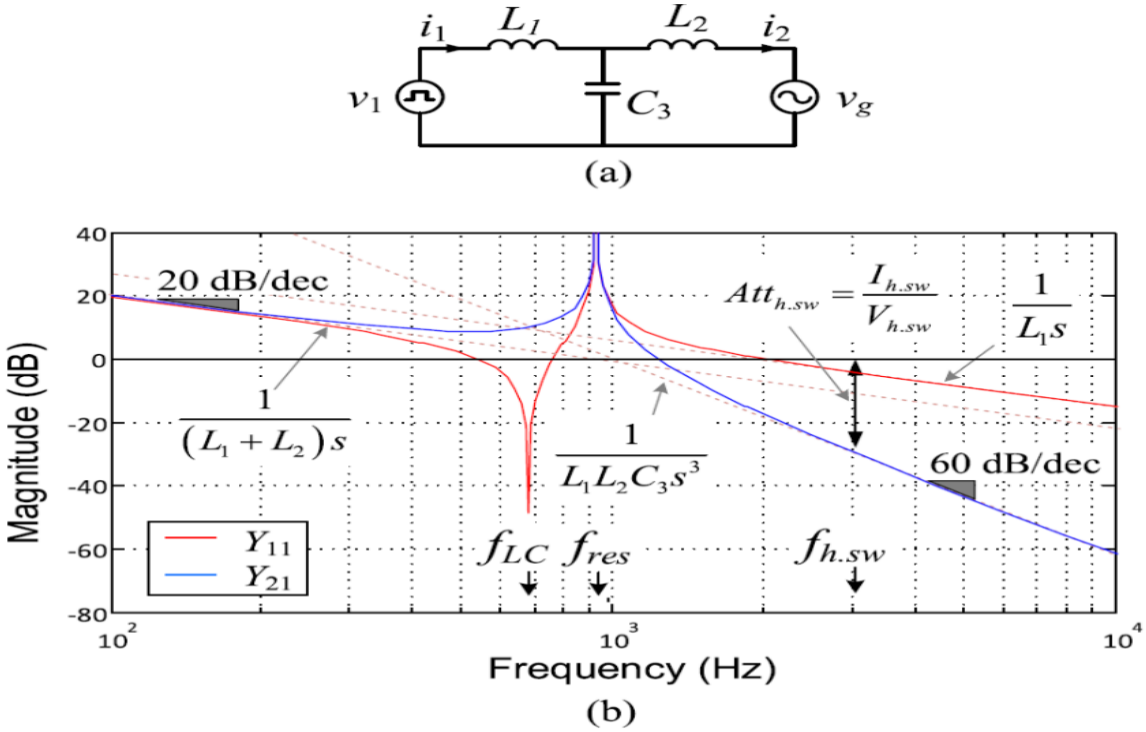

Figure 27: LCL filter for a single-phase representation connected to a grid [53]**.**

An LCL filter is especially useful because it offers 60dB attenuation after its resonant frequency, and it's always smaller than the switching frequency, allowing it to filter sideband voltage harmonics [52]. When choosing the LCL filter parameters, several factors must be considered [52], [54], [55], although a generic guideline may be developed by considering all of them:

- Regulate the converter side inductor's upper and lower limits by regulating the inductor's fundamental voltage drop and current ripple.
- Determine the capacitor's max limit in terms of value and voltage, taking into account the required converter current to charge the capacitor for a smooth synchronization.
- Calculate the inductor value in the grid side by considering the converter's resonant frequency including some margin, as well as the grid side harmonic constraints.
- Examine the LCL's performance with active damping and without active damping.

For a complete design of the converter with an LCL filter, more explicit requirements are needed, such as optimizing the weight of the inductors and capacitors [53] and the DC link voltage [56], however the primary values can be derived as follows:

- Assume the capacitor impedance to be 10 times (10 p.u.) that of the base impedance. Before synchronization and grid connection the capacitor voltage should be 1.0 p.u. by charging it using 0.1 p.u. converter current.

$$C = 0.1 \frac{P_R}{w_1 V_g^2} \tag{64}$$

In the above equation (64), P_R is rated output of the converter, V_g is the voltage of the grid, w_1 is grid fundamental frequency.

- Regulate the voltage drop in the inductance in operation to 10%, ideally 5% for each inductor in the beginning. Else, a greater DC connection voltage is required to ensure current controllability, resulting in increased losses. [55]. Then the converter side inductance can be calculated as follows:

$$L_1 = 0.05 \frac{V_N}{\sqrt{3} I_N} \tag{65}$$

Similar findings can be obtained using other formulations, such as the one proposed in [53].

- Compute the LCL filter's resonant frequency with both inductances equal and verify if there is adequate margin. The grid impedance should be addressed in the resonant frequency calculation and an estimate of its fluctuation should be evaluated to determine its impact on the resonant frequency [52]. The resonance frequency can be achieved using below formula:

$$f_{res} = \frac{1}{2\pi} \sqrt{\frac{L_1 + L_2}{L_1 L_2 C}} \tag{66}$$

L_2 is the grid side inductor with grid equivalent impedance and as considered above the grid side inductor and converter side inductor is equal then L_2 becomes:

$$L_2 = L_1 + L_g \tag{67}$$

- Then K_{res} can be obtained using f_{res} :

$$K_{res} = \frac{f_{res}}{f_s} \tag{68}$$

To prevent resonance issues in the upper and bottom regions of the harmonic spectrum, the resonant frequency must be in the limit of $[10f_1, \frac{1}{2}f_s]$.

For a hysteresis controller it is important to have a switching frequency not more than 3 kHz to reduce the switching losses. The inductor in the converter side has more impact on average switching frequency.

3.6 Synchronous Reference Frame (d-q) Control

Synchronous reference frame control, popularly referred to as d-q control, involves the reference frame transformation of a-b-c vectors to d-q quantities. This transformation module helps to configure the grid current and voltage waveforms into a reference frame that rotates synchronously with the grid voltage. Doing so converts the control variables from ac to dc quantities, making filtering and controlling more efficient [7]. When applying reference frame concepts to a three-phase grid-connected VSC with a constant dc-link voltage and LCL filter, the current control is achieved with either the Proportional+ Resonant (PR) controllers in the alpha-beta frame or the Proportional+ Integral (PI) controller in the d-q frame [57]. In control

systems, Proportional-integral controllers have widespread control applications and the standard mathematical expression of PI controllers[24], [58] can be written as:

$$G_{PI(s)} = K_P + \frac{K_i}{s} \tag{69}$$

Where K_P and K_i are the proportional and integral gains of the transfer function. However, the d-q control structure can be developed using the PI controller in polar (d-q) coordinates and its matrix transfer function can be expressed as:

$$G_{PI}^{(dq)}(s) = \begin{bmatrix} K_P + \frac{K_i}{s} & 0 \\ 0 & K_P + \frac{K_i}{s} \end{bmatrix} \tag{70}$$

For the designed control scheme, two PI controllers are connected to the Active Front End converter to measure the current references that are injected into the utility grid. The operation of the current controlled AFE in the direct-quadrature reference frames is achieved in Figure 28. The Phase Lock Loop (PLL) generates the grid voltage´s phase angle data. The phase information obtained from the PLL helps in the transformation of the grid currents from a-b-c to d-q frames, I_d and I_q. Similarly, the transformation of the d-q voltage is returned to its a-b-c frame with the same phase information. The regulation of I_d and I_q currents based on the current setpoints i_d^* and i_q^* are essential for the bi-directional transfer of active and reactive powers between the VSI and the grid. Since the input power of the AFE converter is provided by a non-varying power source, then the regulation of the DC link voltage can be neglected.

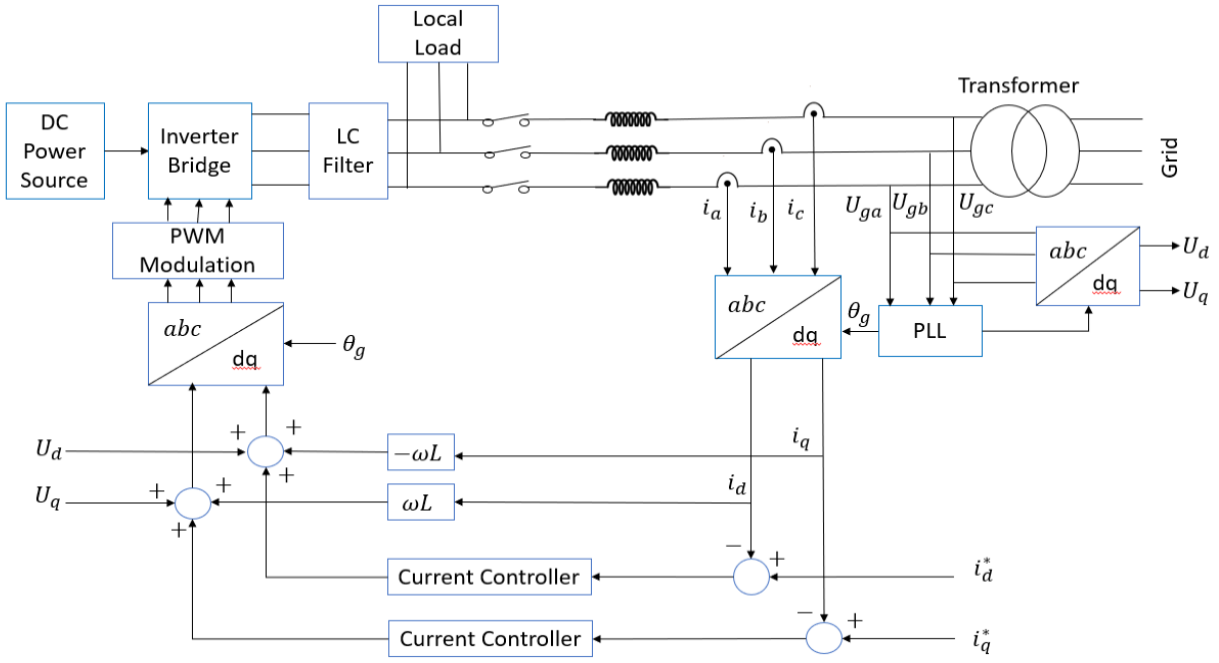

Figure 28:Current Controlled AFE in Synchronously Rotating Reference Frame [24]**.**

An exciting control scheme in Figure 28 is the feed-forward coupling terms of the grid voltage in the d-q reference frame U_d and U_q, which are combined with the output of the current controllers in the d-q frame. This addition enables the amplitude and phase of the capacitor voltage to be the same as the grid voltage before synchronization. Moreover, the inclusion of cross-coupling terms ($\pm wL$) increases the performance of the d-q PI controllers, ensures quicker response, and better dynamism of control during grid voltage oscillations [7].

PI controllers in d-q coordinates are generally considered a good fit for regulating alternating currents in balanced three-phase networks. Unfortunately, there are limitations to its applications. The application of the PI control scheme is not effective when there are unbalanced load conditions as it is unable to adjust unbalanced disturbance currents unless positive- and negative sequence currents are treated independently. Besides, PI controllers exhibit poor performance when compensating for low-order harmonics. Simultaneously, the synchronously rotating reference frame ensures independent control of active and reactive grid currents, allowing the possibility of adjusting the setpoints for the real and reactive power delivered to the grid.

3.7 Stationary Reference Frame (Alpha-Beta) Control

Stationary Reference Control slightly differs from the d-q control mentioned earlier. It is a control structure that transforms from the a-b-c grid current vectors into stationary reference frame alpha-beta coordinates, as depicted in Figure 29. The control scheme is often used due to PI controllers' inability to eliminate the steady-state errors during the control of sinusoidal waveforms. Proportional Resonant (PR) controllers operate in the alpha-beta mode and are widely used in the current control of AFEs. A general matrix transfer function expression of PR controllers in alpha-beta frame can be expressed as:

$$G_{PR}^{(\alpha\beta)}(s) = \begin{bmatrix} K_P + \dfrac{K_i \cdot s}{s^2 + \omega^2} & 0 \\ 0 & K_P + \dfrac{K_i \cdot s}{s^2 + \omega^2} \end{bmatrix} \tag{71}$$

Where ω is the resonance frequency of the controller, K_P and K_i represent the proportional and integral gains respectively.

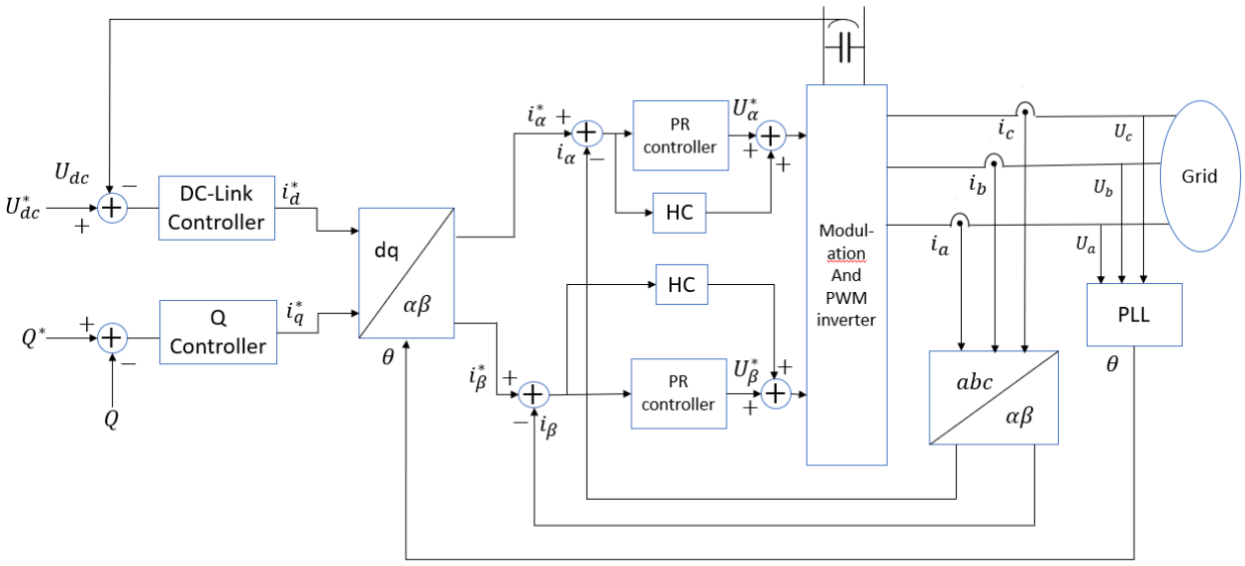

Figure 29: Stationary Reference Frame Control Strategy [7].

This control strategy transforms three-phase a-b-c grid currents into stationary reference frame $i_\alpha$and i_β currents through the a-b-c to alpha-beta transformation module. The alpha quantity represents the phase-a vector, and the beta-quantity is a union of the phase-b and phase-c current signals under balanced conditions. These alpha-beta current signals are controlled using two PR controllers and a Phase-Lock Loop, which obtains the phase information of the grid voltage and is used in generating the i^*_α and i^*_β reference signals from d-q current references (d-q to alpha-beta transformation). Most PR controls have harmonic compensation, which ensures tracking of the alpha-beta reference currents by the actual alpha-beta currents signals. Afterwards, the output of the PR controllers is transformed to the a-b-c frame before conversion into PWM or hysteresis signals for switching. The d-q current signals still maintain the bi-directional transfer of active and reactive power as this control depends on grid voltage. However, an essential feature of the alpha-beta control strategy in Figure 29 is that the PR controller can attain a huge gain close to the resonance frequency, making it possible to eliminate the steady-state error between the control signal and its set point. The limit of the frequency band around the resonance point depends on the integral time constant K_i. A small $K_i$creates a narrow band and vice-versa [24].

3.8 Natural Reference Frame Control

A Natural Reference Frame control is another control method that develops three separate controllers for the a-b-c grid currents. Although, when designing such a natural reference frame controller, careful consideration must be made regarding the star or delta configurations of the three-phase network. For neutral networks in isolation, two controllers are sufficient since there is an interaction amongst the current signals and the third current can be obtained by applying Kirchhoff's current law. Still, it is possible to have 3 unconnected controllers so far; they are being designed in a hysteresis or dead-beat control case. The high

level of dynamism of a bang-bang controller makes it the best choice for natural reference frame control.

Furthermore, developing the a-b-c controllers using digital signal processing or FPGA improves the controller performance. Figure 30 shows the design of the grid-tie inverter in a-b-c, where the output signal of the dc-link voltage controller gives the setpoints for the d-q current reference. The phase information of the grid voltages provided by the PLL helps in generating the a-b-c current references. The individual current references are compared with their corresponding measured current signals, and current controllers adjust the errors. When hysteresis controllers are used, the output signals become the modulator for the converter's switching operations. If PI or PR controllers are used for the design, the modulator will have to be used to generate duty cycles or PWM signals.

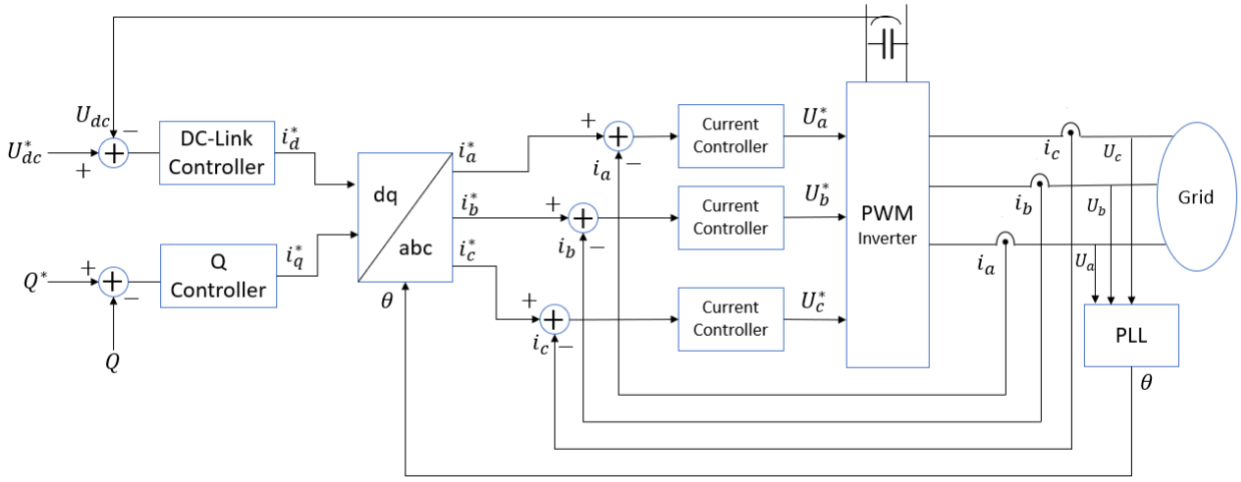

Figure 30: Natural Reference Frame Control Strategy [7]***.***

As discussed in previous sections, the d-q and alpha-beta frames can be expressed in the natural reference frame control. The PI controller implemented in the d-q frame is equivalent to the Proportional-Resonant controller implemented in the alpha-beta frame at the fundamental frequency. The matrix transfer function of the PI controller in the a-b-c frame as developed by [59] is:

$$C_{PIabc}(s) = \begin{bmatrix} K_P + K_i\frac{s}{s^2+\omega^2} & -\frac{K_P}{2} - \frac{K_i s + \sqrt{3}K_i\omega}{2(s^2+\omega^2)} & -\frac{K_P}{2} - \frac{K_i s - \sqrt{3}K_i\omega}{2(s^2+\omega^2)} \\ -\frac{K_P}{2} - \frac{K_i s - \sqrt{3}K_i\omega}{2(s^2+\omega^2)} & K_P + K_i\frac{s}{s^2+\omega^2} & -\frac{K_P}{2} - \frac{K_i s + \sqrt{3}K_i\omega}{2(s^2+\omega^2)} \\ -\frac{K_P}{2} - \frac{K_i s + \sqrt{3}K_i\omega}{2(s^2+\omega^2)} & -\frac{K_P}{2} - \frac{K_i s - \sqrt{3}K_i\omega}{2(s^2+\omega^2)} & K_P + K_i\frac{s}{s^2+\omega^2} \end{bmatrix} \quad (72)$$

The equation (72) above is the PI controller in an a-b-c frame. The PI control consists off-diagonal elements which are representations of a Proportional+Resonant control combined

with non-diagonal cross-coupling terms. These terms indicate that the three-phase signals are dependent on each other. For unbalanced networks, the lack of independence of the three-phase system could pose a challenge. However, the PR controller has an easy implementation in the natural reference frame. As mentioned before, the a-b-c phases can be connected to three independent PR controller, with the current setpoints obtained from I_{dref} and I_{qref} based on the d-q to a-b-c transformation module. The transfer function matrix in the a-b-c frame derived by [60] is written as:

$$C_{PRabc}(s) = \begin{bmatrix} K_P + K_i \frac{s}{s^2+\omega^2} & 0 & 0 \\ 0 & K_P + K_i \frac{s}{s^2+\omega^2} & 0 \\ 0 & 0 & K_P + K_i \frac{s}{s^2+\omega^2} \end{bmatrix} \quad (73)$$

The equation (73) above enables the application of the PR controller for three-phase systems in the alpha-beta reference frame.

3.9 Low Pass and High Pass Filters in Reference Frame

A low pass filter (LPF) allows low-frequency signals and rejects signals that are beyond the cutoff frequency of the filter frequencies. Conversely, the high-pass filter expels signals below its frequency. According to [61], the low pass and high pass filters for PI controllers developed in d-q and alpha-beta frames can be expressed with the following equations:

$$LPF_{dq}(s) = \frac{1}{1 + T_{Lp}s} \quad (74)$$

$$LPF_{\alpha\beta}(s) = \begin{bmatrix} \frac{1 + T_{Lp}s}{(1 + T_{Lp}s)^2 + (\omega_1 T_{Lp})^2} & 0 \\ 0 & \frac{1 + T_{Lp}s}{(1 + T_{Lp}s)^2 + (\omega_1 T_{Lp})^2} \end{bmatrix} \quad (75)$$

$$HPF_{\alpha\beta}(s) = 1 - LPF_{\alpha\beta}(s) = \begin{bmatrix} \frac{T_{Lp}s(1 + T_{Lp}s) + (\omega_1 T_{Lp})^2}{(1 + T_{Lp}s)^2 + (\omega_1 T_{Lp})^2} & 0 \\ 0 & \frac{T_{Lp}s(1 + T_{Lp}s) + (\omega_1 T_{Lp})^2}{(1 + T_{Lp}s)^2 + (\omega_1 T_{Lp})^2} \end{bmatrix} \quad (76)$$

3.10 Phase Lock Loop (PLL)

The phase angle for grid voltage is a critical piece of information for the systems that are coupled with the grid. This phase angle is used to control the flow of real and reactive power, switch on/off of the power devices and the conversion of the control variables into a suitable reference frame that is desirable for a particular control. This phase angle can be determined by using a Phase-Locked Loop (PLL) [62]. A general block diagram of a conventional PLL is shown in Figure 31. It has a Phase Detection unit (PD), a loop filter (LF), and a voltage-controlled oscillator (VCO). The PD block determines the phase difference between the input and the produced output signal, and then it feeds that signal to the loop filter unit to extract the DC component of the phase error. This Dc component needs to be amplified before it goes into the PI controller to generate the output signal frequency [24]. To form the phase angle, the output signal is integrated. When the output signal of the PLL is locked with the input frequency, the phase difference from the PD unit will be 0.

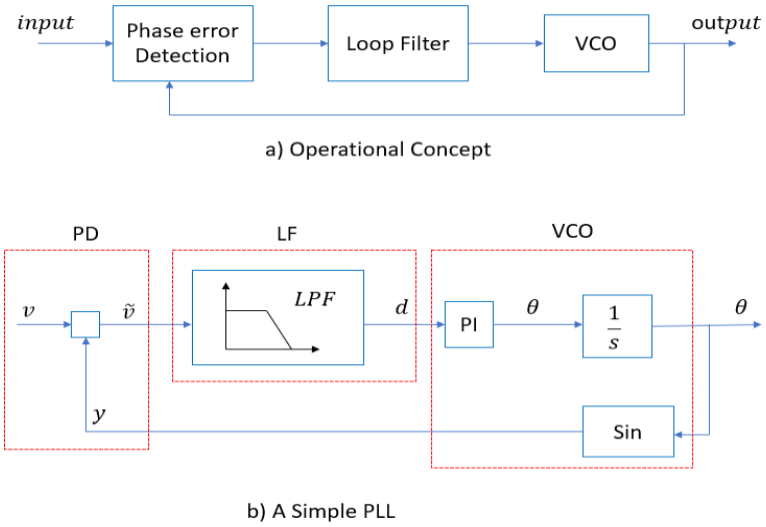

Figure 31: Conventional block diagram of a PLL [24]***.***

If an input signal $v = V_m cos\theta_g$ with a phase of $\theta_g = w_g t + \varphi_g$ and an output signal $y = sin\theta$ with phase $\theta = wt + \varphi$ is passed through the PD unit then the output error signal from the PD will be;

$$v = vy = V_m sin\theta\ cos\theta_g = \frac{V_m}{2}\sin(\theta - \theta_g) + \frac{V_m}{2}\sin(\theta + \theta_g) \tag{77}$$

This term can be rewritten as

$$\frac{V_m}{2}\sin[(w - w_g)t + (\varphi - \varphi_g)] \tag{78}$$

And

$$\frac{V_m}{2}\sin[(w + w_g)t + (\varphi + \varphi_g)]. \tag{79}$$

Equation (78) is low-frequency component, and it has the phase difference between v and y whereas equation (79) is a high-frequency component which is not considered, and it can be filtered out with the loop filter. The output from the loop filter is then;

$$d = \frac{V_m}{2}\sin[(w - w_g)t + (\varphi - \varphi_g)] \tag{80}$$

This signal passes through the PI to generate the frequency w=θ until $d = 0$. To form the phase $y = sin\theta$ the output frequency from the PI is integrated and then it is fed back to the PD unit to complete the control loop. In steady state $\theta = \theta g$.

To control the DC component d to zero, the input signal and output signal are 90° phase shifted.

3.10.1 PLL in the Synchronous Rotating Reference Frame (SRF-PLL)

For a three-phase system a PLL in synchronously rotating reference frame is mostly used. A simple block diagram can be seen below.

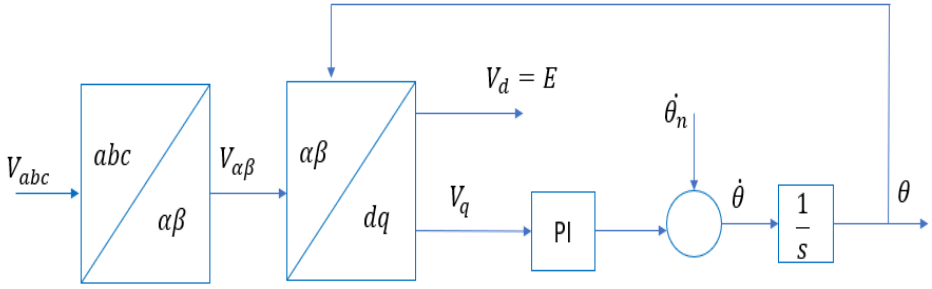

Figure 32: Three phase PLL in the synchronously rotating reference frame (SRF PLL) [24]**.**

A three-phase voltage vector in natural frame $v_{abc} = [v_a\ v_b\ v_c]^T$ can be transformed into synchronously rotating reference frame vector $[v_d\ v_q]^T$ by using the Clarke transformation then the Park transformation.

The Clarke transformation is,

$$v_{\alpha\beta} = \begin{bmatrix} v_\alpha \\ v_\beta \end{bmatrix} = \begin{bmatrix} 1 & -\frac{1}{2} & -\frac{1}{2} \\ 0 & -\frac{\sqrt{3}}{2} & \frac{\sqrt{3}}{2} \end{bmatrix} v_{abc} = T_{\alpha\beta} \times v_{abc} \tag{81}$$

Then the park transformation,

$$\begin{bmatrix} V_d \\ V_q \end{bmatrix} = \begin{bmatrix} cos\theta & -sin\theta \\ sin\theta & cos\theta \end{bmatrix} v_{\alpha\beta} = T_{dq} \times v_{\alpha\beta} \tag{82}$$

Any three-phase voltage vector,

$$\begin{bmatrix} v_a \\ v_b \\ v_c \end{bmatrix} = \begin{bmatrix} E\cos\theta_g \\ E\cos\left(\theta_g - \frac{2\pi}{3}\right) \\ E\cos\left(\theta_g + \frac{2\pi}{3}\right) \end{bmatrix} \tag{83}$$

So,

$$\begin{bmatrix} V_d \\ V_q \end{bmatrix} = \begin{bmatrix} E\cos(\theta - \theta_g) \\ E\sin(\theta - \theta_g) \end{bmatrix} \tag{84}$$

Where,

$$E = \sqrt{v_d^2 + v_q^2} \tag{85}$$

$[v_d\ v_q]^T$ are two DC component vectors V_d and V_q in SRF. The input signal will be locked into the phase when $V_q = 0$ in the steady-state, and to achieve that, the V_q component will be fed into a PI controller. The output from the PI controller is the estimated frequency, which will give the phase angle by integrating it further. The voltage amplitude E can also be calculated by equation (85). The amplitude of the voltage vector E becomes the same with the d component of the SRF during the phase lock. So, in SRF PLL all the three quantities of frequency, amplitude, and phase are available. Throughout the process, the calculated θ is the crucial parameter that gives the phase error detection. As V_q is a DC component, the loop filter in the PLL is a unity gain. As discussed earlier, the PI gives the frequency, and the integration of that frequency generates the phase angle, and together these two perform the function of the VCO.

3.11 Active Damping

The inductor-capacitor-inductor or LCL-type filter for inverter-based generation offers a better performance when rejecting switching harmonics, unlike the L-type filter. Various current methods have been discussed for the inverter control, including single loop, grid current and inverter-side current. Still, the controller gains K_P were set to minimum values to maintain stability. The selection of these low gains resulted into low-order harmonics, and occurrence of transients in the networks [63].

It is important to discuss the concept of damping of oscillations between line reactance and filter capacitors (LC or LCL-filter) for line current controlled hysteresis or PWM VSCs. The oscillations exhibited in the LC-filter are due to the resonance between itself and the grid that can be attributed to load variations or grid disturbances. Often the LC resonant excitation can

be caused by harmonic voltages in the grid and harmonic currents generated by the converter. The resonance frequency of a typical LC filter can be expressed as:

$$\omega_{res} = \frac{1}{\sqrt{L_s C_f}} \tag{86}$$

Where ω_{res} is the resonance frequency, L_s line inductance and C_f is the filter capacitor

Studies and reports given by [64], [65] suggest methods of damping of oscillations by adding lead-lag compensated feedback from measured capacitor voltage to the bang-bang or PWM control and the use of a virtual resistor(s) to mitigate the oscillations in the system. It was pointed out by [65] that applying passive damping to a transient oscillation through the application of a resistance can suppress the resonance, but the approach is unfit for high power applications due to the excessive losses that will be incurred in the resistor. However, the active damping strategy proposed for this research entails including closed loop feedback, which controls the capacitor voltage oscillations to zero by contributing the damping components to the three-phase AC current references.

[44] explains the passive and active damping for LC resonance as adding a physical damping resistor R_P to the control circuit, assuming the converter to be a current source. For a pulse With Modulation scenario, the equivalent circuit for an LC-type filter with passive and active damping are illustrated in Figure 33 below.

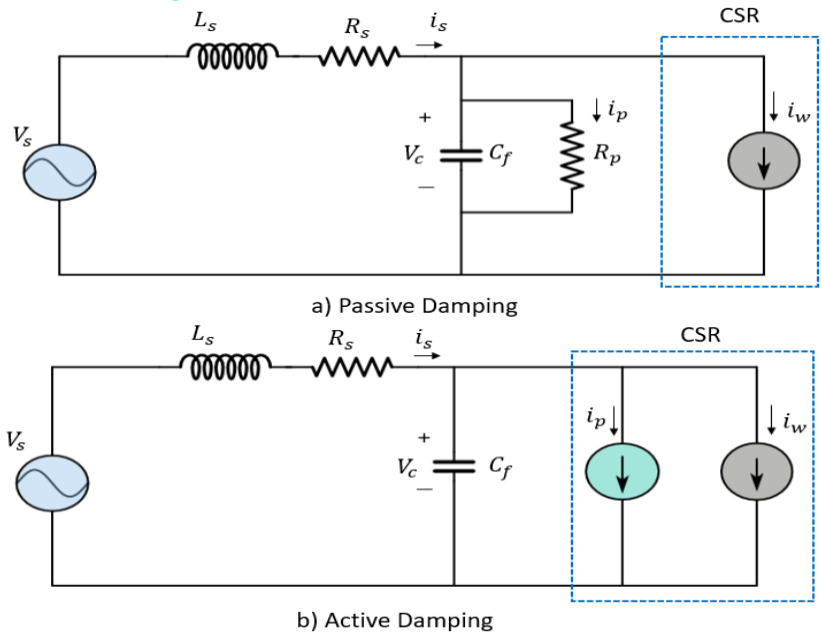

Figure 33: Passive and Active damping [44]**.**

The principle of operation is highlighted as follows:

- Detect the instantaneous capacitor voltage v_c
- Calculate the damping current by $i_p = \frac{v_c}{R_p}$
- Adjust the modulation index m_a dynamically based on the calculated i_p

The circuit's resonances can only be suppressed without power losses if the appropriate value is selected. For an efficient operation of the active damper, the LC resonances at all frequencies must be suppressed, excluding the fundamental component of i_p.

Figure 34 depicts the active damping control process. The capacitor voltage v_c is obtained, and it undergoes transformation from a-b-c to the synchronous reference frame (polar coordinate). The a-b-c to d-q transformation is achieved based on the phase information θ' received from the phase-locked loop (PLL). The fundamental component of v_c in the stationary frame has a d-c equivalent in the synchronous frame. The d-c quantity is extracted with a high pass filter (HPF), and the remaining signal represents the oscillating component or harmonics of the capacitor voltages v_c' in the d-q frame. This harmonic detection method is insensitive to the variations in the supply frequency. The HPF is adjusted to a low cut-off frequency, resulting in a small phase delay at the resonating frequencies.

The damping current i_p' is calculated by the division of v_c' by the desired damping resistance R_p. The reference current i_p' is then converted to the damping modulation index m_a' by resulting to the d-c output current I_d. The damping modulation index m_a' is added to the m_a'' for the d-c current control in the space vector modulator for active damping and d-c current control.

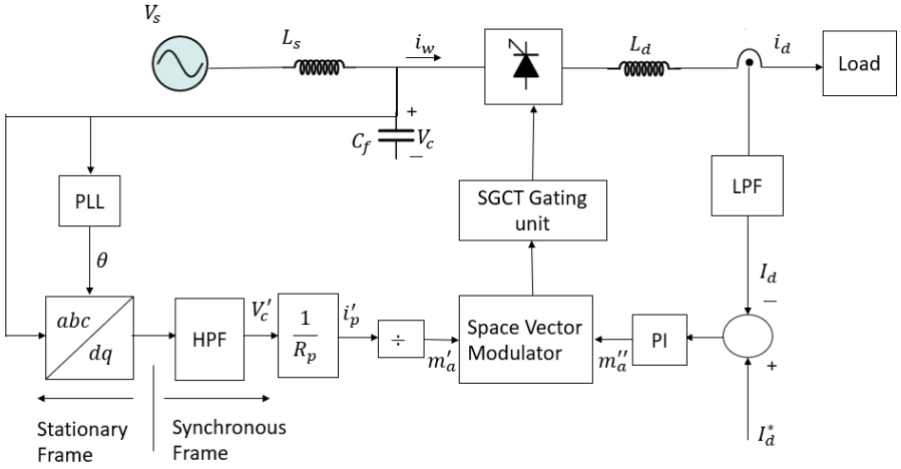

Figure 34:Vector Controlled Converter with active damping control [44].

Alternatively, the active damping control for a two-level three phase voltage source converter can be developed according to [66]:

- The oscillating component of the capacitor voltage is obtained (the non-fundamental component)
- The error in the capacitor voltage is gotten by subtraction of the oscillating component from its reference
- The error is amplified and added to the reference signal for the current controller

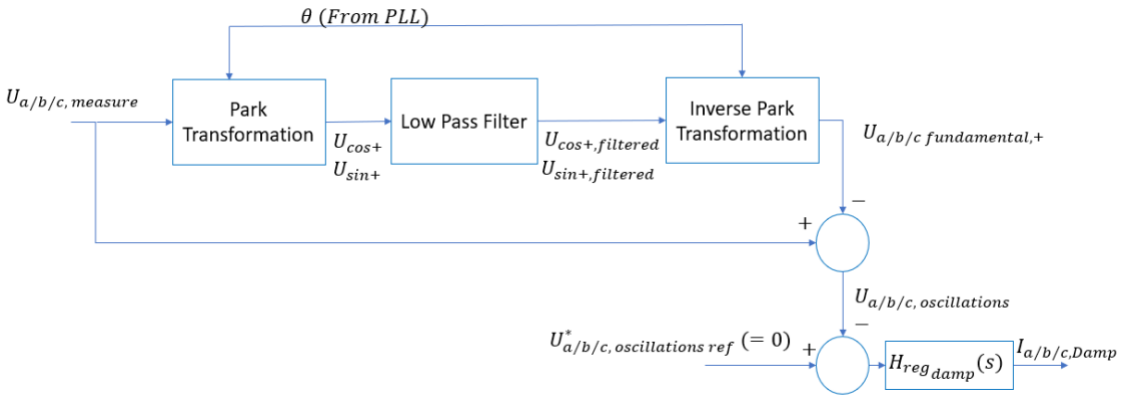

Figure 35: Internal Control Circuit of the Active Damping [66].

In this research, [66] method has been adopted for the suppression of the resonance present in the circuit.

3.12 Synchronization

A synchronization system is an algorithm that validates the conditions of an electrical circuit before activating the closure of a breaker. This synchronization system permits the connection of a major device, such as generating units, and electrical drives, to electric power systems.

To achieve such a connection, three important criteria must be met, according to the pre-set conditions. They are:

- The voltage variation is within the set limit
- The frequency variation is within the set limit
- The phase angle difference is within the set limit

When the electrical connection fulfils all these requirements, the circuit breaker can close the circuit and connect the device with the electric power network. With regards to the voltage level, the synchronization algorithms vary, which can be the following:

- Low and medium voltage level: three pole closing
- High voltage level: monopile closing and three pole closing

Invariably, to reduce the overvoltage transients that might occur due to the connection of a device, the energization of the three phases is achieved in a sequence termed point-on-wave switching. This switching feature is typically deployed for connecting long-distance high voltage transmission lines, reactors, or power transformers. However, point-on-wave switching isn't applicable for medium and low voltage levels because of high-cost implications and design complexities.

The utmost significance of Voltage Source Converter or VSIs is its self-commutating property, i.e., it doesn't require a grid voltage for its switching operations. This feature is highly

beneficial in case of an occurrence of any blackout event in power networks. For grids with the prevalence of HVDC links, VSCs can activate their black start capabilities after a network failure [67]. The fact that an inverter can induce its own voltage like a synchronous generator enables synchronization. To accomplish this feature, the circuit breaker of an AFE is usually installed with the filter capacitor as depicted in the Figure 36 below:

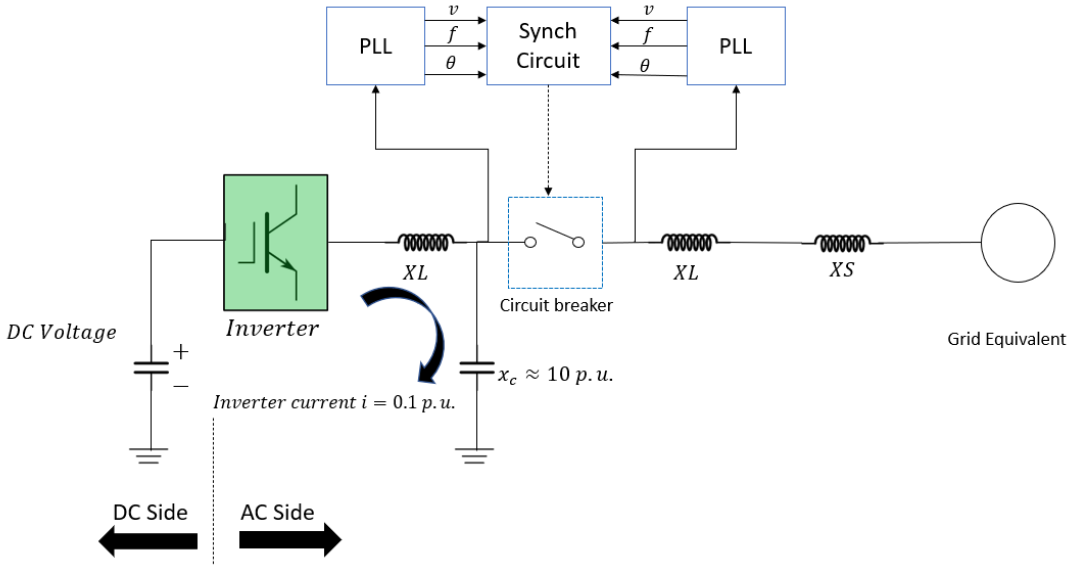

Figure 36: Single Phase Schematic Synchronization of AFE.

The charging current can deliver the required capacitor voltage from the DC link of the inverter. The DC side voltage could either be connected to battery storage (BS) or be an endpoint of a machine-side converter comprising a drive with a motor or generator. For solar technology, it is a direct connection, hence doesn´t require an extra converter.

3.12.1 Normal Operation

Once the circuit breaker closes, the voltage controller increases the voltage level to the reference value (1.0 p.u.) and raises the converter current to the rated value. For a normal operating condition, the voltage and current reach their expected values at the earliest time possible.

In its working condition, the inverter should be able to manage the load designed for voltage fluctuations while maintaining stability. It should also handle non-linear loads and minimize the total harmonic distortion (THD) up to an acceptable limit.

To measure voltages on either side of the breaker and angle reference and frequency on both sides, voltage transformers and two-phase locked loops are needed respectively. Once the capacitor charges up to the desired level and the frequency and angle also meeting the desired limits, the circuit breaker energizes.

Chapter 4

4.0 Modelling of the Active Front End with Virtual Inertia and Damping

In this section, a brief discussion on the control of synchronous generator is highlighted in connection to the filter capacitor voltage-oriented control.

Figure 37 shows a line diagram of a synchronous generator connected to the main grid; e_{af} is the internal voltage of the machine, x_s is equivalent reactance of the machine and u_{grid} is the grid voltage.

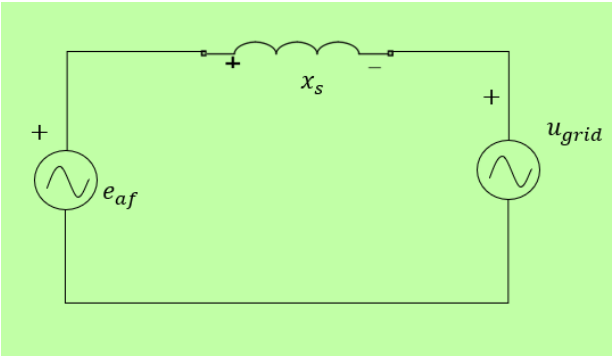

Figure 37: Equivalent Circuit of Grid Connected Synchronous Generator. [68]

The internal voltage of the synchronous machine can be mathematically represented as:

$$e_{af} = \omega . x_s . i_f \tag{87}$$

Where ω is the speed of the synchronous machine and i_f is the field current.

The field current i_f controls the amplitude of the internal voltage of the synchronous machine, and the turbine torque controls the speed ω of the synchronous generator. However, this control strategy can be modelled in the capacitor of the LCL filter in the stator-oriented control.

4.1 Capacitor Voltage control

When connecting the DC link or renewable energy sources to AC networks, the requirements of the LCL filter must be considered. It is essential to prevent fluctuations of the capacitor voltage as an unbalance in voltage can lead to higher ripple voltage across the dc-link capacitor, increased output current ripple and over-voltage stress on some semiconductor devices [69].

In this section, we shall model the control of the filter capacitor battery in the Active Front End Converter. The control strategy of the filter capacitor in the stator-oriented coordinate will be adopted for emulating the behavior of synchronous generators 'behavior and achieving the converter´s synchronization with the grid. Also, the AFE can be designed for various functionalities depending on the control objective. It is used for implementing droop control of active and reactive power, virtual inertia, harmonic compensation, and unbalanced compensation [70]. In this case, the outer control loop is dependent on the capacitor voltage and shall be used for the droop control of active and reactive power, emulation of virtual synchronous machine, and active damping.

The overall control strategy for an Active Front End converter is depicted in Figure 38 below:

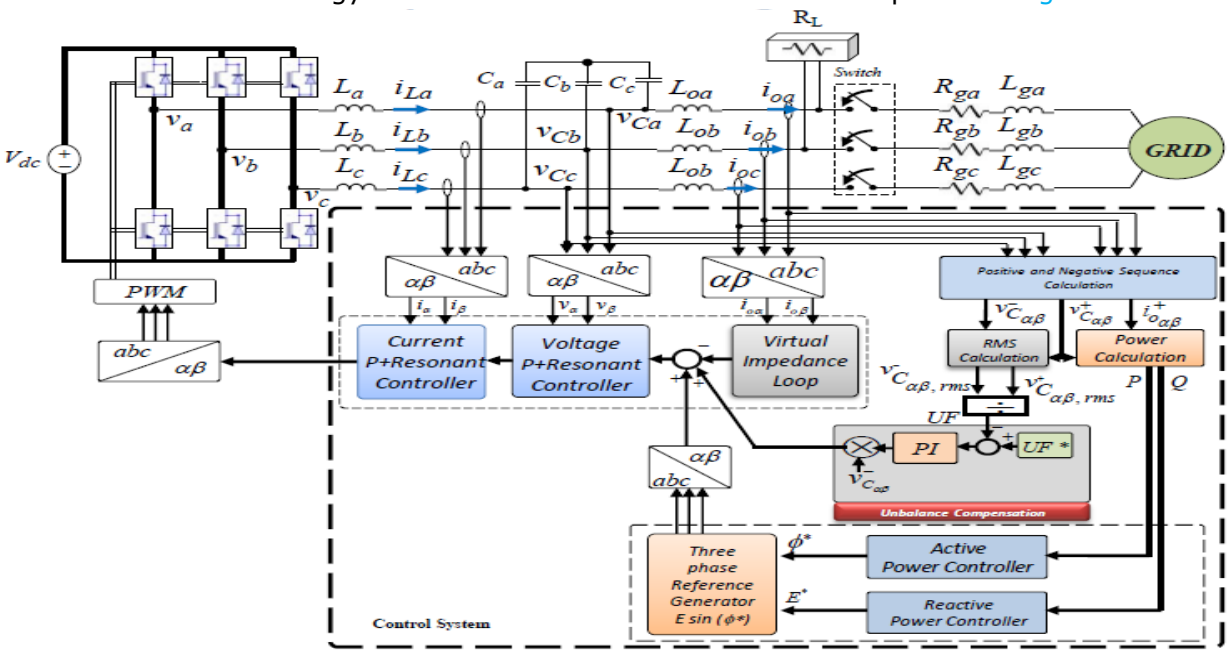

Figure 38: Typical Active Front End Converter Control Strategy [70].

For the main voltage control loop, the controller can be a proportional P, PI or a PI controller with an addition of a resonant controller. Resonant controllers are often added to the voltage control loop to cancel individual harmonics such as the 7th order harmonics. Similarly, the inner current control loop can be designed with the help of a Proportional+Resonant controller as depicted above. However, the P+R current controller and the Pulse width modulation will be replaced by a hysteresis controller for fast response. Also, the PI controller will be used to control the fundamental component of the system. At steady-state, the control of filter capacitor voltage ($\underline{u_c^s}$) is achieved in synchronous reference frame (d-q). In principle, the balance of the capacitor voltage is achieved through the control of the amplitude and frequency during no load and load conditions.

According to Kirchhoff's current law, the algebraic sum of current entering and exiting a node must be equal to zero. Figure 39 shows the path of current leaving the converter and entering the capacitor and the grid (charging and discharging operations). The governing equation for modelling the filter capacitor battery for the Active Front End Converter can be expressed as:

$$\frac{d\underline{u_c^s}}{dt} = \omega_N \,.\, x_c \,.\, \left(\underline{i_1^s} - \underline{i_2^s}\right) \tag{88}$$

Where ω_N is the frequency of the converter. $\underline{i_1^s}$ is active current from converter, $\underline{i_2^s}$ active current of the load.

$$\frac{d\underline{u_c^s}}{dt} = \omega_N \,.\, x_c \,.\, \underline{i_c^s} \tag{89}$$

Equation (90) shows that the $\underline{u_c^s}$ is along the voltage vector which controls the d component (the amplitude).

$$\underline{u_c^s}(t + dt) = \underline{u_c^s}(t) + d\underline{u_c^s}\,(t) \tag{90}$$

Equations (88) to (90) are the expressions for the design of the capacitor voltage control in $\alpha\beta$ reference frame- stator oriented control.

From Figure 39, U_{dc} represents the DC link voltage, the $\underline{u_c}$ is the voltage across the LCL filter, x_c is the capacitance of the filter capacitor in per unit, r_1, x_1 and r_2, x_2 represent the per unit impedances of the converter and grid sides respectively.

The filter capacitor is modelled in u_c oriented coordinates system (stationary DC quantities) to generate the i_{cd} and i_{cq} current reference signals deployed for the switching operations of the VSI. These d-q current references are the output of the amplitude and angle controllers and the input variables to the inner current control loop.

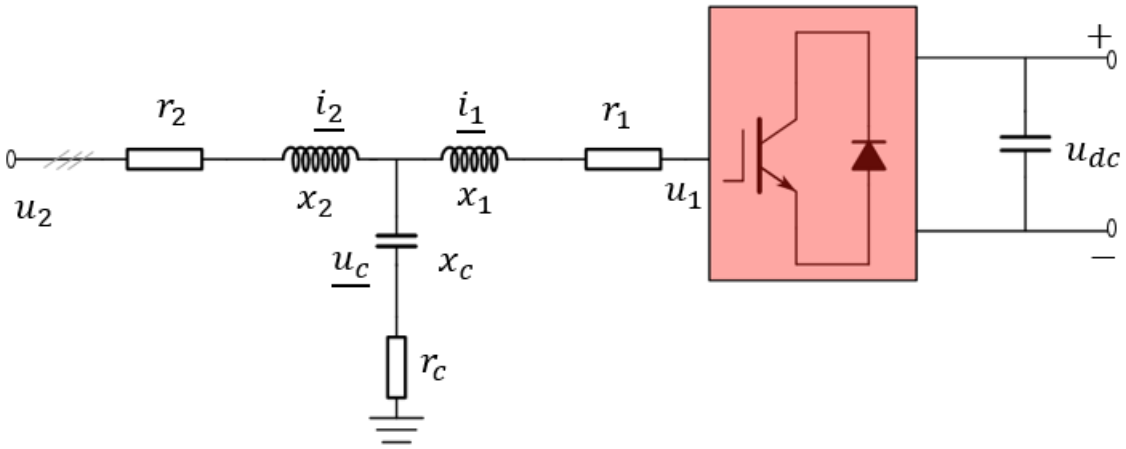

Figure 39: Schematic Diagram of the Control of Capacitor voltage.

The active current i_{1d} is a vector component controlled by the converter. The active current i_{2d} can be categorized as a form of disturbance depending on the load. To ensure steady state

operations, the active current i_{1d} is manipulated with the help of the PI controller to achieve the desired u_c value. This implies that the PI controller increases the i_{1d} up to a point that it becomes the same magnitude with i_{2d}. At this point in the d-axis, the capacitor is neither charging nor discharging, so the amplitude is constant.

The equation for the amplitude PI controller for the filter capacitor can be expressed as:

$$\frac{du_c}{dt} = \omega_N \,.x_c \,.(\, i_{1d} - i_{2d}) \tag{91}$$

$$\frac{du_c}{dt} = \omega_N \,.x_c \,.(i_{cd}) \tag{92}$$

The q-axis component which is orthogonal to the d-axis component is used in generating the reactive current i_{cq}. The q-axis can be oriented to align with the d-axis component. The reactive current can be expressed in relation with the frequency as:

$$\frac{du_c}{dt} = 0 = \omega_N \,.x_c \,.\big(i_{cq}\big) - \,\omega_N \,.f_k \,.u_c \tag{93}$$

To achieve a desired frequency f_k on the rotation of the vector u_c, this frequency is dependent on the reactive current i_{cq}, and the voltage u_c. For the d-q reference frame, the feed-forward current i_{cq} term based on the frequency of the grid is added to the input of the angle controller.

$$i_{cq} = \frac{f_k \,.u_c}{x_c} \tag{94}$$

Where f_k is the frequency of u_c.

The equation for the angle PI controller can be represented as:

$$\frac{d\delta_c^s}{dt} = \omega_N \cdot f_k = \frac{\omega_N \cdot x_c}{u_c} \cdot i_{cq} \tag{95}$$

When comparison is made between the synchronous machine and the capacitor voltage control the following observations can be drawn:

- The amplitude of the voltage vector e_{af} of the synchronous generator is cotrolled by field current i_f
- The speed ω of the synchronous generator is controlled by the turbine torque $\tau_{turbine}$
- The amplitude of the capacitor voltage vector u_c^s is controlled by the active current i_{1d}
- The frequency of the capacitor voltage vector f_k is controlled by the reactive current i_{cq}

4.2 LCL Dimensioning

4.2.1 For the analogue system

As described in section 3.5 earlier for LCL filter design, the capacitance and inductance have been calculated.

$$C = 0.1\frac{P_N}{w\,V_g^2} = 0.1\frac{1.72}{377 \times 690^2} = 958.27\ \mu F$$

Here the converter rated power in MW, and the angular frequency is in rad/s. A value of 800 μF was chosen because it shows better performance in the simulation than the calculated value.

For the inductance,

$$L_1 = \ 0.05\frac{V_{SN}}{\sqrt{3}I_{SN}} = 0.05\frac{690}{\sqrt{3} \times 1250} = 15.9\ mH$$

A value of 57 μH chosen for better performance in simulations.

4.3 Virtual Inertial Control (Modelling)

In conventional power systems monopolized by synchronous generators, whenever there is a sudden change in power balance due to disturbance, stabilizing the power is usually done by the natural response of the rotor or rotating mass (inertia compensation) and governor action (primary control). Conversely, the domination of the modern-day power systems by converter-based generation units limits the natural response of the rotating mass to any disturbance; hence their reduction in inertia compensation which results in rapid frequency variations with wide-ranging amplitudes. Unrestrained RoCoF could take place, resulting into the cascaded tripping if generators are not configured to ride through. Supposing system inertia drops considerably, the massive generation loss will lead to the rapid frequency drop that under frequency load-shedding would initially occur, creating stability issues, cascading outages, and power blackouts [16].

In this section, we will emulate the mechanical system of a synchronous machine in the AFE converter.

The concept of virtual inertia is based on the swing equation and droop control:

$$T_m\frac{dn}{dt} + \ d_{DQ}(n - f\_ref) = T_{turbine} - T_{g,syn} \tag{96}$$

Where T_m is the mechanical time constant relating to the inertia to be emulated by the VSI controller. $\frac{dn}{dt}$ is the rate of change of speed, d_{DQ} represents the droop gain of the virtual inertia, f_ref is the frequency set point which determines how much power will be delivered,

$T_{turbine}\ and\ T_{g,syn}$ are the turbine and synchronization torque in the system, and $d_{DQ}(n - f_{\_ref})$ represents the damper winding.

According to Newton's second law of motion,

$$J\frac{d\omega}{dt} = T_{turbine} - T_{e,g} \tag{97}$$

Where $T_{turbine}$ is the driving torque and the $T_{e,g}$ is the load torque

In practical application, the loading of the turbine is achieved through the synchronization and damper winding. Then, $T_{e,g}$ can be expressed as;

$$T_{e,g} = T_{g,syn} - T_{g,damp} = T_{g,syn} - d_{DQ}(\omega_s - p.\omega_{mech}) \tag{98}$$

$T_{g,damp}$ is the damper winding torque which is a function of slip that exist in induction motors with shorted rotor bars. Then substituting equation (98) into (97) gives:

$$J\frac{d\omega}{dt} + d_{DQ}(\omega_s - p.\omega_{mech}) = T_{turbine} - T_{g,syn} \tag{99}$$

The synchronization torque $T_{g,syn}$ can be represented in terms of generator power $P_{g,syn}$ and flux ψ as:

$$T_{g,syn} = \frac{P_{g,syn}}{n} = \frac{e_{af}\ .u_{grid}}{n\ .x_s}\ .sin\delta \tag{100}$$

$$T_{g,syn} = \frac{\psi_{af}\psi_s}{x_s}.\ sin\delta \tag{101}$$

Where ψ_{af} is field winding flux, ψ_s is stator flux, δ is the angle between flux or voltage, and n is the speed of the generator.

If we linearize the synchronization torque $T_{g,syn}$ around a certain angle, it becomes:

$$T_{g,syn} = \frac{\psi_{af}\psi_s}{x_s}.\ sin\delta \approx \frac{\psi_{af}\psi_s}{x_s}.\ cos\delta_o.\delta \tag{102}$$

In equation (102) the $\frac{\psi_{af}\psi_s}{x_s}.\ cos\delta_o$ term can be interpreted as gain and it changes depending on the point of operation, then the equation can be re-written as follows,

$$T_{g,syn} = K_1.\delta \tag{103}$$

K_1 can be interpreted as gain from the equation above which changes depending on the point of operation.

Also, the derivative of the pole angle can be given by:

$$\frac{d\delta}{dt} = \frac{d\theta}{dt} = \frac{d\delta_s^s}{dt} = \omega_N \,.(n - f_{\_ref}) \tag{102}$$

Now, introducing equation (96) into the s domain, one can show that:

$$T_m.s.n(s) + d_{DQ}.(n - f_{\_ref}) = T_{turbine} - T_{g,syn} \tag{103}$$

Finally, the virtual inertia control based on swing equation can be written as:

$$T_m.s.n(s) = \left(d_{DQ} + \frac{\omega_N.K_1}{s}\right).(f_{\_ref} - n) + T_{turbine} \tag{104}$$

Based on the equation above, the damper winding represents the expression of a PI frequency controller.

$$K_p + \frac{K_i}{s} \approx d_{DQ} + \frac{\omega_N.K_1}{s} \tag{105}$$

Then, the inertia emulation can be designed in Simulink. Figure 40 shows the design of the virtual inertia control.

Supposing f is designed to be a stiff grid (constant amplitude) and compared with the speed of the generator, the PI frequency controller will supersede the turbine controller. The $f_{\_ref}$ is a frequency set-point that determines how much power will be delivered. The control system won't attain the desired reference frequency due to the rigidity of the grid frequency. On the contrary, the reference frequency $f_{\_ref}$ or can only attain its desired value based on the appropriate settings of the damper windings and the synchronization torque $T_{g,syn}$. As shown in equation (107) above, the damper winding is represented with a P controller. Power is delivered if the reference frequency $f_{\_ref}$ is higher than the grid frequency f.

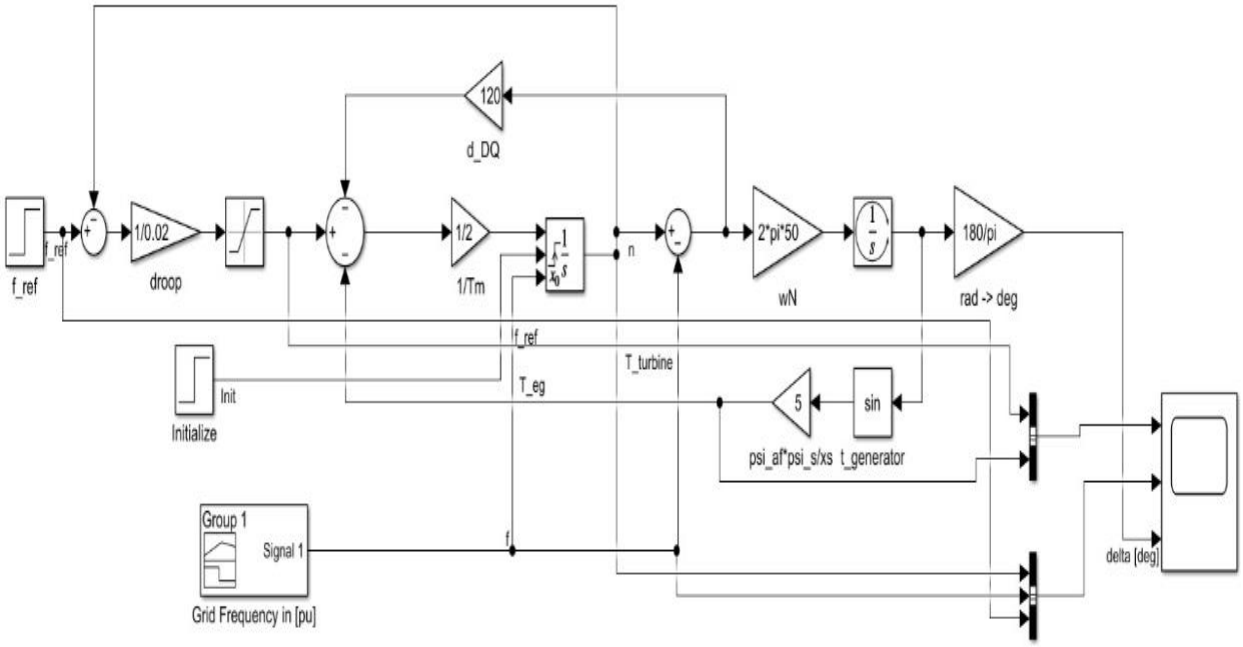

Figure 40: Simple Virtual Inertial Control Model from Simulink.

In Figure 41, the graphical results of the virtual inertial modelling in Simulink are displayed and the interpretation of the outputs is discussed.

At 1 second, the frequency reference $f_{\_ref}$ increases beyond the nominal value of the grid frequency f (1.0 p.u. or 60Hz). This step-change creates a disturbance in the speed n, at that instant of time but quickly re-aligns with the grid frequency because of the restrictions of the damper winding. A step-change $f_{\_ref}$ increases the turbine torque from 0-0.5 p.u. but the speed n, of the turbine remains the same in steady-state. This constant speed is decided by the characteristics of the grid frequency. However, a sudden variation in speed n, will result to a corresponding trip in the system.

From 5 to 7 seconds, the grid frequency drops by 6% and the frequency or the speed of the VISMA follows the grid frequency. Currently, the difference between $f_{\_ref}$ and speed n, increases, which increases the magnitude of the turbine and generator torque. A slight increase in $T_{e,g}$ decelerates the system and later tracks the torque of the turbine. At this point, the machine is braking. After that, the system maintains a constant speed and frequency values for an additional 3 seconds.

For 10-12 seconds, the grid frequency increases again and the difference between $f_{\_ref}$ and speed n reduces, which subsequently reduces the magnitude of the generator torque. At this point, the machine accelerates (generation mode). The generator torque $T_{e,g}$ becomes less than the turbine torque and more active power is supplied to the grid. After 12 seconds, the grid frequency is restored to 1.0 p.u., and the speed perfectly tracks the grid frequency. In addition, the grid frequency stabilizes for 2 seconds and beyond.

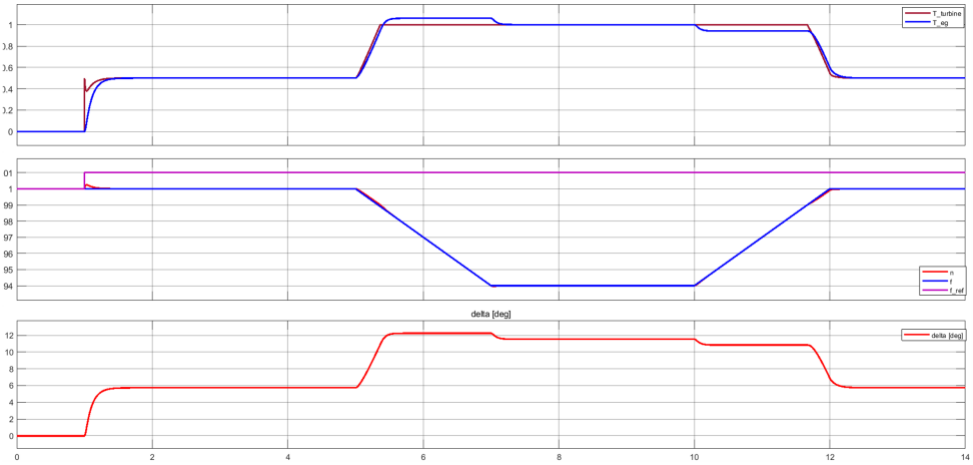

Figure 41: Simulink Results of the Virtual Inertia Control.

Chapter 5

5.0 Typical design for AFE with virtual inertia and damping in Simulink

5.1 Power and control circuit of AFE

The layout of the inner current control loop and voltage control loop designed for the AFE is shown in Figure 42:

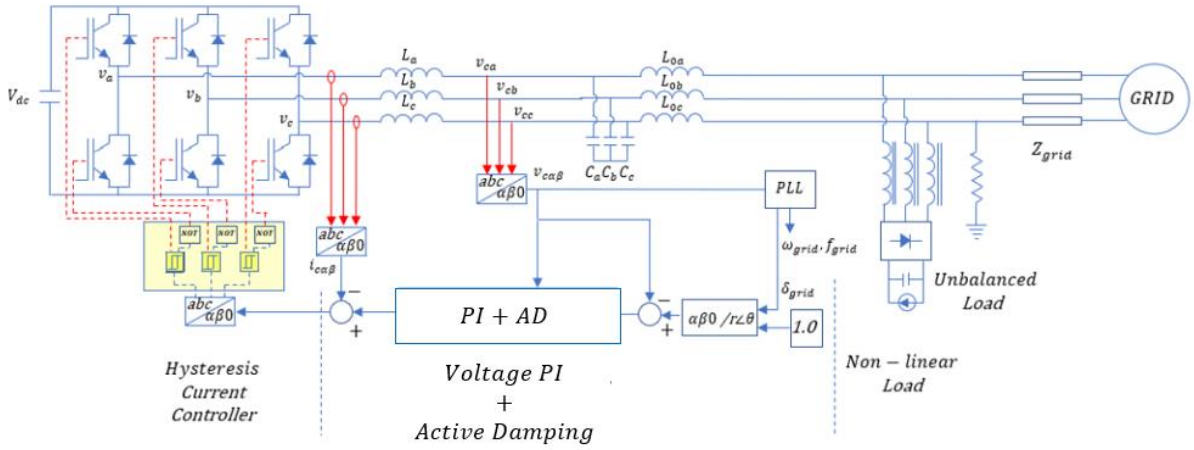

Figure 42: Overall Power and Control scheme of the Active Front End Converter.

The circuit shows the connection of the voltage loop PI controllers in the stationary reference frame (alpha-beta) and active damping. The PI controllers generate the current references that serve as input to the hysteresis controller. The scheme considers a connection to a stiff grid, and non-linear load. Also, the disconnection of grid is put into consideration.

5.2 Synchronization Unit

The synchronization circuit implemented in Simulink is shown in Figure 43. Phase-Locked Loops were generated for the grid and converter to measure the grid angle ($\delta_{grid}\ PLL$) and converter angle ($\delta_{conv}\ PLL$) signals. Similarly, the grid and converter frequencies are obtained from the PLL. The grid and capacitor voltages were measured. Overall, the voltage, frequency, and angle of the grid PLL and the Inverter were compared to ensure that the errors ($u_{error}, angle_{error}, freq_{error}$) generated do not exceed the set requirement. As shown in Figure 44, logic gates are developed to generate signals that make decision for the closing of the circuit breaker.

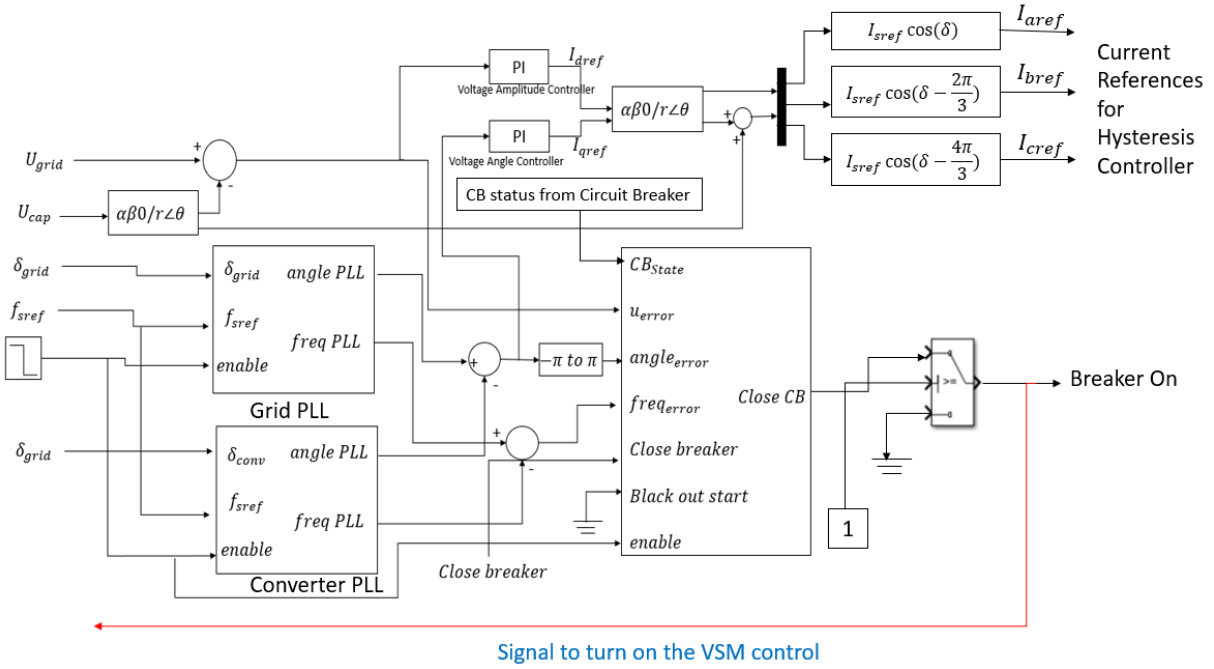

Figure 43: Synchronization Control layout implemented in Simulink.

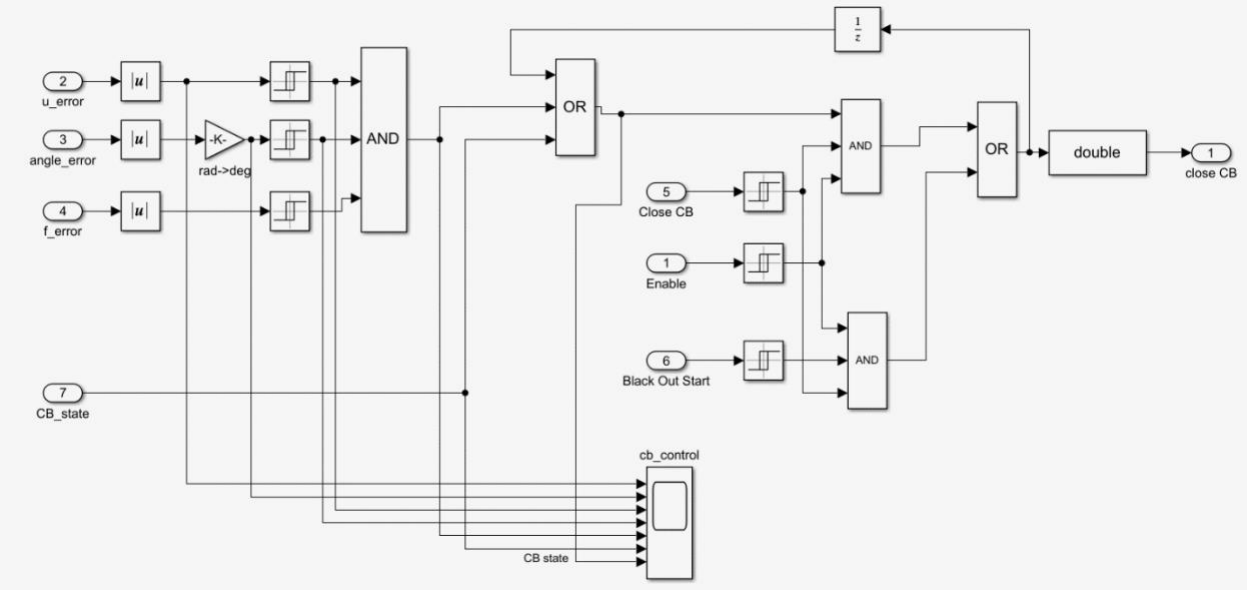

Figure 44: Synchronization Logic circuit in Simulink.

5.3 Virtual Synchronous Machine in $\alpha\beta0$ coordinate system

The comprehensive implementation of the virtual inertia control in stationary reference frame coordinates are explained below:

The current references $I_{s\alpha\beta}$ are the outputs (outer voltage control loop) of the scheme developed in Figure 45. The current references are converted from the $\alpha\beta\ to\ abc$ reference frame. These triple signals serve as input current references for the inner current control loop. To achieve the control of the virtual synchronous machine in $\alpha\beta$ coordinate system, the frequency of the grid and the capacitor voltage are essential signals for this control algorithm.

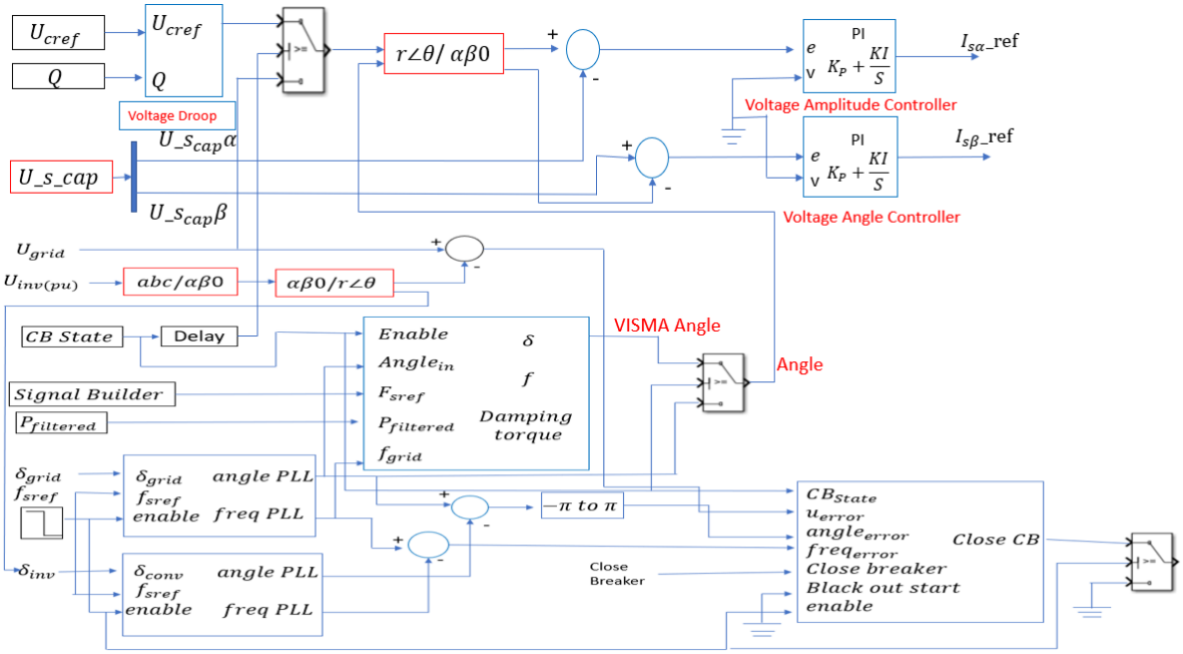

Figure 45: Control scheme of virtual inertia emulation implemented in Simulink.

5.4 Virtual Synchronous Machine in dq coordinate system

Figure 46 shows a similar implementation of the virtual synchronous machine in the polar coordinate system. The variation of d-q coordinate system from the $\alpha\beta$ reference frame is that the capacitor voltage amplitude and angle are the basic vectors for this control mechanism. The output of these controller is the direct and quadrature reference currents which are DC quantities. The PI controllers are responsible for effective tunning of the voltage amplitude and angle of the filter capacitor to generate the desired current references for the inner current control loop. The angle of the capacitor voltage vector is added to the $I_{q_{ref}}$ to rotate the voltage vector to ensure the frequency of the inverter aligns with the grid frequency. In contrast to harmonic compensation in $\alpha\beta$ reference frame, the $I_{d_{ref}}\ and\ I_{q_{ref}}$ current references are DC signals use to avoid dealing with possible harmonics that could exist in the fundamental frequency.

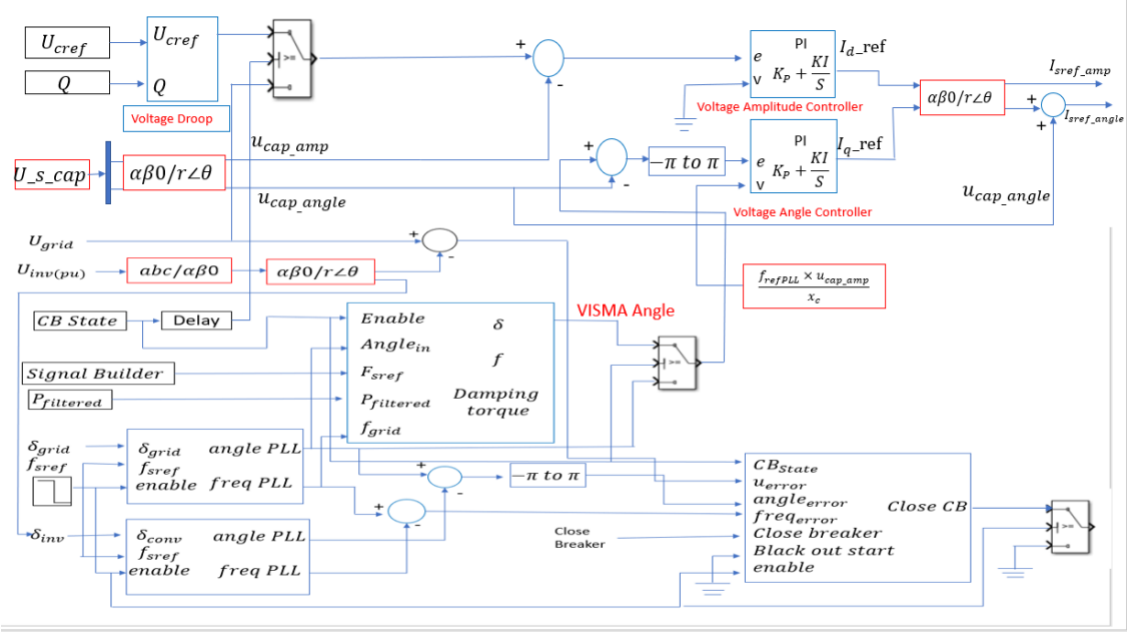

Figure 46: Control scheme of virtual inertia emulation implemented in Simulink.

5.5 Tuning of the PI controllers using Symmetrical optimum

Figure 47, shows the tuning algorithm established for the voltage amplitude and angle PI controllers used for the filter capacitor. As discussed in section 2.5.4, the K_p *and* T_i of the controllers can be achieved with the help of the flow chart. K_s is for power balance, β represents the degree of freedom of the control system. The selection of the higher magnitude of β corresponds to slower response but more damped system and vice versa. In our case, the PI controllers created optimal performance when β was set to 4.

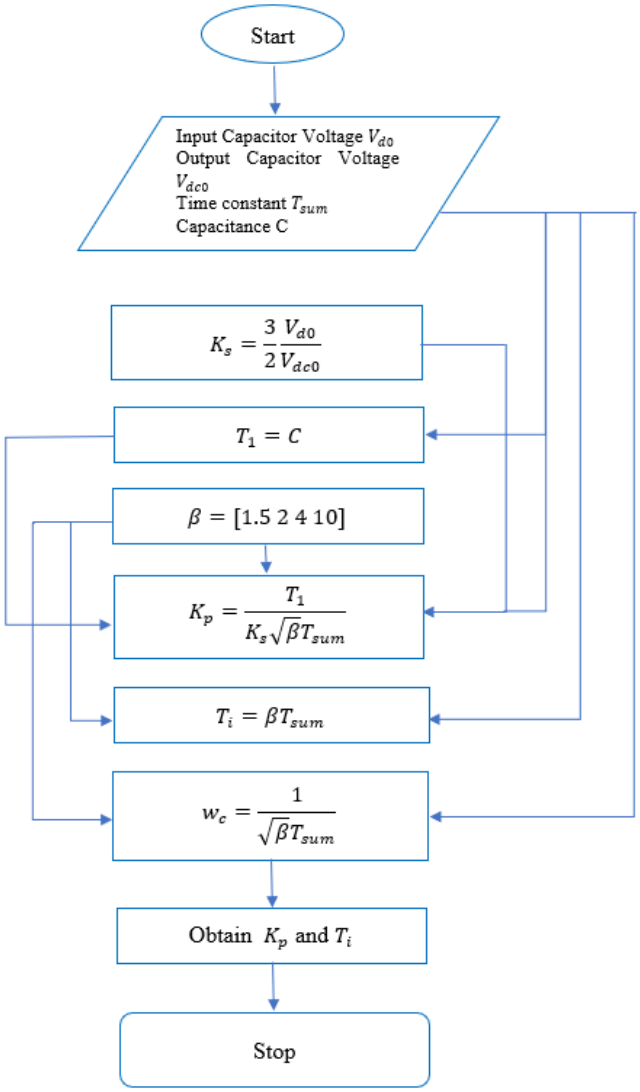

Figure 47: Flow chart representation of tuning PI controller.

Chapter 6

6.0 Simulation results

6.1 Analogue model in alpha beta coordinate system

6.1.1 Grid Synchronization and breaker closing

From the Figure 48, the breaker closes at 0.511s and there are noticeable oscillations in the active power during breaker closing. The oscillations settle down to 0 in 0.2s. The steady-state operations are achieved after 0.9s. The grid voltages and inverter voltages look stable at this instant of time.

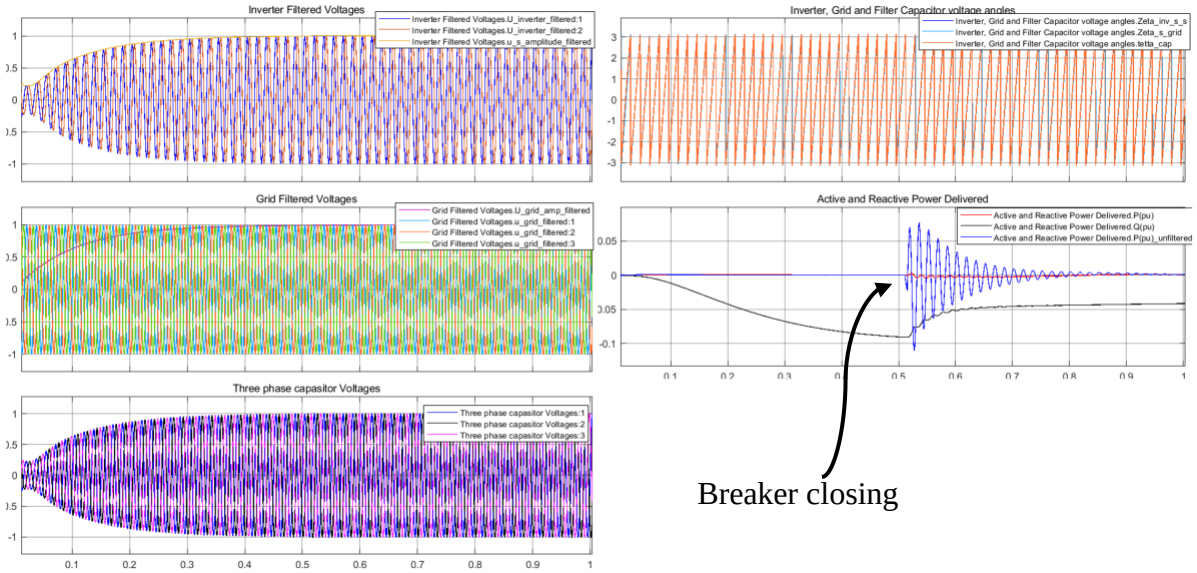

Figure 48: Voltage, Power and Phase measurements for Inverter, Grid and Capacitor during the breaker closing (alpha-beta reference frame).

In Figure 49, the alpha-beta signals for the PI controllers are represented. The capacitor voltage references are obtained through the combination of amplitude and angle of the grid voltage before synchronization. Likewise, the capacitor voltage signals serve as the actual values compared with the reference signals mentioned before to generate the possible errors that will be sent to PI controllers. The steady-state of the capacitor voltage is observed from Figure 49.

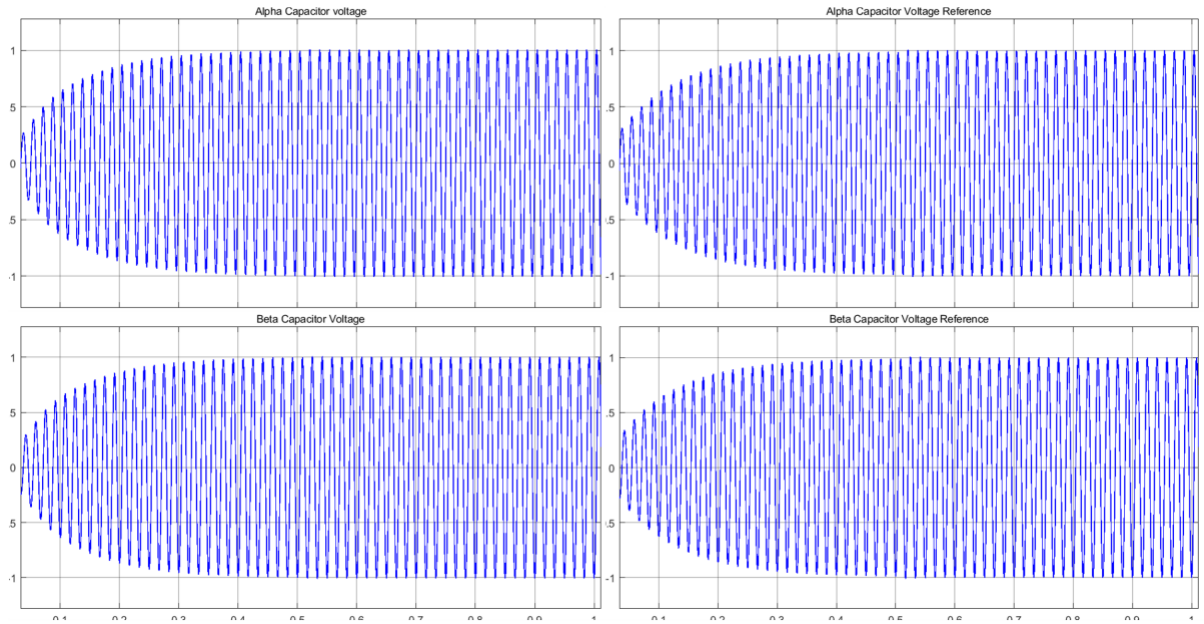

Figure 49: Capacitor and grid voltage references in alpha-beta coordinate system.

Figure 50 shows the oscillations of the alpha-beta current references from PI controllers during breaker closing. It is observed that the reduction of the oscillations occurred after 0.511s. This current reference signals are used for switching operation of the converter.

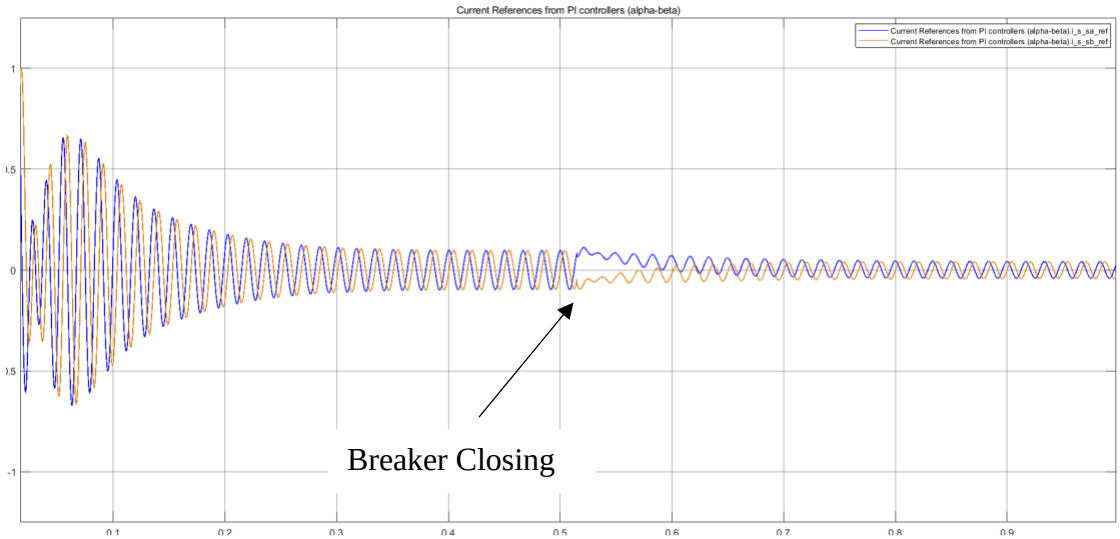

Figure 50: Alpha-Beta Current References from the PI controller during breaker closing.

Figure 51 shows the PLL and VISMA outputs. The Angle error (difference between the Grid PLL angle and Inverter angle) exceeded the set limit before 0.15s. Also, the Grid angle from the PLL and VISMA angle are in phase even before breaker closing. The phase information from the grid PLL allows the initialization of the VISMA by the grid.

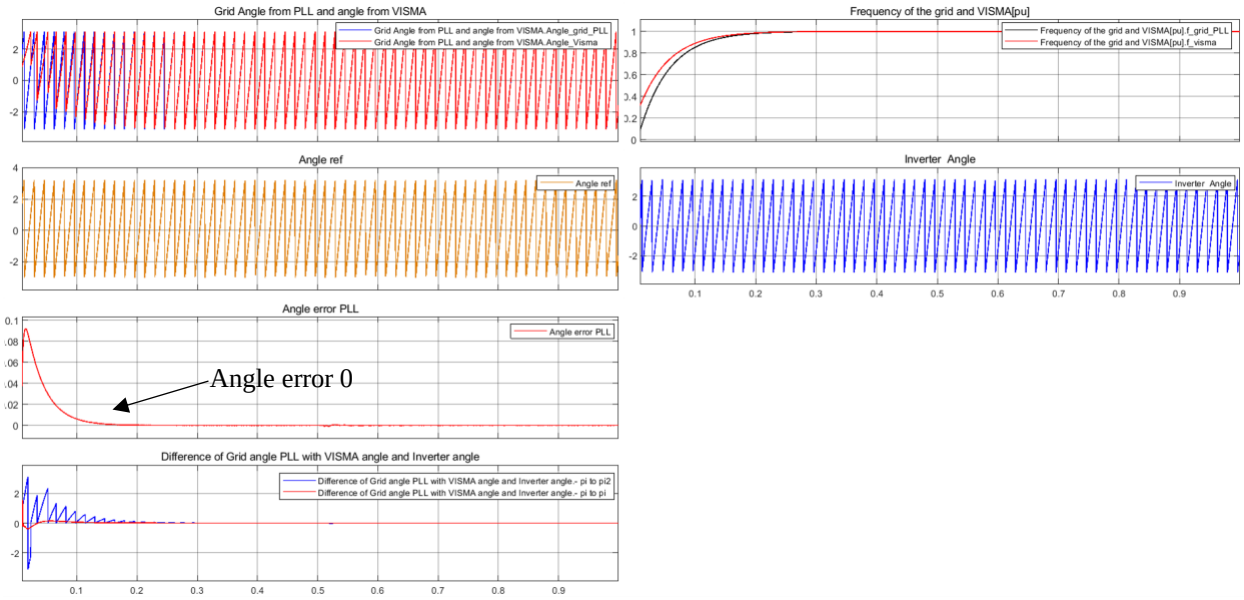

Figure 51: PLL and Visma Phase angle outputs before connecting the breaker and increasing the frequency set point (f_{sref}).

After the grid synchronization, various scenarios were considered for testing the working operation of the filter capacitor voltage, PI controllers, and VISMA. Figure 52, Figure 53, Figure 54, Figure 55, Figure 56 will depict the characteristics of the power and control circuit of the AFE during each scenario.

6.1.2 Scenario 1: Grid Connected mode

As earlier mentioned, the AFE system synchronized at 0.511s (Figure 52). The operation of the converter starts delivering the power to grid at 1.2s. An increase in the f_{sref} at that instant of time contributed to delivery of power. Figure 52 shows the filtered and unfiltered active power signals with varying oscillations. At 1.8s, the connection of a non-linear load demands more power from the converter. The steady state condition was achieved at 2.5 seconds.

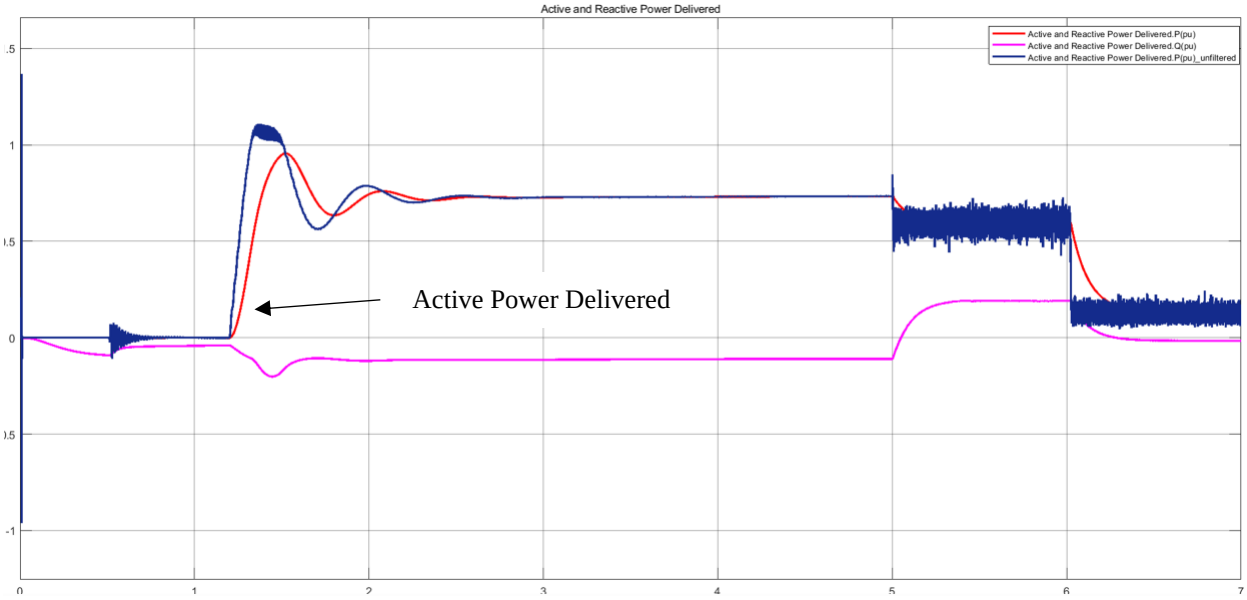

Figure 52: Active and Reactive Power outputs from the converter.

Figure 53 shows the corresponding response of the current references in $\alpha\beta 0$ reference frame during synchronization and when the converter is delivering active power to the grid and load. At 1.2s the current references go into saturation due to the limit block, which can be avoided by increasing the limit from 1 to 1.5 for the current controllers.

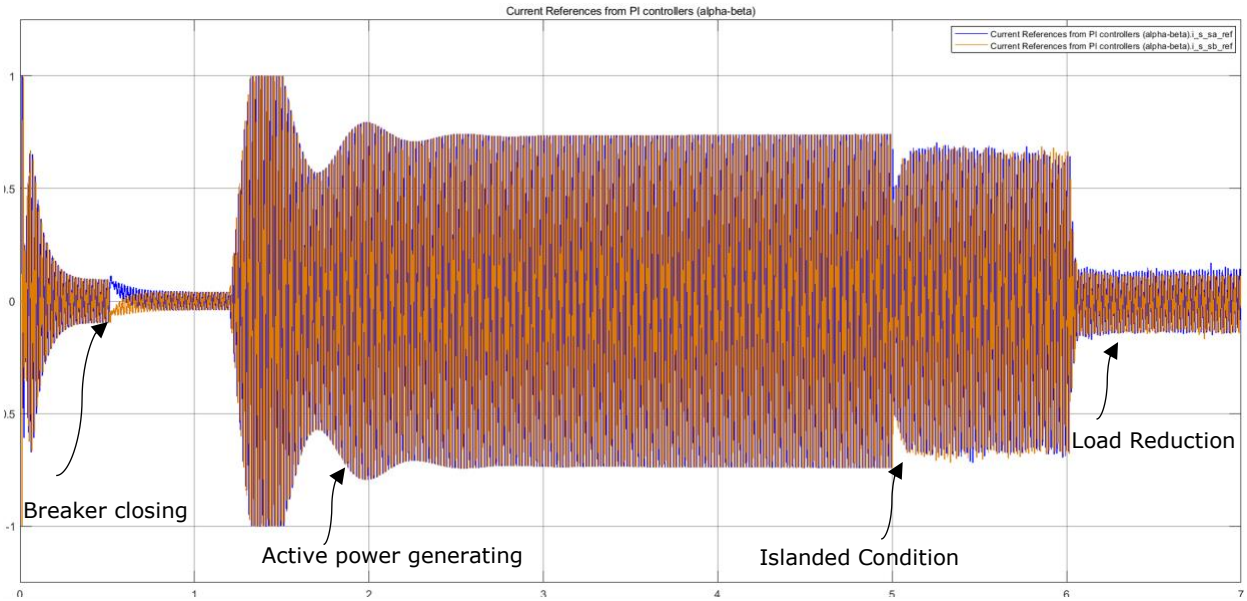

Figure 53: Alpha-Beta Current references from the PI controllers (All scenarios).

Figure 54 shows some oscillations at around 1.3s in the angle error, which are caused by the saturation of the current controllers. As discussed earlier, these oscillations can be avoided by increasing the limit for the alpha-beta current controllers.

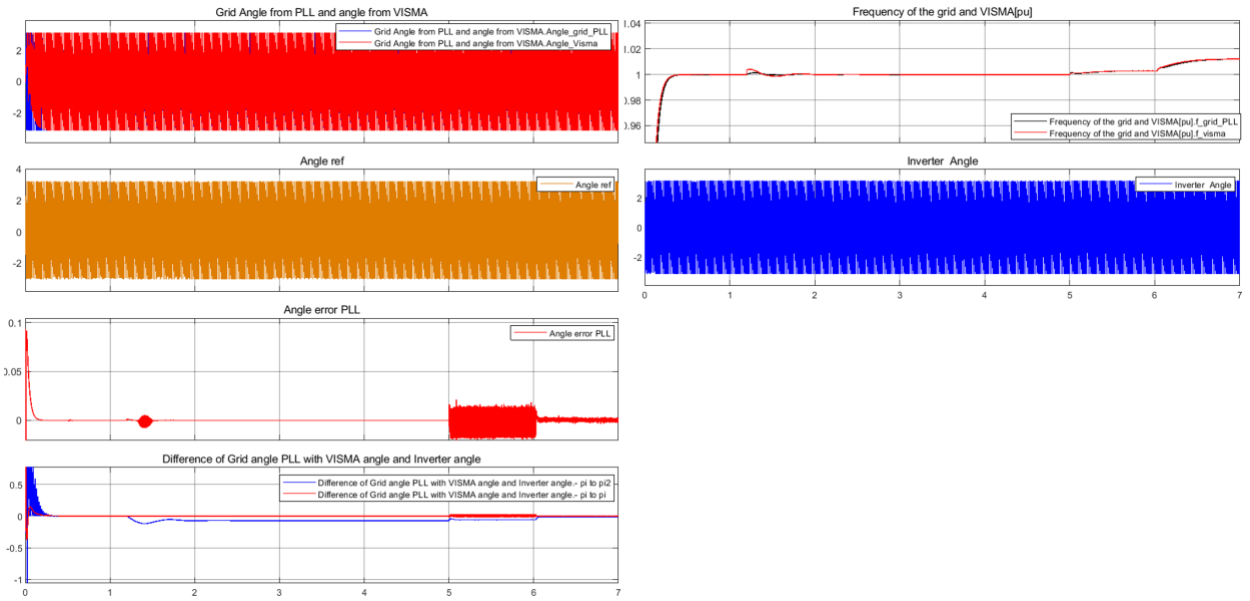

Figure 54: PLL and Visma Phase angle outputs in alpha-beta reference frame (All Scenarios).

6.1.3 Scenario 2: Island Mode

From Figure 52, the system´s operation was considered in island mode at 5s. There was a drop in active power due to a disconnection from the grid. The circuit breaker between the grid and the converter trips. The converter goes into island mode, which reduces the power supplied to the load and grid. At 6s, the load demand drops down from 800kW to 100 kW. As a testament to this scenario, the alpha-beta current references in Figure 53 had corresponding reduction in magnitudes between these time intervals. In Figure 54, there was a massive increase in the angle error between the grid PLL and the inverter caused by a 6^{th} order harmonic due to the presence of the diode rectifier load. Also, at 6s the load drops down to 100kw, which reduces the harmonics.

Figure 55 shows that the response of the virtual synchronous machine emulated in the active front-end converter. The system´s behavior is a representation of the virtual inertia control modeled in (96). An increment in f_{sref} and connection of non-linear load between 1.2s to 1.8s resulted in system oscillations. Later, the system maintained a high degree of stability. The speed *n* follows the grid frequency up until the point of islanding. At 5s, the grid frequency is out of the system and the speed of the machine was observed to track the frequency of the virtual inertia emulation. At 7s, both frequency set-point and machine speed achieve the same speed as there was a proportional reduction in the generator torque.

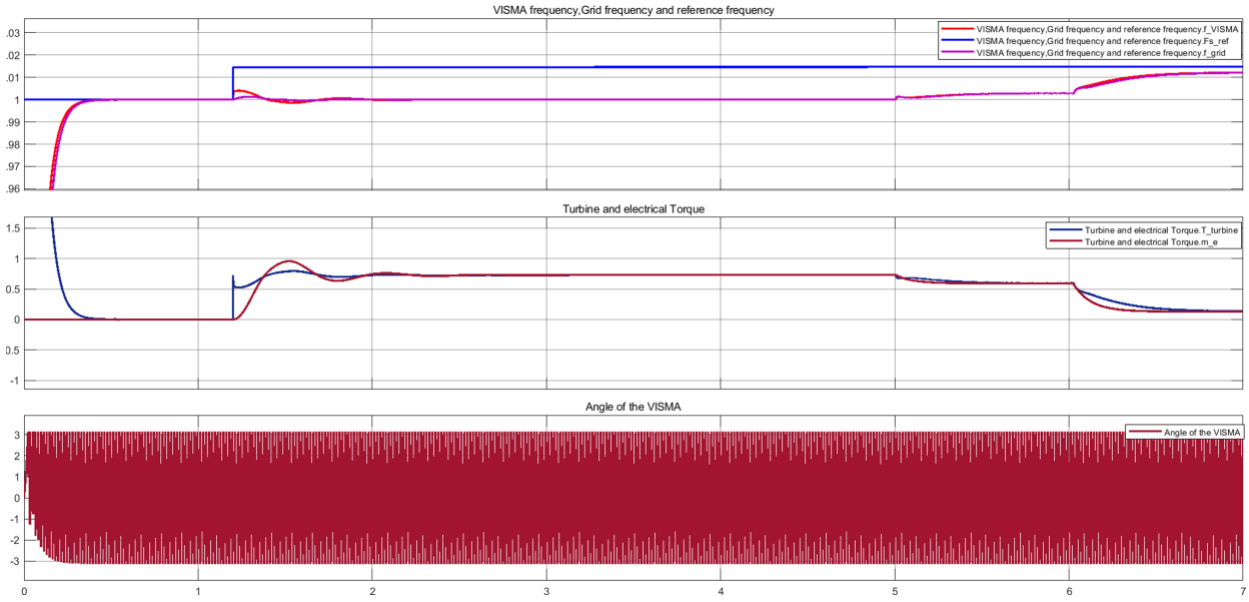

Figure 55: Frequency and angle responses of the VISMA (alpha-beta) during power generation.

In Figure 56, the relationship between the power delivered to the grid and the existing damping of the VISMA is simulated. The damping torque is responsible for stabilizing frequency deviations to maintain control and system stability. When the active power starts getting delivered at 1.2s, the damping torque opposes the sudden changes in frequency to ensure the stability of power being supplied to the grid. During islanding condition, a reduction in power resulted in a corresponding damping torque because of grid disconnection and increased machine speed.

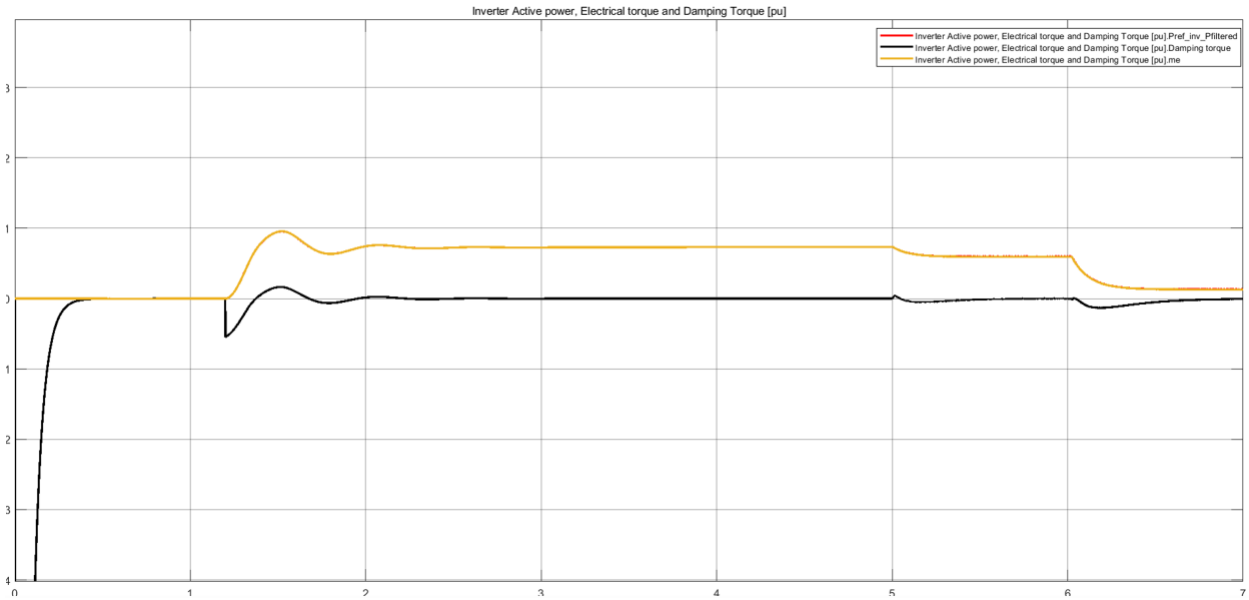

Figure 56: Electrical and damping torque responses of the VISMA in alpha beta reference frame.

6.1.4 Scenario 3: Grid Frequency Deviations

Figure 57 and Figure 58 are the responses of the VISMA during under/over frequency conditions. As stated earlier, the VISMA has been modelled to emulate the characteristics of the grid. At 3s the properties of the grid frequency were manipulated to investigate the response of the system to changes in frequency. An increase or a decrease in grid frequency by 1% was considered, which resulted in a corresponding increment and decrement of the VISMA. These imply that power delivered to grid can be more or less under actions taken on the stiff grid.

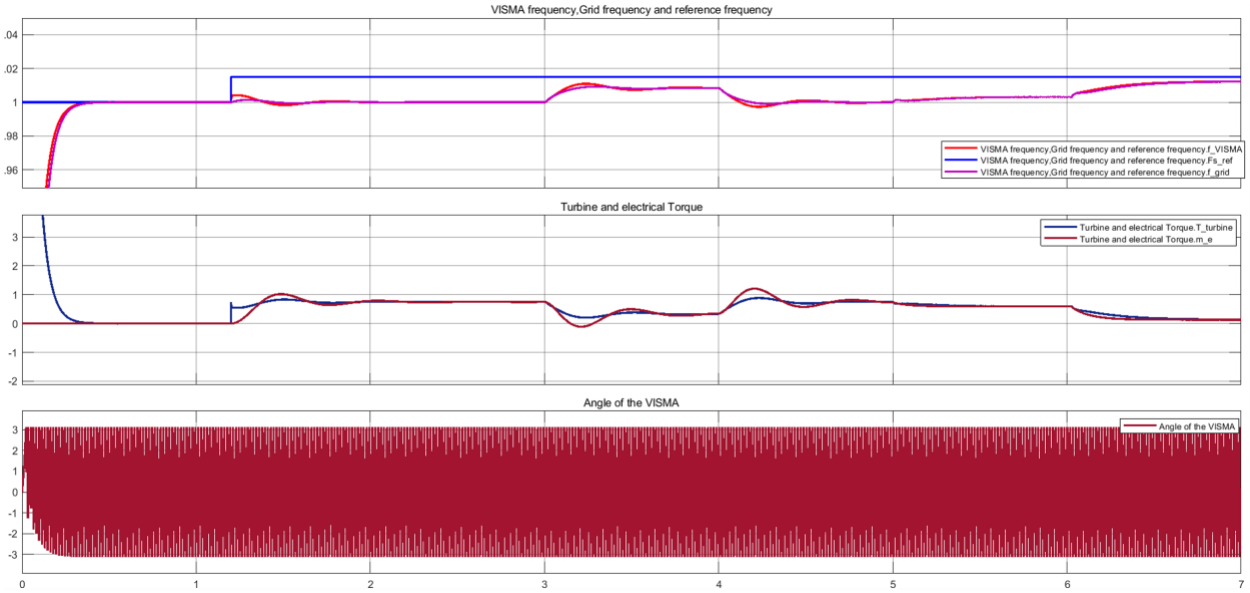

Figure 57: Performance of the VISMA during grid frequency deviation (over frequency).

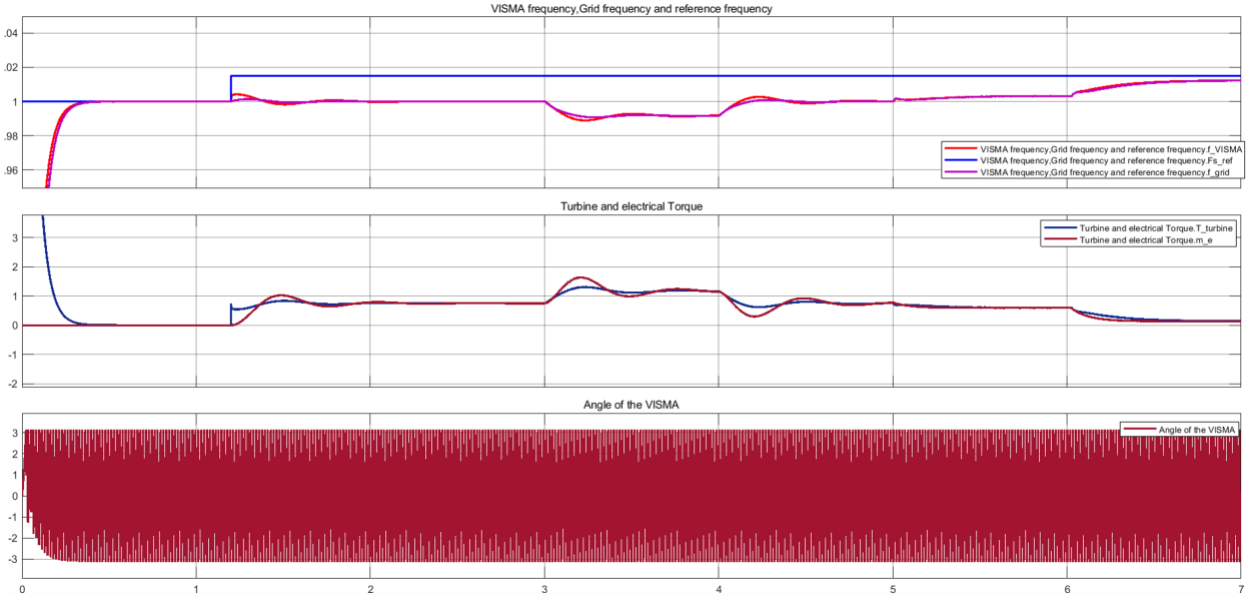

Figure 58: Performance of the VISMA during grid frequency deviation (under frequency).

6.2 Analogue model in polar coordinate (d-q) system

In this section, the outputs of the scenarios considered for the alpha-beta reference frame shall be discussed.

6.2.1 Grid Synchronization and breaker closing (d-q)

Figure 59, represents the voltage measurements of the grid, the inverter and filter capacitor in the direct-quadrature axis transformation. The synchronization of the inverter to the grid was achieved 0.711s. it is observed that the voltage frequency and phase requirements of the system was achieved before breaker closing.

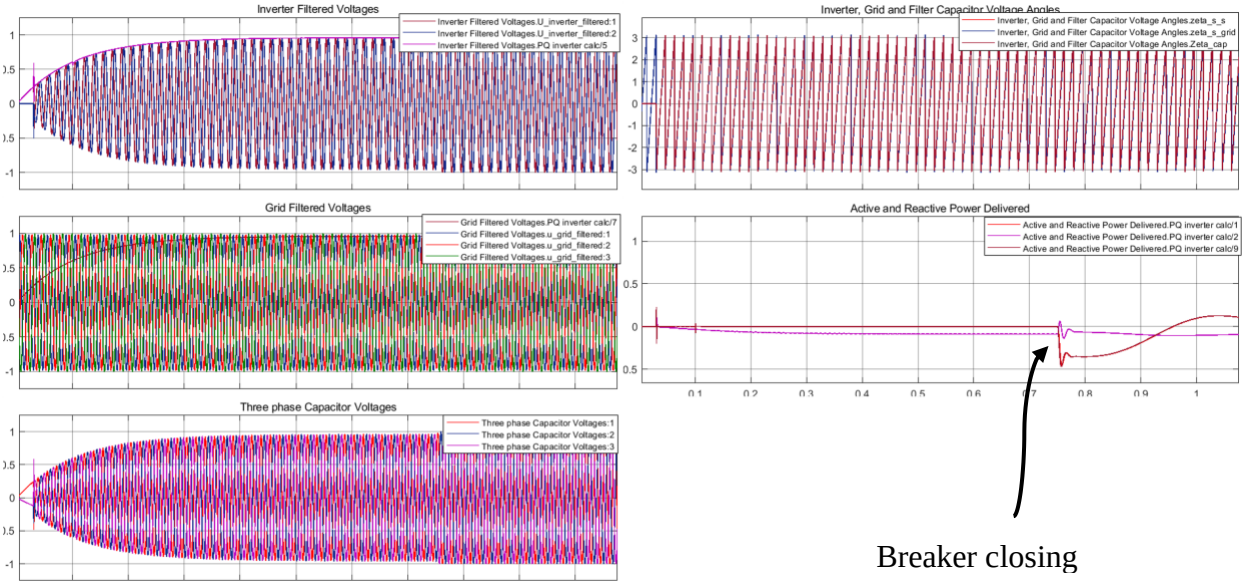

Figure 59: Voltage, Power and Phase measurements for Inverter, Grid and Capacitor during the breaker closing (d-q reference frame).

Figure 60, shows the angle error between the inverter and the grid PLL. The oscillations noticed in the error signal result from the characteristic of the phase information from the grid.

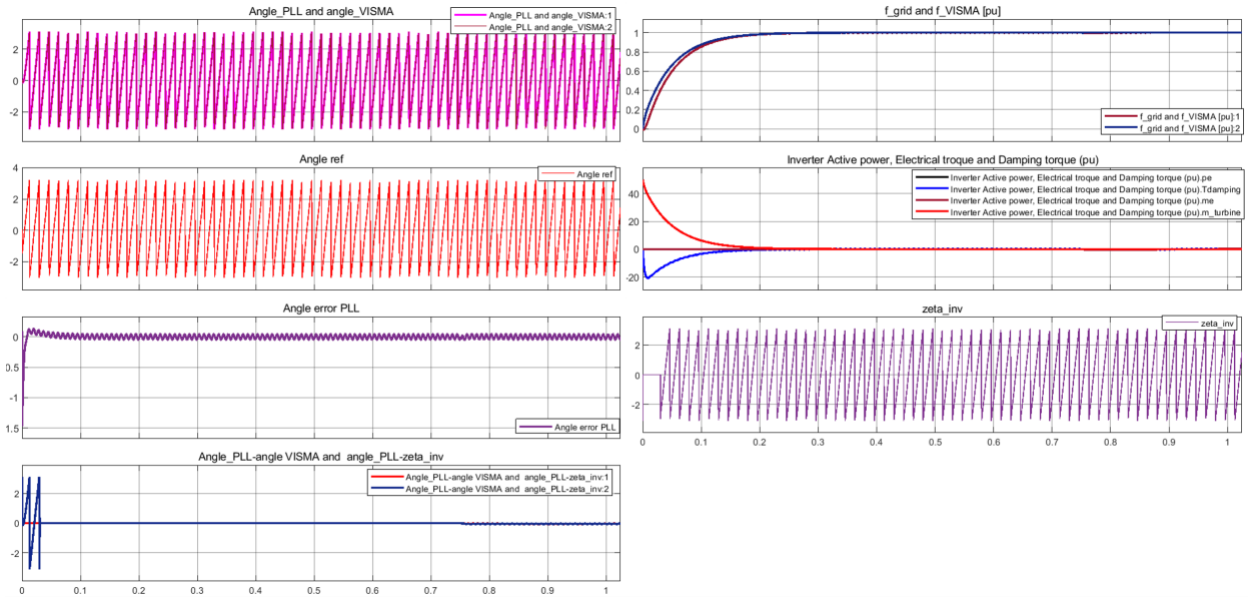

Figure 60: PLL and Visma Phase angle outputs before connecting the breaker and increasing the frequency set point (f_{sref}).

Figure 61 shows the signals generated from the filtered capacitor voltage amplitude and angle. Unlike the modelling of the capacitor voltage in alpha-beta reference frame, the d-q transformation of the filter capacitor produced quite a stable DC quantity in its amplitude. The angle of the capacitor has been varied from pi to pi. There are noticeable oscillations between 5-7 seconds, and this observation will be discussed in the subsequent section.

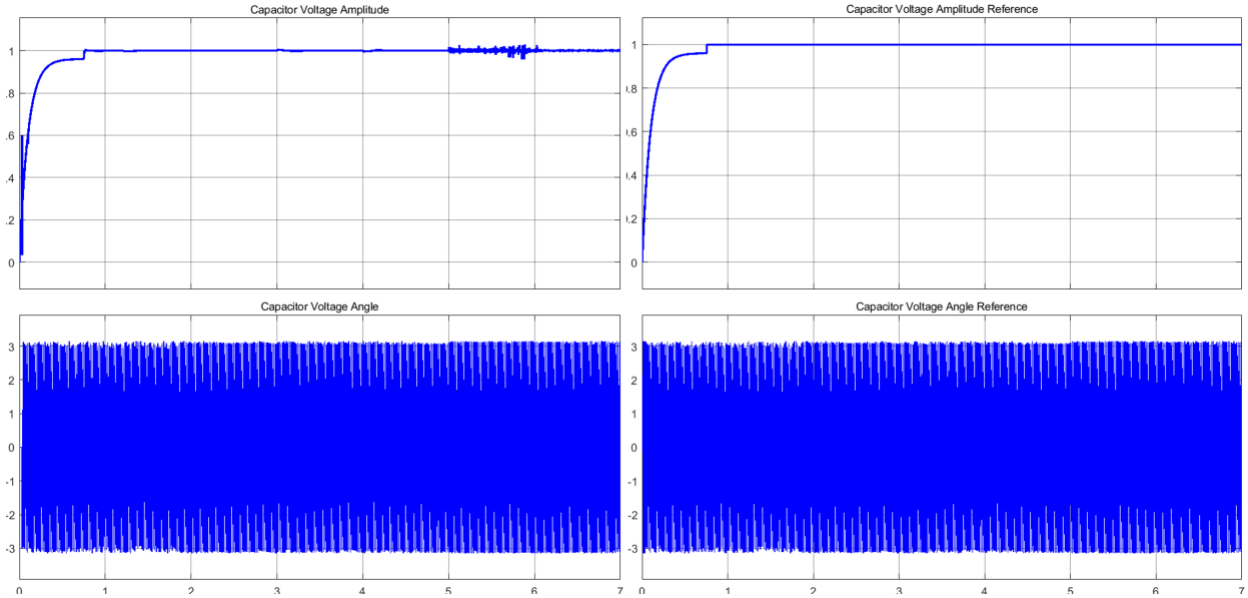

Figure 61: Actual and reference Capacitor Voltage amplitudes and angles for PI controllers (d-q reference frame).

6.2.2 Scenario 4: Grid connected (d-q)

After the closing of the circuit breaker, the inverter begins to deliver power to the grid at 1.2s based on the adjustments made to frequency set point (f_{sref}) of the Virtual synchronous machine. However, the oscillations observed before power delivery can be attributed to the system trying to meet the requirements of the breaker closing. At 1.8s a non-linear load was connected to the VSI (AFE) modelled in the d-q frame, resulting in an increase in power delivered to the grid and the load.

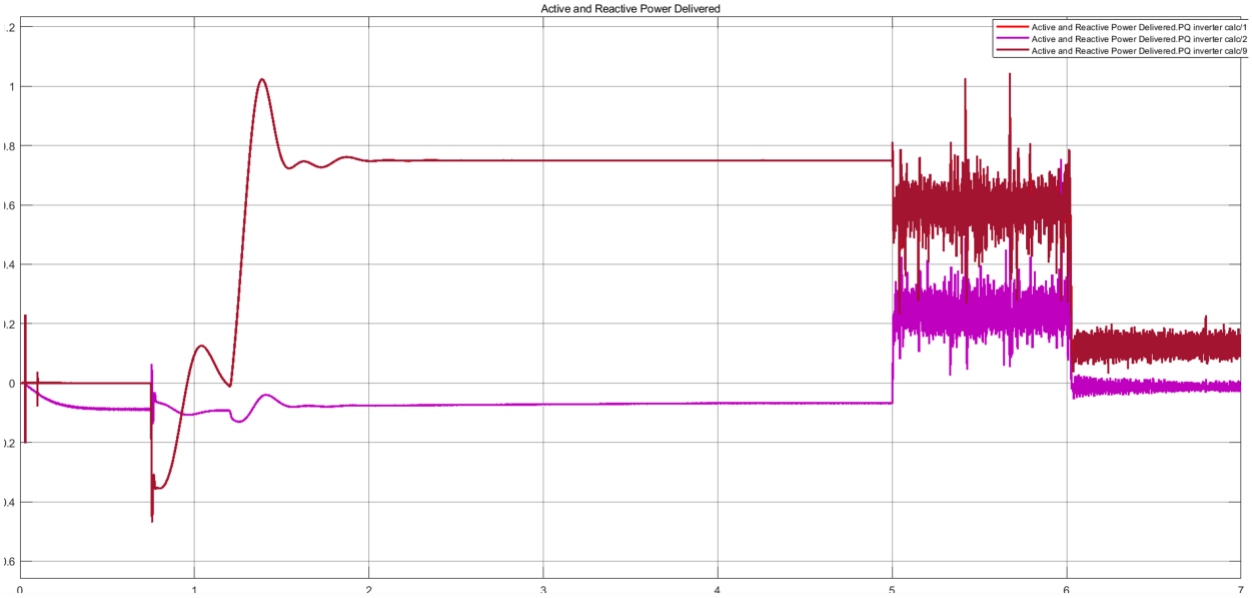

Figure 62: Active and Reactive Power outputs from the converter (d-q coordinate system).

6.2.3 Scenario 5: Island mode (d-q)

At 5s, the grid is disconnected from the system, as previously discussed in the alpha-beta transformation. The sudden disconnection of the grid affects the behavior of the capacitor voltage and the load. There exist oscillations for a duration of 2s. At 6s, the load reduces to 100kW from 800kW which reduces the oscillations.

Figure 63 shows the behavior of the damping torque in connection to the power being generated in the synchronous rotating reference frame (d-q). Limiting RoCoF was explicitly achieved by expressed tuning of the PI controllers that generated the I_{dref} and $I_{q\,ref}$ current references. It is observed that the damping term helped maintain the variation in frequency or power being generated in grid-connected and island modes. With the absence of the stiff grid, the speed or frequency VISMA matches the reference frequency.

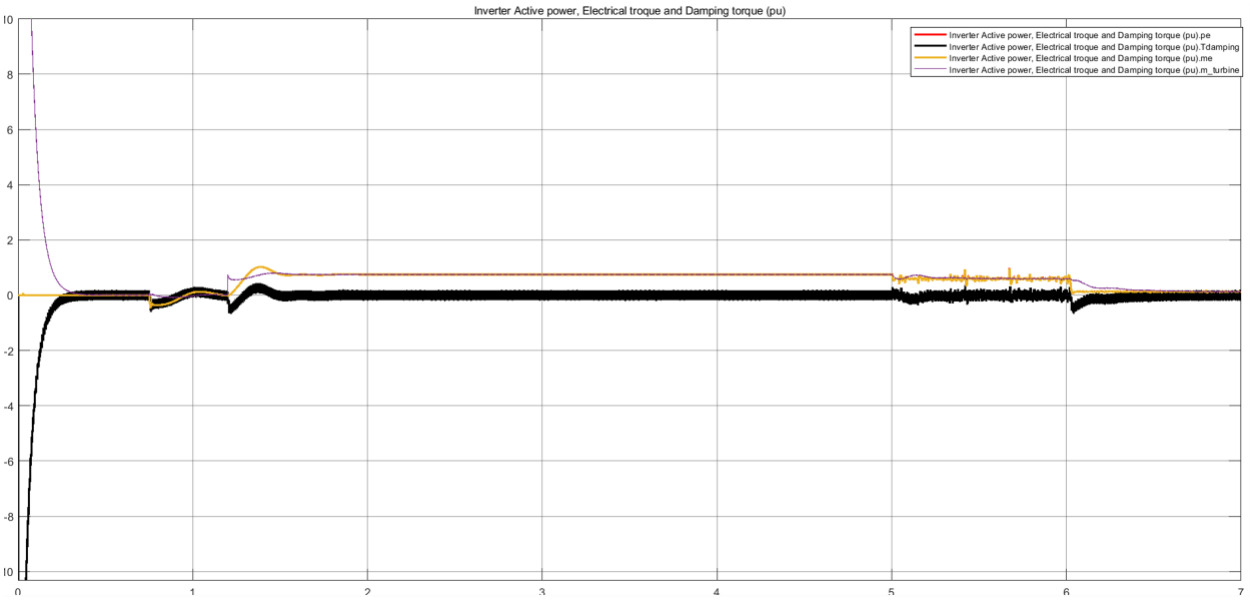

Figure 63: Electrical and damping torque responses of the VISMA in d-q reference frame.

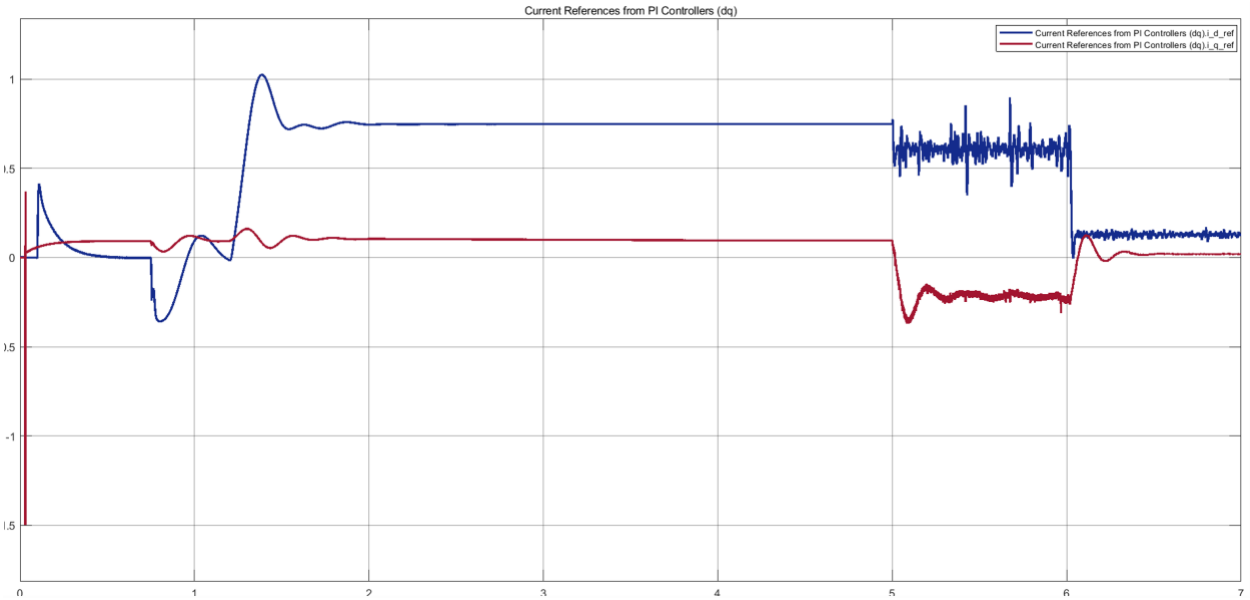

Figure 64: d-q current references from the PI controllers.

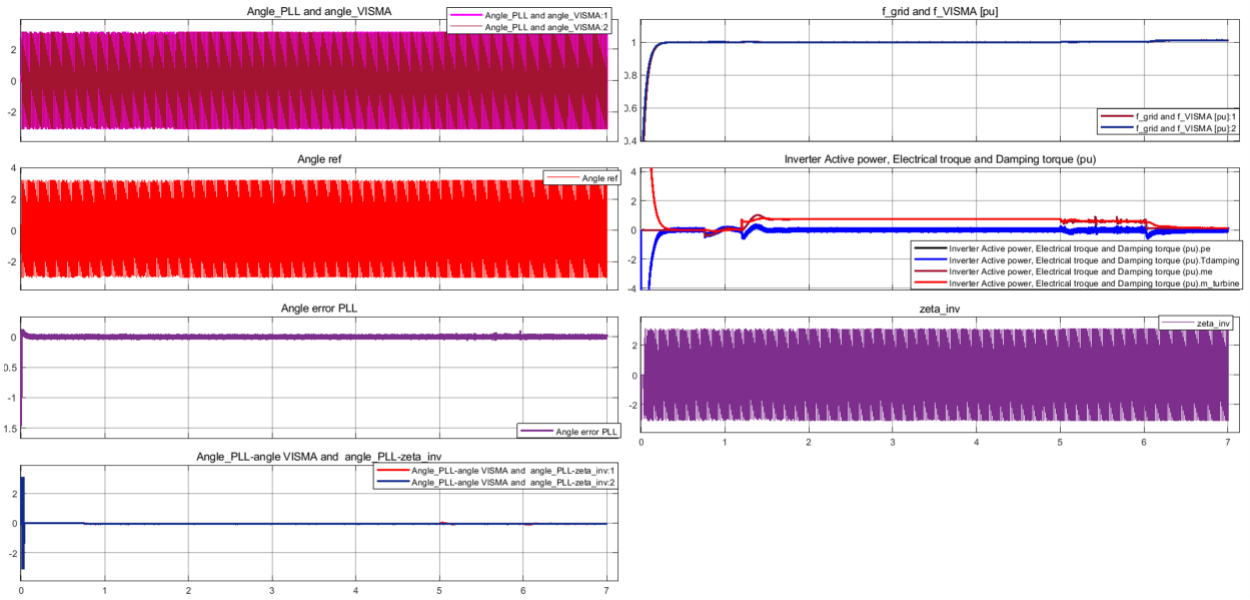

Figure 65: PLL and Visma Phase angle outputs in d-q reference frame (All Scenarios).

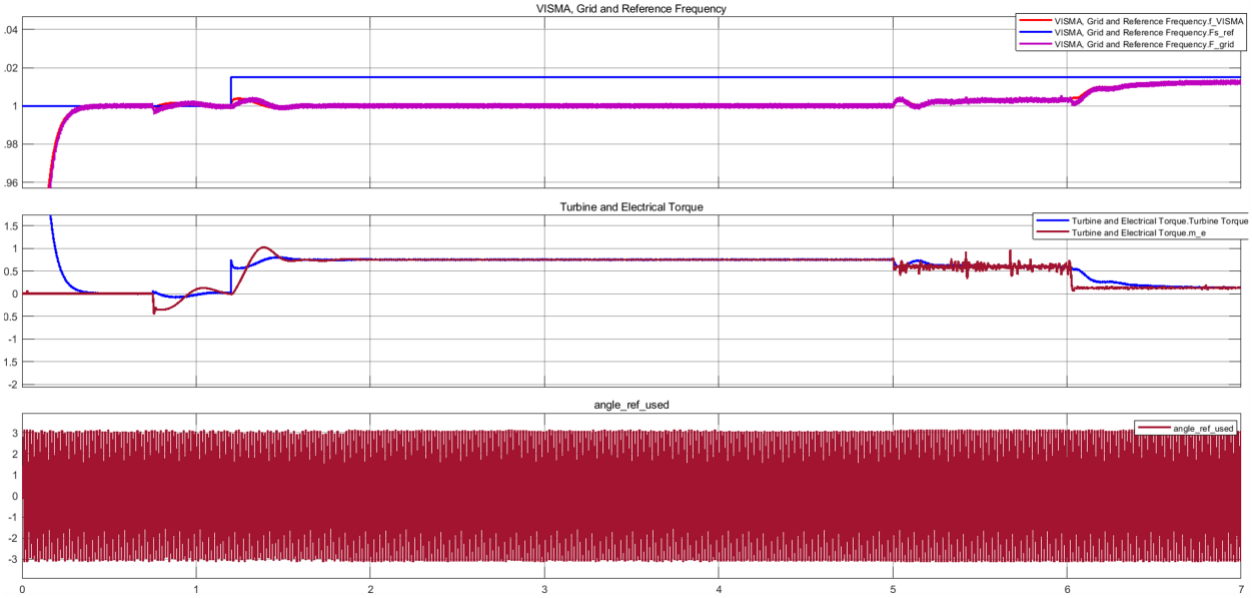

Figure 66: Frequency and angle responses of the VISMA (d-q) during power generation.

6.3.3 Scenario 6: Grid Frequency Variation (d-q)

In a similar approach to the stationary reference frame coordinates, the over/under frequency conditions were simulated in the polar coordinate (d-q) system. The frequency deviation of the system was achieved by $\pm 1\%$. The AFE´s response to the grid frequency variation are captured in Figure 67, Figure 68, Figure 69 and Figure 70.

At 3s, the increment of the grid frequency above its nominal value in polar coordinates gave a close response to the $\alpha\beta$ configuration. As expected, the machine accelerated with a

corresponding drop in generator torque when the frequency was increased from 60 to 60.5Hz. Likewise, the under-frequency condition gave an exact response with the $\alpha\beta$ model. However, it is important to properly model the damping torque of the virtual inertia emulation to ensure the VISMA in the VSI doesn't exceed the grid frequency set limit.

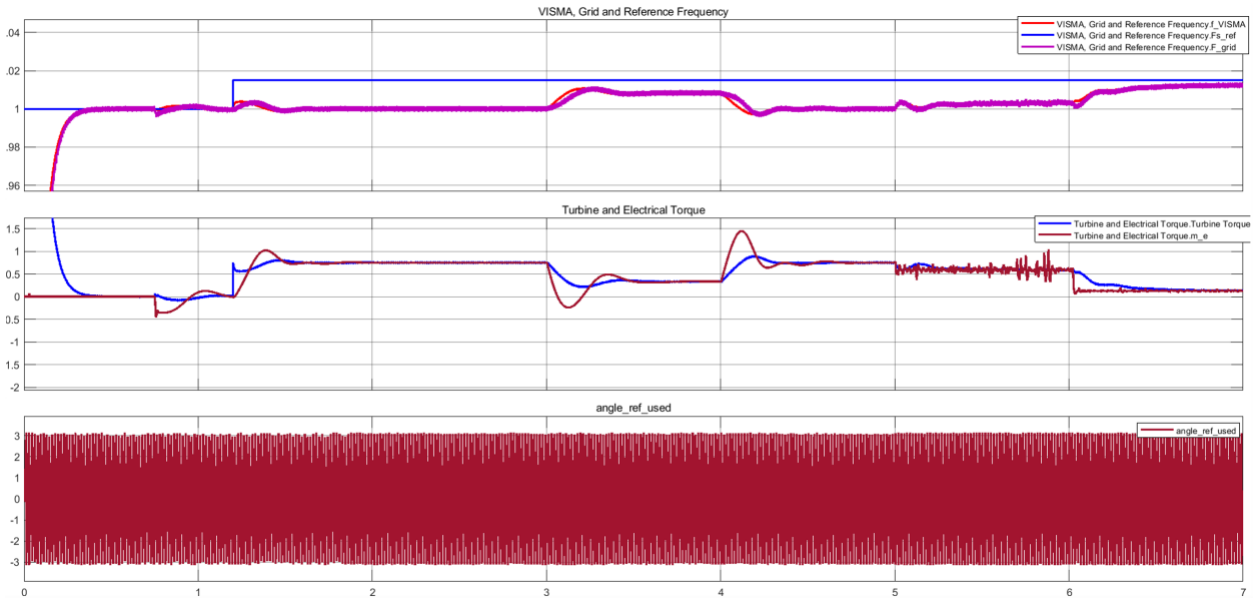

Figure 67: Performance of the VISMA during grid frequency deviation (over frequency).

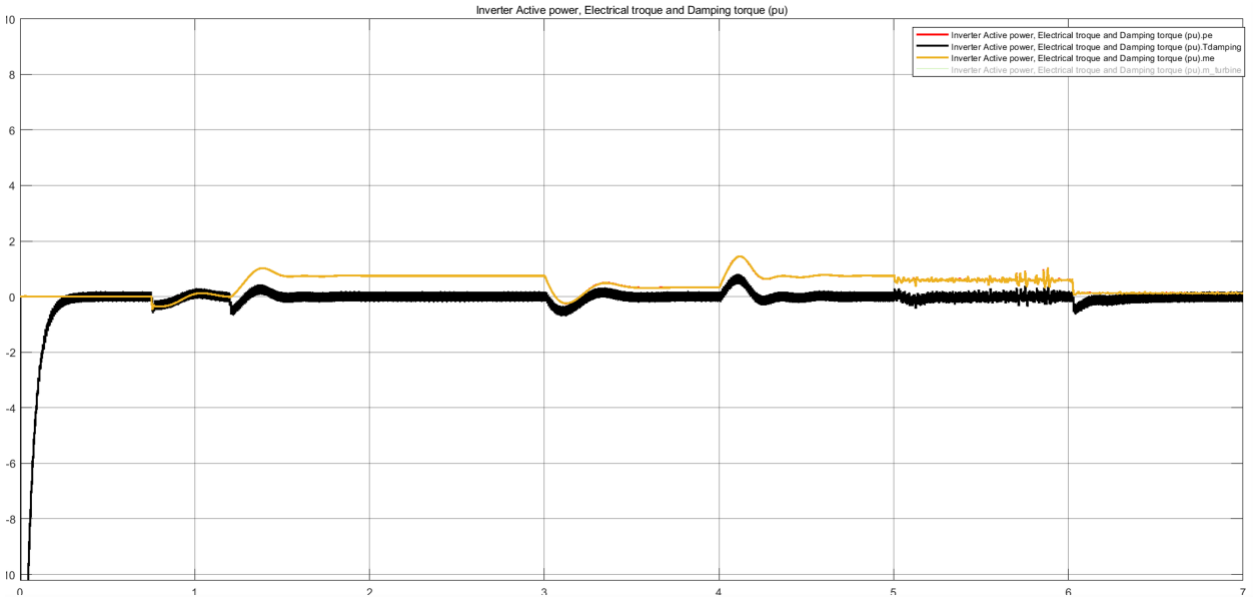

Figure 68: Inverter active power, Electrical and Damping torque of the VISMA (in d-q frame).

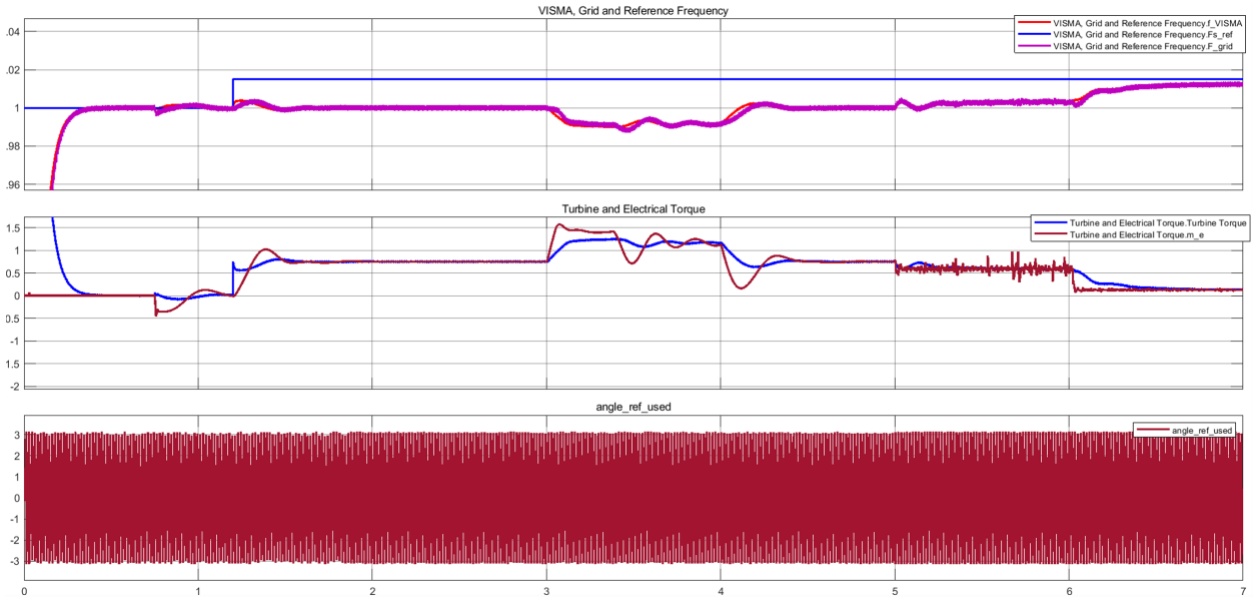

Figure 69: Performance of the VISMA during grid frequency deviation (under frequency).

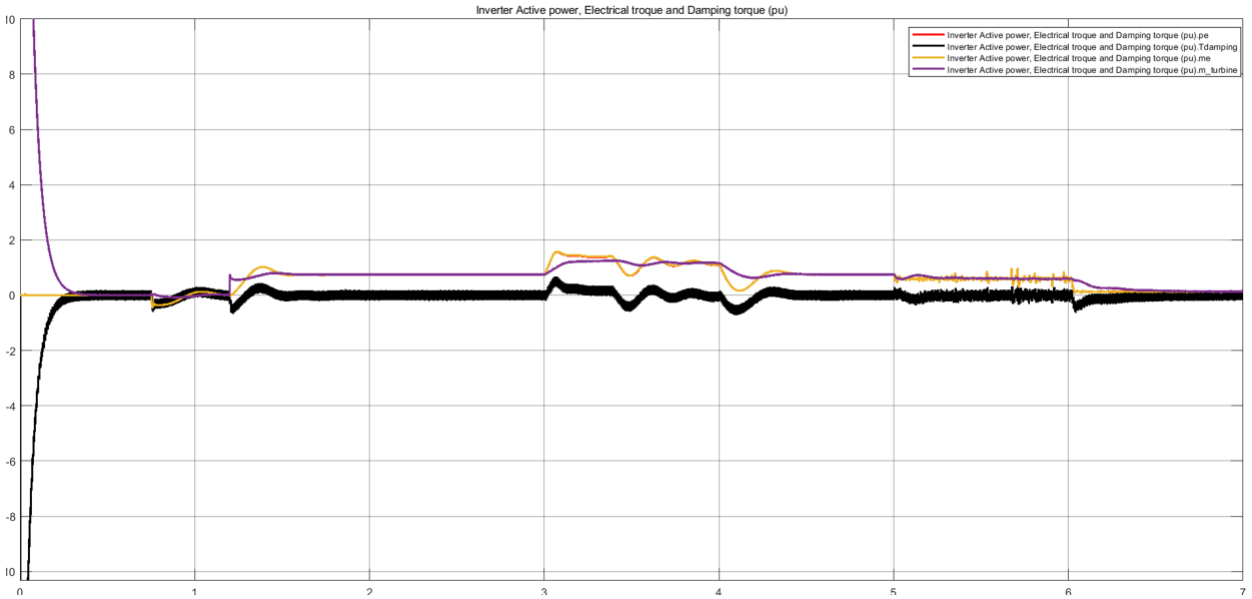

Figure 70: Inverter active power, Electrical and Damping torque of the VISMA (in d-q frame).

Chapter 7

7.0 Conclusions and Further work

7.1 Conclusions

- The engagement of the classical control theory and symmetrical optimum has been deployed in developing a strategy to tune PI controllers to achieve filter capacitor battery control in stator-orient coordinates (AC stationary quantities) and polar-orient coordinates (DC stationary quantities).
- The PI controllers in alpha-beta and d-q coordinates are efficient for good current reference tracking.
- The voltage amplitude and the angle of the filter capacitor are highly essential for maintaining active power balance between the converter and the grid.
- The proposed capacitor modelling in DC stationary quantities generated current references in polar coordinates that were used in maintaining the stability of the filter capacitor with or without any load or grid disturbance.
- Active damping is a popular methodology used in preventing oscillation and maintaining the stability of the reference currents generated for converter switching operations.
- The design of phase locked loop is instrumental for limiting the voltage, frequency, and phase errors between the converter and the grid.
- The stability of the virtual inertia control was analyzed for grid operation, frequency variations and islanding operations.
- With the absence of synchronous machines, the proposed virtual inertial emulation in the AFE is essential for maintaining inertia with rapid changes in grid frequency.
- The design of the virtual inertial control was robust enough to prevent the saturation of the current references.
- The proposed droop methodology for frequency control was useful in active power distribution.
- The proposed droop methodology for voltage regulation helped to achieve reactive power production.
- The frequency of the virtual inertia control had a good tracking of the grid frequency.
- The selection of beta β is essential for fast or slow response and damping of the controllers.
- K_p is the most significant element when tuning the amplitude and angle P+I controllers and its optimum value is dependent on the crossover frequency ω_c.
- K_I is less significant for systems stability, increasing its magnitude creates saturation and larger settling time
- The magnitude of droop gain was a determinant factor for the control of VISMA frequency deviation.
- The damping term in the system is modelled as a PI frequency controller. The proportional component in the damping winding is synonymous to the one present in

synchronous generators. The torque emulation in the VISMA is ascertained by the droop in the PI or speed controller. For a strong grid, the frequency or speed of the VISMA matches the network frequency. The turbine regulation determines the level of torque or power to be delivered.

- In an Island operation, the turbine regulator determines frequency.
- The control of unbalanced current or voltage was achieved with PI controllers in stator-orient and polar-orient coordinates. This control strategy was executed for the fundamental frequency.

7.2 Further Work

- The digital implementation of the virtual inertia control. A discrete model in d-q reference frame was partially implemented and the model was successfully synchronized with the grid. However, the VISMA model was implemented but wasn't fully functional. Concrete investigations couldn't be made due to time constraints.
- Investigate the approach on harmonic mitigation of current injected to the grid by the VSI with the presence of virtual inertia.
- Investigate other variables that can ensure frequency stability.
- Study the control loop characteristics and virtual inertial control behavior under grid fault conditions.
- Implement the control loop in a processor board either a DSP or FPGA.
- Testing operation in a laboratory to ascertain AFE operations in the grid connected and island conditions.
- Consider a test of the system holistically i.e. the combination of the AFE converter with adjustable speed drive and synchronous machine.

References

[1] U. Tamrakar, D. Shrestha, M. Maharjan, B. P. Bhattarai, T. M. Hansen, and R. Tonkoski, "Virtual inertia: Current trends and future directions," *Applied Sciences (Switzerland)*, vol. 7, no. 7. MDPI AG, Jun. 26, 2017. doi: 10.3390/app7070654.

[2] airswift.com, "Wind energy projects in europe," *https://www.airswift.com/blog/wind-energy-projects-norway*, Oct. 11, 2021.

[3] B. Kroposki *et al.*, "Achieving a 100% Renewable Grid: Operating Electric Power Systems with Extremely High Levels of Variable Renewable Energy," *IEEE Power and Energy Magazine*, vol. 15, no. 2, pp. 61–73, Mar. 2017, doi: 10.1109/MPE.2016.2637122.

[4] R. Yan, T. K. Saha, N. Modi, N. al Masood, and M. Mosadeghy, "The combined effects of high penetration of wind and PV on power system frequency response," *Applied Energy*, vol. 145, pp. 320–330, May 2015, doi: 10.1016/j.apenergy.2015.02.044.

[5] M. M. Hussein, T. Senjyu, M. Orabi, M. A. A. Wahab, and M. M. Hamada, "Control of a stand-alone variable speed wind energy supply system," *Applied Sciences (Switzerland)*, vol. 3, no. 2, pp. 437–456, Jun. 2013, doi: 10.3390/app3020437.

[6] J. Fang, H. Li, Y. Tang, and F. Blaabjerg, "Distributed Power System Virtual Inertia Implemented by Grid-Connected Power Converters," *IEEE Transactions on Power Electronics*, vol. 33, no. 10, pp. 8488–8499, Oct. 2018, doi: 10.1109/TPEL.2017.2785218.

[7] F. Blaabjerg, R. Teodorescu, M. Liserre, and A. v. Timbus, "Overview of control and grid synchronization for distributed power generation systems," *IEEE Transactions on Industrial Electronics*, vol. 53, no. 5. pp. 1398–1409, Oct. 2006. doi: 10.1109/TIE.2006.881997.

[8] J. Matevosyan *et al.*, "Proposed future Ancillary Services in Electric Reliability Council of Texas," Aug. 2015. doi: 10.1109/PTC.2015.7232743.

[9] A. Tosatto, M. Dijokas, T. Weckesser, S. Chatzivasileiadis, and R. Eriksson, "Sharing reserves through HVDC: Potential cost savings in the Nordic countries," *IET Generation, Transmission and Distribution*, vol. 15, no. 3, pp. 480–494, Feb. 2021, doi: 10.1049/gtd2.12035.

[10] K. Moslehi and R. Kumar, "A reliability perspective of the smart grid," *IEEE Transactions on Smart Grid*, vol. 1, no. 1, pp. 57–64, 2010, doi: 10.1109/TSG.2010.2046346.

[11] U. Tamrakar, D. Galipeau, R. Tonkoski, and I. Tamrakar, "Improving transient stability of photovoltaic-hydro microgrids using virtual synchronous machines," Aug. 2015. doi: 10.1109/PTC.2015.7232663.

[12] A. Gurung, D. Galipeau, R. Tonkoski, and I. Tamrakar, "Feasibility study of Photovoltaic-hydropower microgrids.," in *5th International Conference on Power and Energy Systems (ICPS)*, Oct. 2014, pp. 1–6.

[13] K. S. Ratnam, K. Palanisamy, and G. Yang, "Future low-inertia power systems: Requirements, issues, and solutions - A review," *Renewable and Sustainable Energy Reviews*, vol. 124. Elsevier Ltd, May 01, 2020. doi: 10.1016/j.rser.2020.109773.

[14] J. G. Slootweg and W. L. Kling, "Impacts of distributed generation on power system transient stability," in *Proceedings of the IEEE Power Engineering Society Transmission and Distribution Conference*, 2002, vol. 2, no. SUMMER, pp. 862–867. doi: 10.1109/pess.2002.1043465.

[15] J. Driesen and K. Visscher, "Virtual synchronous generators," in *2008 IEEE Power and Energy Society General Meeting - Conversion and Delivery of Electrical Energy in the 21st Century*, Jul. 2008, pp. 1–3. doi: 10.1109/PES.2008.4596800.
[16] T. K. Fathin, S. Rahman, M. Watanabe, and Y. Mitani, "Power Systems Virtual Inertia Synthesis and Control." [Online]. Available: http://www.springer.com/series/4622
[17] H. Bevrani, T. Ise, and Y. Miura, "Virtual synchronous generators: A survey and new perspectives," *International Journal of Electrical Power & Energy Systems*, vol. 54, pp. 244–254, Jan. 2014, doi: 10.1016/j.ijepes.2013.07.009.
[18] S. D'Arco, J. A. Suul, and O. B. Fosso, "A Virtual Synchronous Machine implementation for distributed control of power converters in SmartGrids," *Electric Power Systems Research*, vol. 122, pp. 180–197, 2015, doi: 10.1016/j.epsr.2015.01.001.
[19] M. C. Chandorkar, D. M. Divan, and R. Adapa, "Control of parallel connected inverters in standalone ac supply systems," *IEEE Transactions on Industry Applications*, vol. 29, no. 1, pp. 136–143, 1993, doi: 10.1109/28.195899.
[20] S. D'Arco and J. A. Suul, "Virtual synchronous machines - Classification of implementations and analysis of equivalence to droop controllers for microgrids," 2013. doi: 10.1109/PTC.2013.6652456.
[21] D.-I. Hans-Peter Beck and D.-I. Ralf Hesse, "Virtual Synchronous Machine."
[22] C. Pelczar, "Mobile Virtual Synchronous Machine for Vehicle-to-Grid Applications," TU Clausthal, Gottingen, 2012. [Online]. Available: https://cuvillier.de
[23] Y. Chen, R. Hesse, D. Turschner, and H. P. Beck, "Comparison of methods for implementing virtual synchronous machine on inverters," *Renewable Energy and Power Quality Journal*, vol. 1, no. 10, pp. 734–739, Apr. 2012, doi: 10.24084/repqj10.453.
[24] Q.-C. Zhong and T. Hornik, *Control of Power Inverters in Renewable Energy and Smart Grid Integration*. Chichester, West Sussex, United Kingdom: John Wiley & Sons, Ltd., 2012. doi: 10.1002/9781118481806.
[25] N. Pogaku, M. Prodanović, and T. C. Green, "Modeling, analysis and testing of autonomous operation of an inverter-based microgrid," *IEEE Transactions on Power Electronics*, vol. 22, no. 2, pp. 613–625, Mar. 2007, doi: 10.1109/TPEL.2006.890003.
[26] J. M. Guerrero, L. G. de Vicuna, J. Matas, M. Castilla, and J. Miret, "A wireless controller to enhance dynamic performance of parallel inverters in distributed generation systems," *IEEE Transactions on Power Electronics*, vol. 19, no. 5, pp. 1205–1213, Sep. 2004, doi: 10.1109/TPEL.2004.833451.
[27] A. R. Bergen, *Power Systems Analysis*, 2nd ed. New Jersey: Tom Robbins, 1986.
[28] A. Tuladha and ; H Jin, "Parallel Operation of Single Phase Inverter Modules With No Control Interconnections."
[29] R. Nilsen, "Electric Drives," Course TET4120, Norwegian University of Science and Technology, NTNU, Trondheim, 2018.
[30] S. J. Chapman, "ELECTRIC MACHINERY FUNDAMENTALS FIFTH EDITION."
[31] P. Krause, O. Wasynczuk, S. Sudhoff, and S. Pekarek, Eds., *Analysis of Electric Machinery and Drive Systems*. Hoboken, NJ, USA: John Wiley & Sons, Inc., 2013. doi: 10.1002/9781118524336.
[32] R. Tiwari and R. Nilsen, "Active Compensation of Unbalanced Load Currents in Grid Connected Voltage Source Converters; Active Compensation of Unbalanced Load Currents in Grid Connected Voltage Source Converters," 2019.

[33] D. Baimel, J. Belikov, J. M. Guerrero, and Y. Levron, "Dynamic Modeling of Networks, Microgrids, and Renewable Sources in the dq0 Reference Frame: A Survey," *IEEE Access*, vol. 5, pp. 21323–21335, Oct. 2017, doi: 10.1109/ACCESS.2017.2758523.
[34] N. Kroutikova, C. A. Hernandez-Aramburo, and T. C. Green, "State-space model of grid-connected inverters under current control mode," *IET Electric Power Applications*, vol. 1, no. 3, pp. 329–338, 2007, doi: 10.1049/iet-epa:20060276.
[35] P. Mattavelli, "A closed-loop selective harmonic compensation for active filters," *IEEE Transactions on Industry Applications*, vol. 37, no. 1, pp. 81–89, Jan. 2001, doi: 10.1109/28.903130.
[36] C. J. O'rourke, "Decentralized Power Systems: Reference-Frame Theory and Stability Region Generation," 2013.
[37] S. Chattopadhyay, M. Mitra, and S. Sengupta, "Electric Power Quality," *Power Systems*, vol. 62, 2011, doi: 10.1007/978-94-007-0635-4.
[38] P. Kundur, *Power System Stability and Control*. 2007.
[39] A. E. Fitzgerald, C. Kingsley, and S. D. Umans, *Electric Machinery*, 6th ed. McGraw-Hill, 2003.
[40] H. Akagi, E. H. Watanabe, and M. Aredes, *Instantaneous Power Theory and Applications to Power Conditioning*, Second. Jhon Wiley & Sons, 2017.
[41] S. Kharjule, "Voltage source inverter," in *International Conference on Energy Systems and Applications, ICESA 2015*, Jul. 2016, pp. 537–542. doi: 10.1109/ICESA.2015.7503407.
[42] O. Anaya-Lara, | David, C.-G. E. Moreno-Goytia, and G. Adam, "Control, Protection, and Integration to Electrical Systems Offshore Wind Energy Generation."
[43] I. Colak, E. Kabalci, and R. Bayindir, "Review of multilevel voltage source inverter topologies and control schemes," *Energy Conversion and Management*, vol. 52, no. 2, pp. 1114–1128, 2011, doi: 10.1016/j.enconman.2010.09.006.
[44] B. Wu and M. Narimani, *High-Power Converters and AC Drives*. Hoboken, NJ, USA: John Wiley & Sons, Inc., 2017. doi: 10.1002/9781119156079.
[45] D. G. Holmes and T. A. Lipo, *Pulse Width Modulation for Power Converters: Principles and Practice*, vol. 18. Wiley-IEEE Press, 2003.
[46] R. Adapa, "High-wire act: HVdc technology: The state of the art," *IEEE Power and Energy Magazine*, vol. 10, no. 6, pp. 18–29, 2012, doi: 10.1109/MPE.2012.2213011.
[47] J. K. Singh and R. K. Behera, "Hysteresis Current Controllers for Grid Connected Inverter: Review and Experimental Implementation," Jul. 2018. doi: 10.1109/PEDES.2018.8707755.
[48] H. Vahedi, A. Sheikholeslami, M. Tavakoli Bina, and M. Vahedi, "Review and simulation of fixed and adaptive hysteresis current control considering switching losses and high-frequency harmonics," *Advances in Power Electronics*, vol. 2011. 2011. doi: 10.1155/2011/397872.
[49] L. Jun and W. Dazhi, "Study and Simulation of a Novel Hysteresis Current Control Strategy," in *2009 Second International Conference on Intelligent Computation Technology and Automation*, 2009, pp. 306–309. doi: 10.1109/ICICTA.2009.924.
[50] M. Kale and E. Ozdemir, "An adaptive hysteresis band current controller for shunt active power filter," *Electric Power Systems Research*, vol. 73, no. 2, pp. 113–119, Feb. 2005, doi: 10.1016/j.epsr.2004.06.006.

[51] G. Anu and F. M. Fernandez, "Identification of Harmonic Injection and Distortion Power at Customer Location," in *2020 19th International Conference on Harmonics and Quality of Power (ICHQP)*, Jul. 2020, pp. 1–5. doi: 10.1109/ICHQP46026.2020.9177869.

[52] R. Teodorescu, M. Liserre, and P. Rodríguez, *Grid Converters for Photovoltaic and Wind Power Systems*. Wiley, 2011. doi: 10.1002/9780470667057.

[53] K. B. Park, F. D. Kieferndorf, U. Drofenik, S. Pettersson, and F. Canales, "Weight Minimization of LCL Filters for High-Power Converters: Impact of PWM Method on Power Loss and Power Density," *IEEE Transactions on Industry Applications*, vol. 53, no. 3, pp. 2282–2296, May 2017, doi: 10.1109/TIA.2017.2657479.

[54] X. Ruan, X. Wang Donghua Pan, D. Yang Weiwei Li, and C. Bao, "CPSS Power Electronics Series Control Techniques for LCL-Type Grid-Connected Inverters." [Online]. Available: http://www.springer.com/series/15422

[55] R. Pena-Alzola, M. Liserre, F. Blaabjerg, R. Sebastian, J. Dannehl, and F. W. Fuchs, "Systematic design of the lead-lag network method for active damping in lcl-filter based three phase converterss," *IEEE Transactions on Industrial Informatics*, vol. 10, no. 1, pp. 43–52, 2014, doi: 10.1109/TII.2013.2263506.

[56] M. Liserre, F. Blaabjerg, and A. Dell'aquila, "Step-by-step design procedure for a grid-connected three-phase PWM voltage source converter," *International Journal of Electronics*, vol. 91, no. 8, pp. 445–460, Aug. 2004, doi: 10.1080/00207210412331306186.

[57] X. Wang, L. Harnefors, and F. Blaabjerg, "Unified Impedance Model of Grid-Connected Voltage-Source Converters," *IEEE Transactions on Power Electronics*, vol. 33, no. 2, pp. 1775–1787, Feb. 2018, doi: 10.1109/TPEL.2017.2684906.

[58] S. London Berlin, H. New, Y. Barcelona, H. Kong, and M. Paris, "Advances in Industrial Control."

[59] E. Twining and D. G. Holmes, "Grid current regulation of a three-phase voltage source inverter with an LCL input filter," *IEEE Transactions on Power Electronics*, vol. 18, no. 3, pp. 888–895, May 2003, doi: 10.1109/TPEL.2003.810838.

[60] A. Timbus, M. Liserre, R. Teodorescu, P. Rodriguez, and F. Blaabjerg, "Evaluation of current controllers for distributed power generation systems," *IEEE Transactions on Power Electronics*, vol. 24, no. 3, pp. 654–664, 2009, doi: 10.1109/TPEL.2009.2012527.

[61] R. Teodorescu, F. Blaabjerg, M. Liserre, and P. C. Loh, "Proportional-resonant controllers and filters for grid-connected voltage-source converters," *IEE Proceedings: Electric Power Applications*, vol. 153, no. 5, pp. 750–762, 2006, doi: 10.1049/ip-epa:20060008.

[62] V. Blasko and V. Kaura, "Novel control to actively damp resonance in input LC filter of a three phase voltage source converter," in *Conference Proceedings - IEEE Applied Power Electronics Conference and Exposition - APEC*, 1996, vol. 2, pp. 545–551. doi: 10.1109/apec.1996.500495.

[63] J. Xu, S. Xie, and T. Tang, "Active damping-based control for grid-connected LCL - filtered inverter with injected grid current feedback only," *IEEE Transactions on Industrial Electronics*, vol. 61, no. 9, pp. 4746–4758, 2014, doi: 10.1109/TIE.2013.2290771.

[64] V. Kaura and V. Blasko, "Operation of a phase locked loop system under distorted utility conditions," *IEEE Transactions on Industry Applications*, vol. 33, no. 1, pp. 58–63, 1997, doi: 10.1109/28.567077.

[65] P. A. Dahono, "A control method to damp oscillation in the input LC filter," in *2002 IEEE 33rd Annual IEEE Power Electronics Specialists Conference. Proceedings (Cat. No.02CH37289)*, vol. 4, pp. 1630–1635. doi: 10.1109/PSEC.2002.1023044.

[66] O. Mo, M. Hernes, and K. Ljokelsoy, "Active damping of oscillations in LC-filter for line connected, current controlled, PWM voltage source converters," 2003. Accessed: Jun. 13, 2022. [Online]. Available: https://www.sintef.no/globalassets/project/powerelectronics/epe_cd_0032.pdf

[67] M. Bahrman and B. Johnson, "The ABCs of HVDC transmission technologies," *IEEE Power and Energy Magazine*, vol. 5, no. 2, pp. 32–44, Mar. 2007, doi: 10.1109/MPAE.2007.329194.

[68] R. Nilsen and K. Uhlen, "Integration of new energy sources and components with converters as interfaces to the power grid," Course ET6203, Norwegian University of Science and Technology , Trondheim.

[69] D. Woldegiorgis, Y. Wei, H. Mhiesan, and A. Mantooth, "A New Dc-link Capacitor Voltage Balancing Method for Three-level SVM Strategies Based on Two-level Space Vector Diagram," in *2020 IEEE 9th International Power Electronics and Motion Control Conference, IPEMC 2020 ECCE Asia*, Nov. 2020, pp. 1746–1751. doi: 10.1109/IPEMC-ECCEAsia48364.2020.9367733.

[70] JosepM. Guerrero, "Connecting renewable energy sources into the smartgrid," in *2011 IEEE International Symposium on Industrial Electronics*, Jun. 2011, pp. 2400–2566. doi: 10.1109/ISIE.2011.5984420.

Appendix Matlab code for PI controllers

```
%Tuning of PI Controller for AFE
clc
f=60
fsw=15000
c=800*10^(-6)
Vdc0=(2*(sqrt(2))/sqrt(3))*690
Vdc=1030

% Calculation of TRI OF PWM
Ttri=1/fsw

%Tdelay=Ttri/6

Tfilter=c
Ks= (1.5*(Vdc/Vdc0))

% Calculation of Tequivqlent (Teq)
Teq=100*10^-6

B= [4 5 6 7 8 9 10]

%Integral Time constant for AFE
Ti=((B).*Teq)

% Proportional Gain for AFE
Kp= (Tfilter./(B.*(Teq*Ks)))
```

Simulink circuit connections in Alpha beta coordinate system

The power circuits

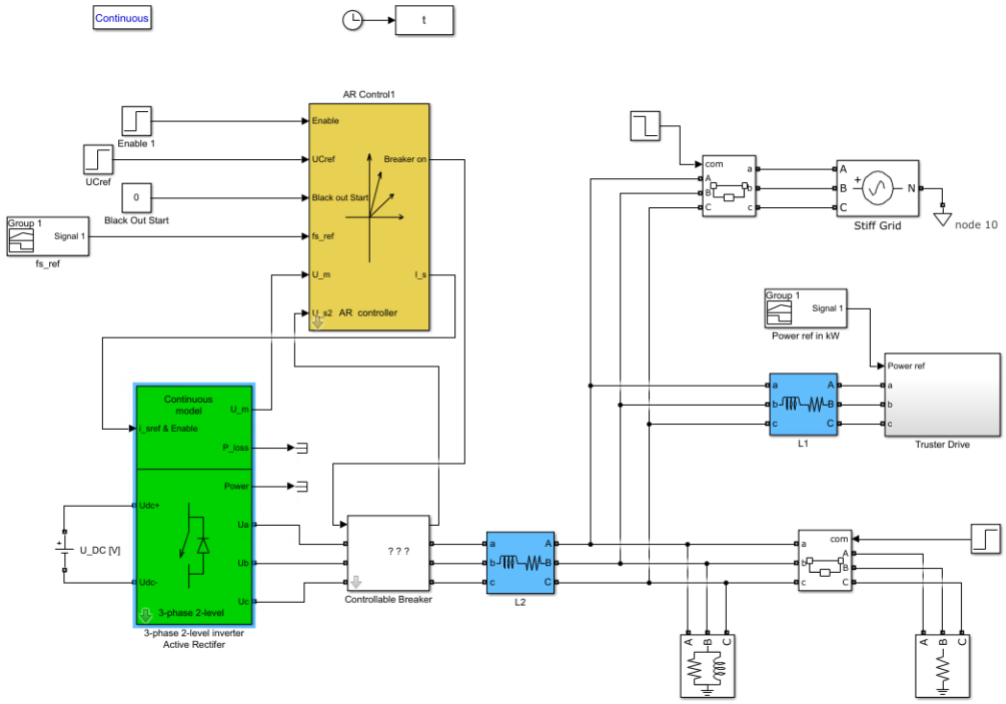

Per unit calculations

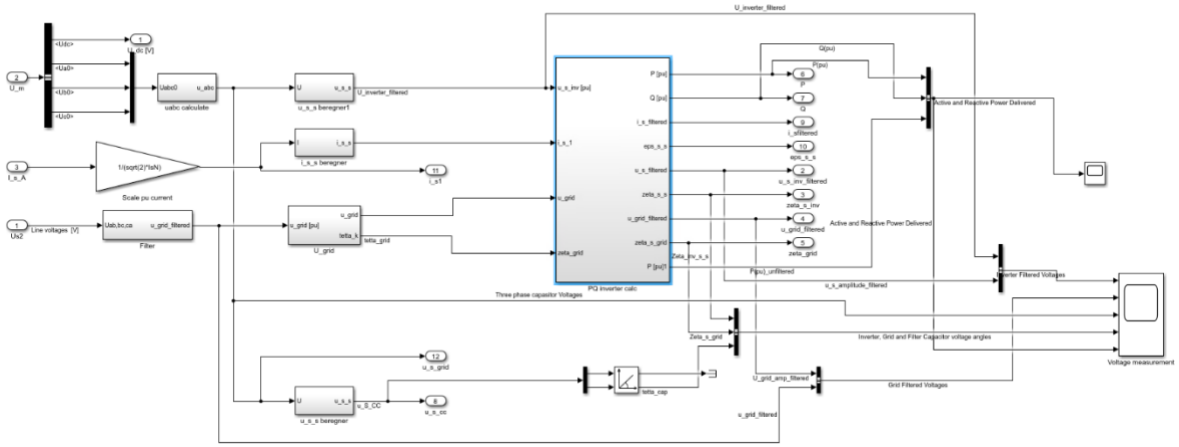

Inverter PQ calculation

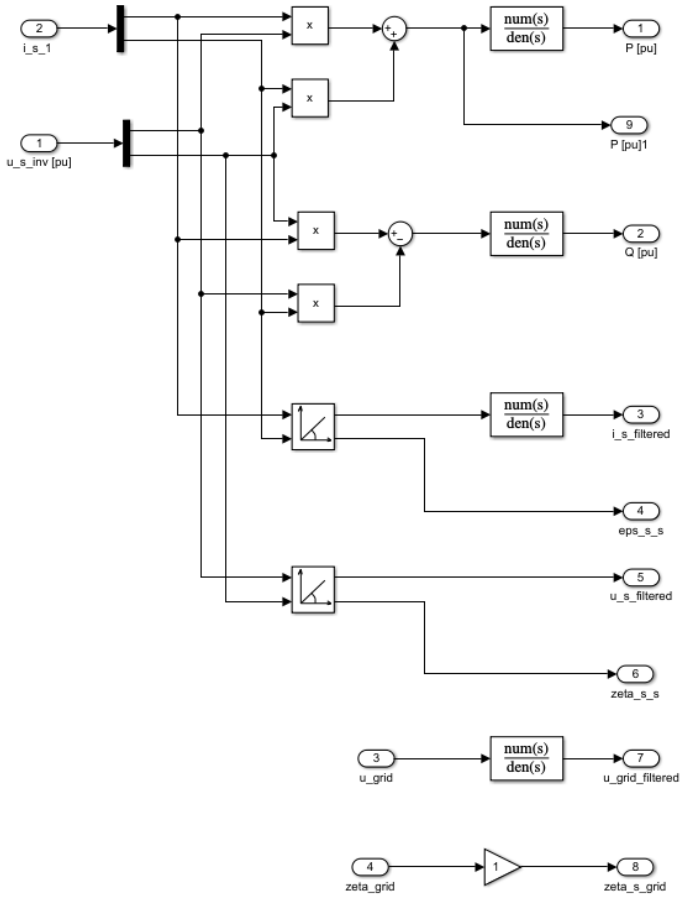

Inner current control loop

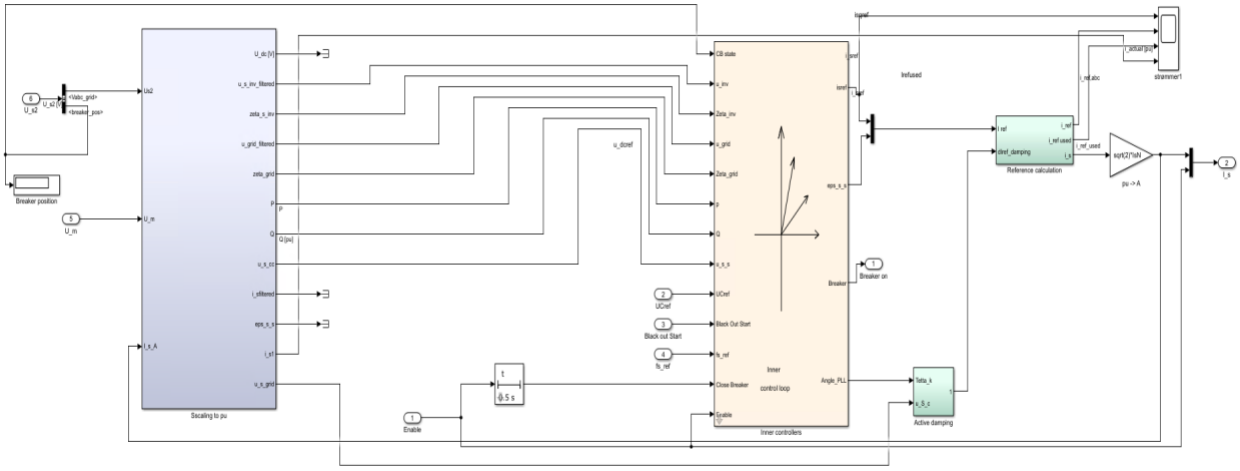

Active damping

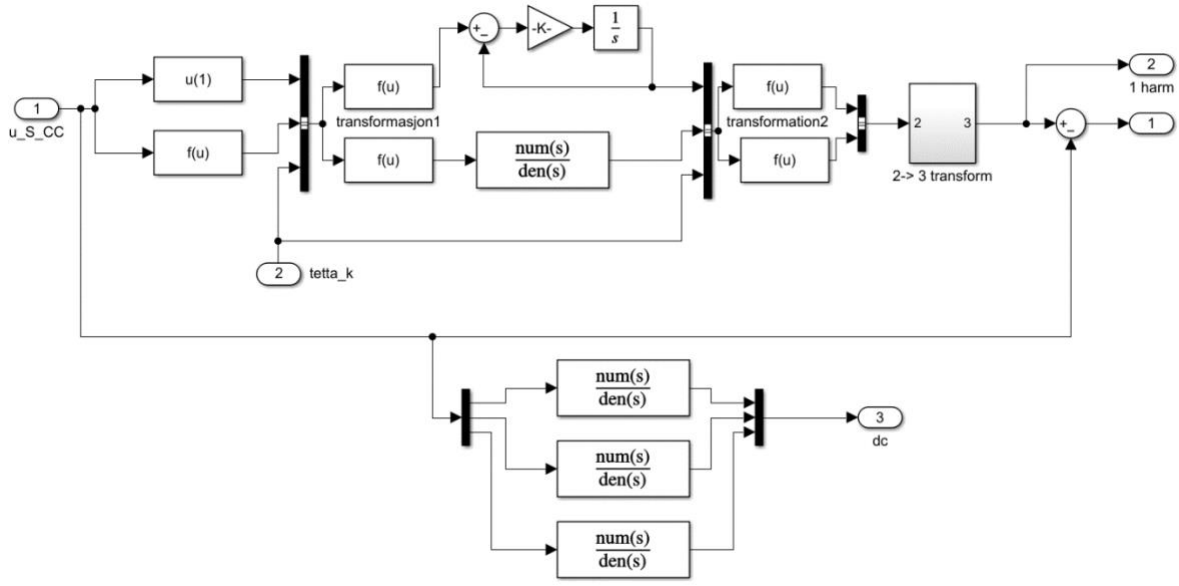

Current references for gate signals

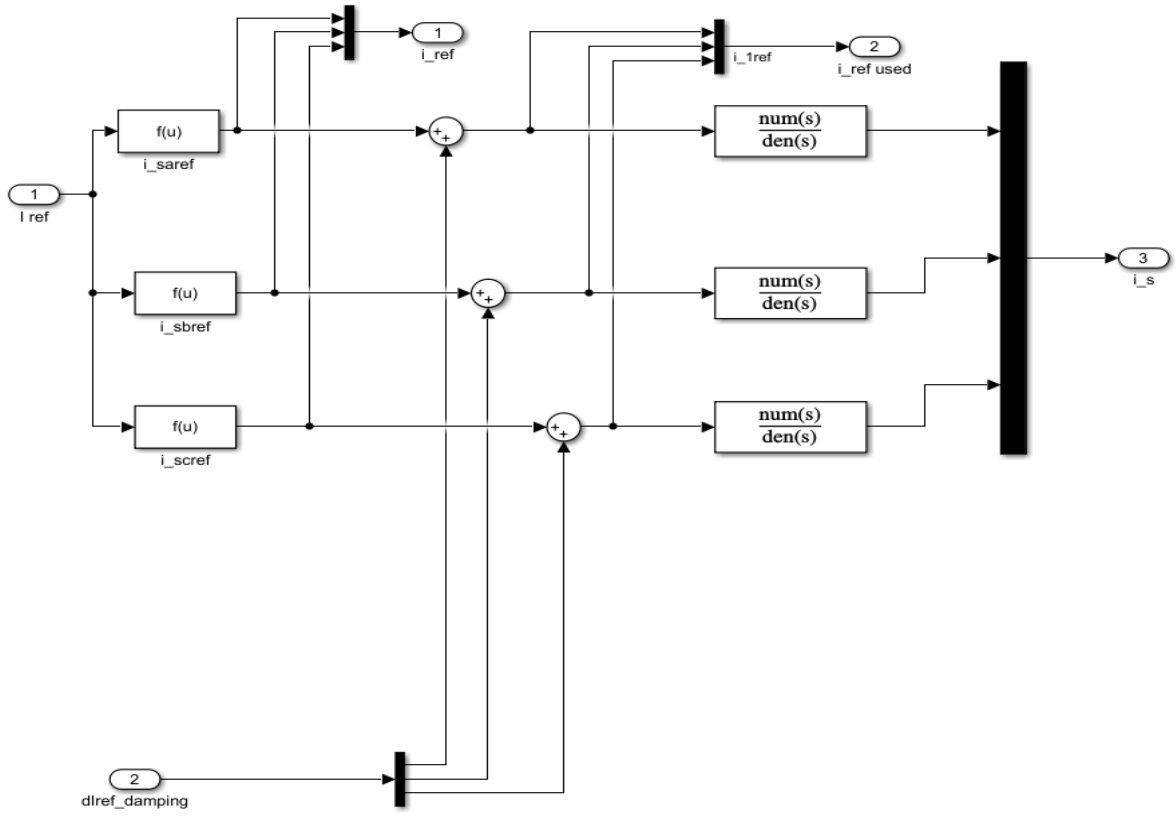

Truster drive load model

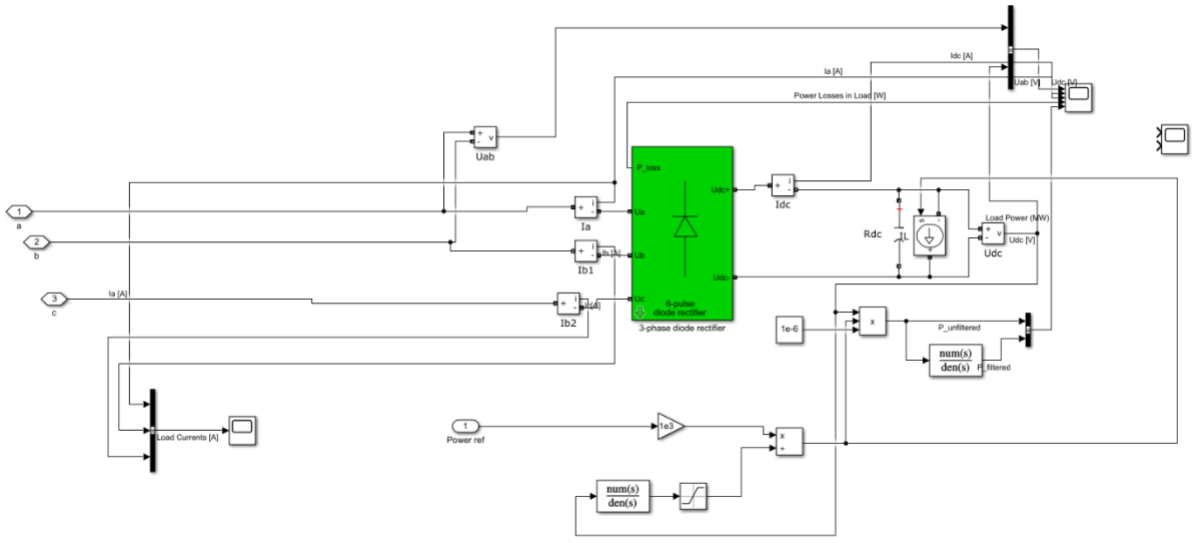

Outer voltage control loop

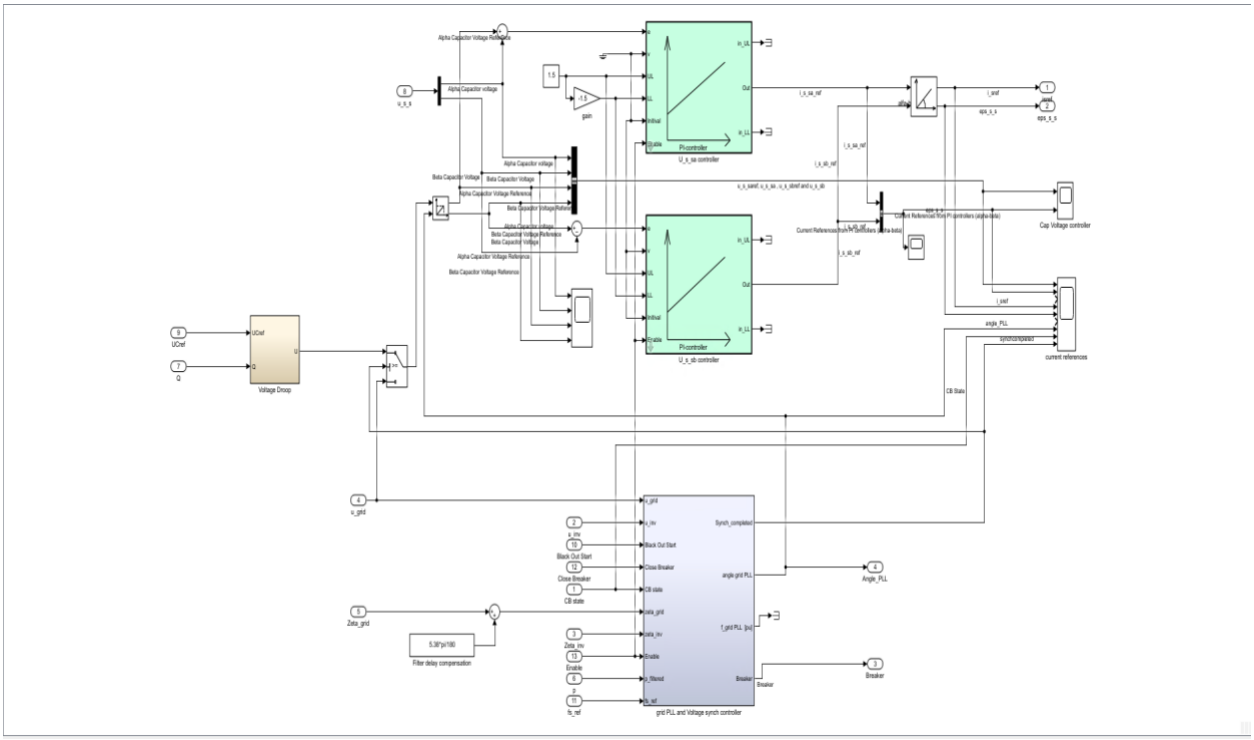

VISMA and Grid PLL synchronization

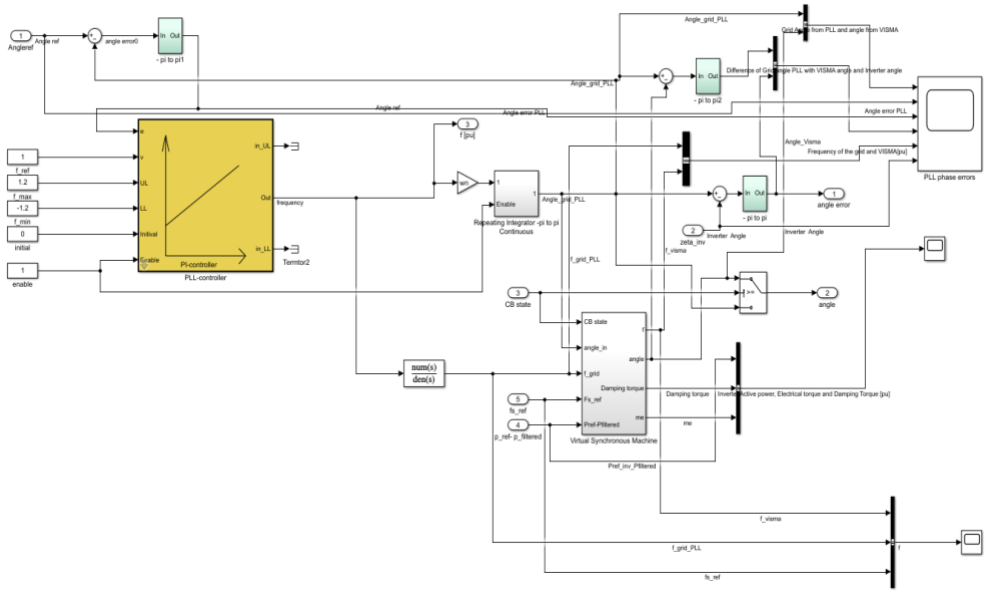

VISMA Model

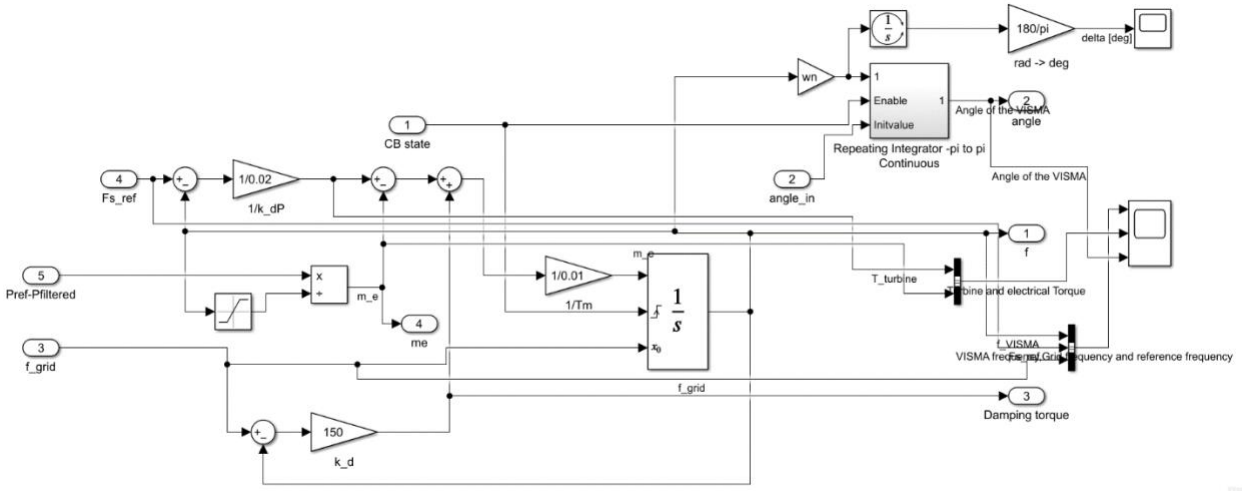

Simulink circuit connections in d-q coordinate system

All the connection are same except the outer voltage control loop with alpha beta coordinate system.

Inner current control loop

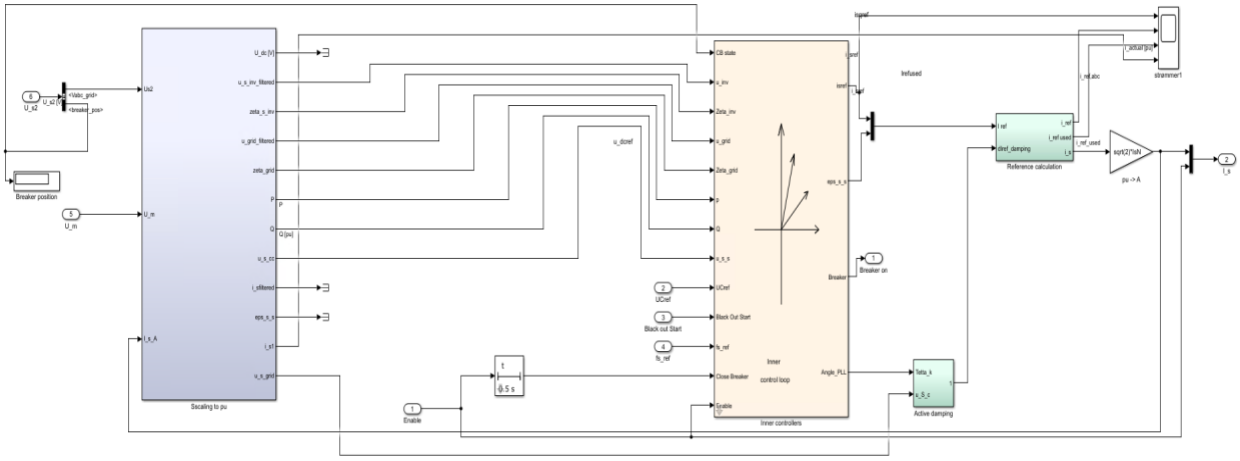

Outer voltage control loop

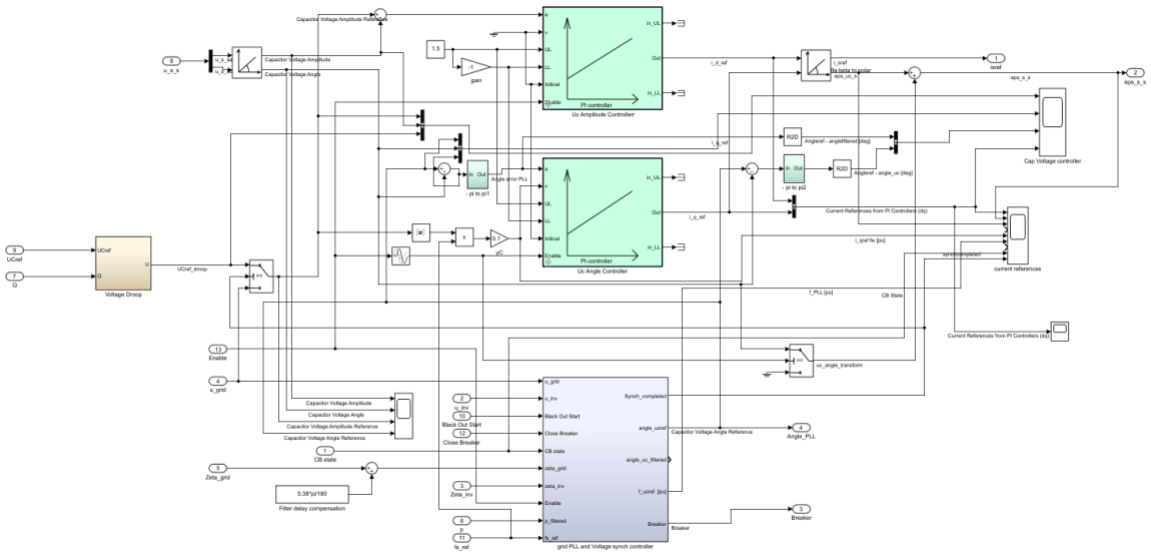

Simulink circuit connections for discrete model in d-q coordinate system

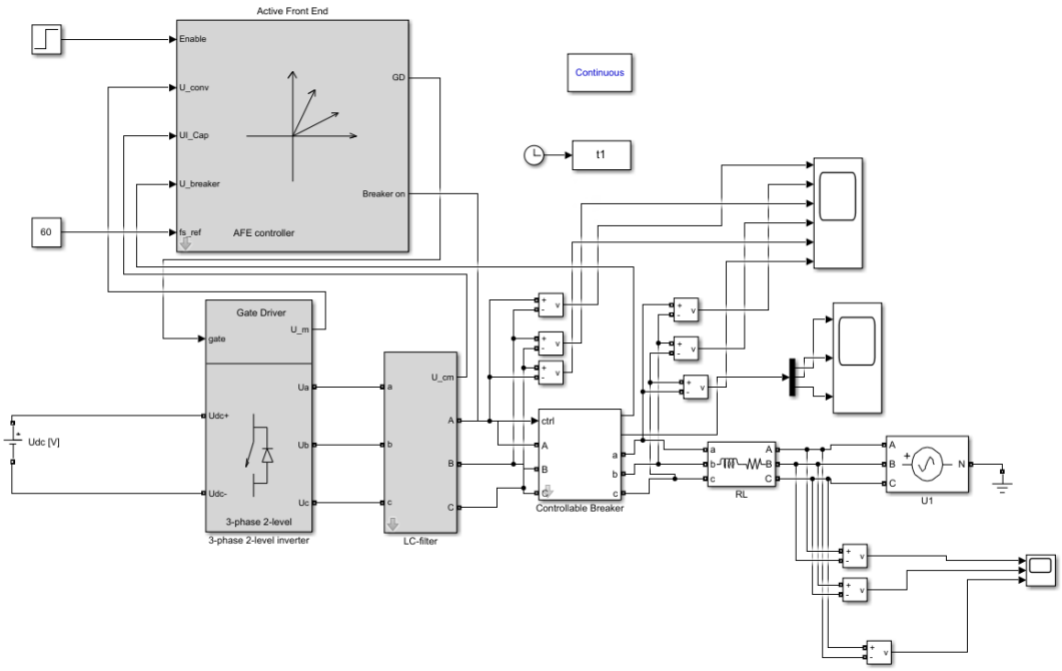

p.u calculations

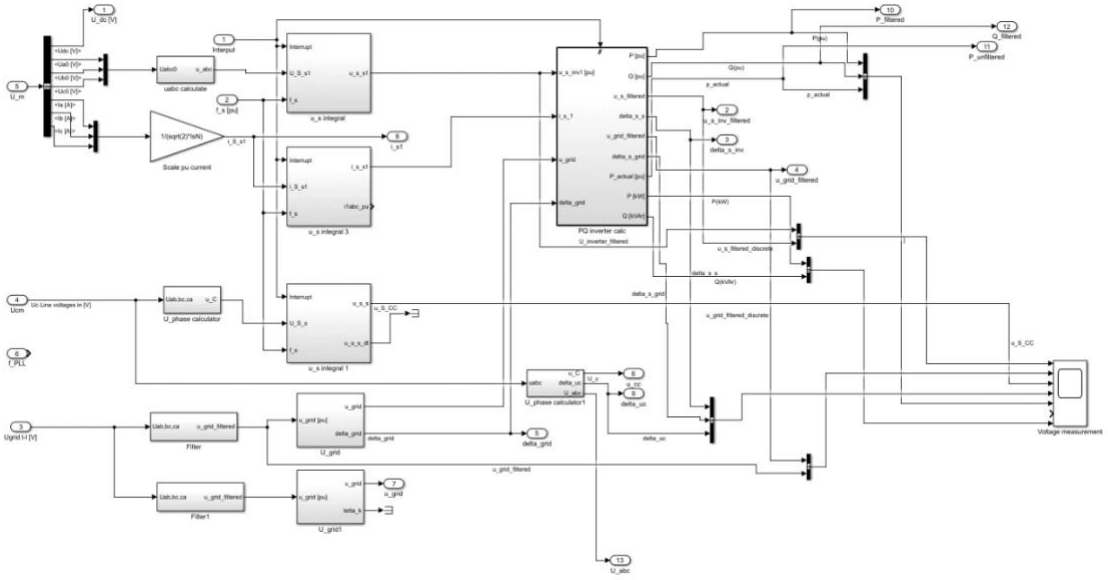

Inverter PQ calculations

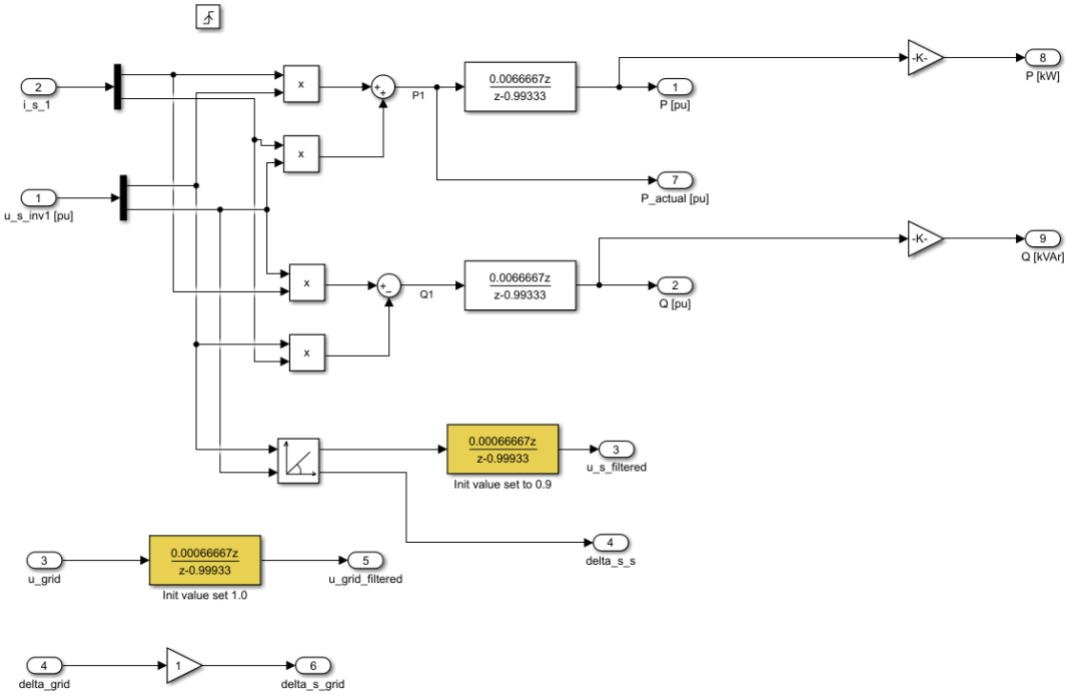

Inner current control loop

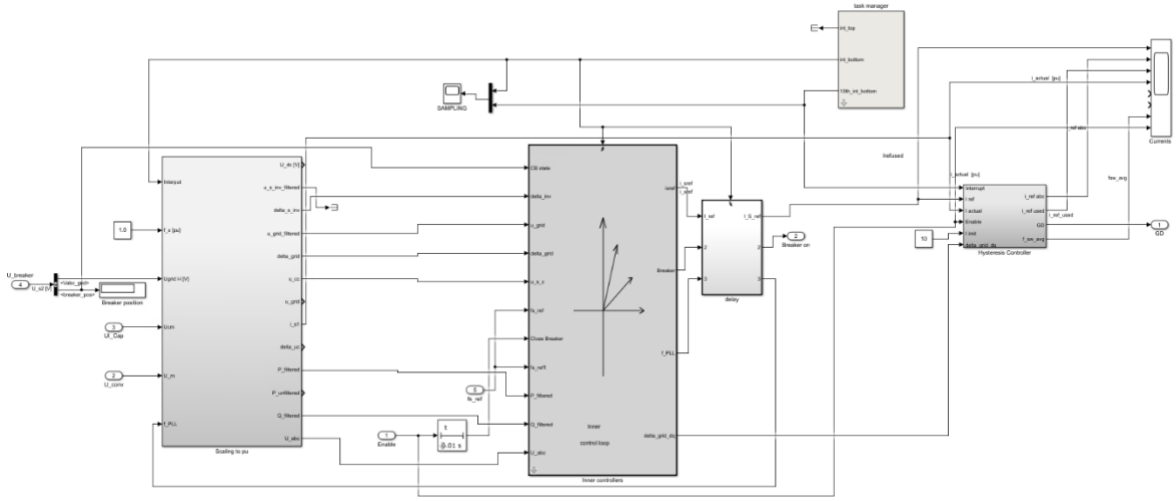

Active damping

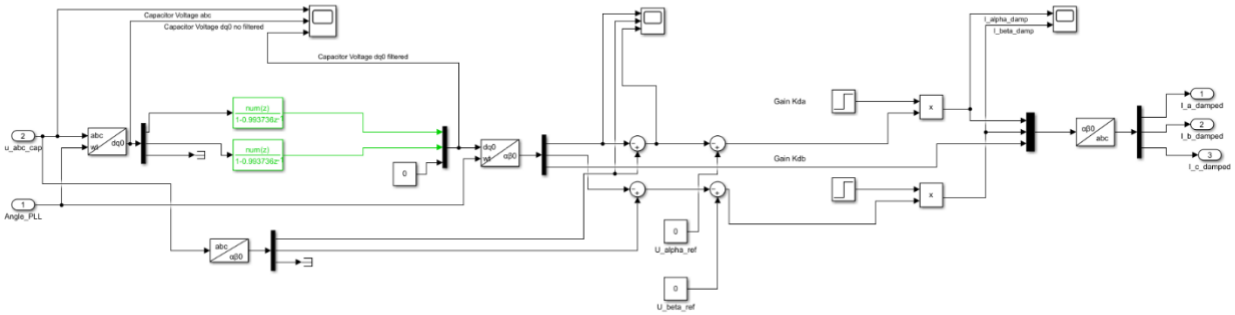

Hysteresis current controller

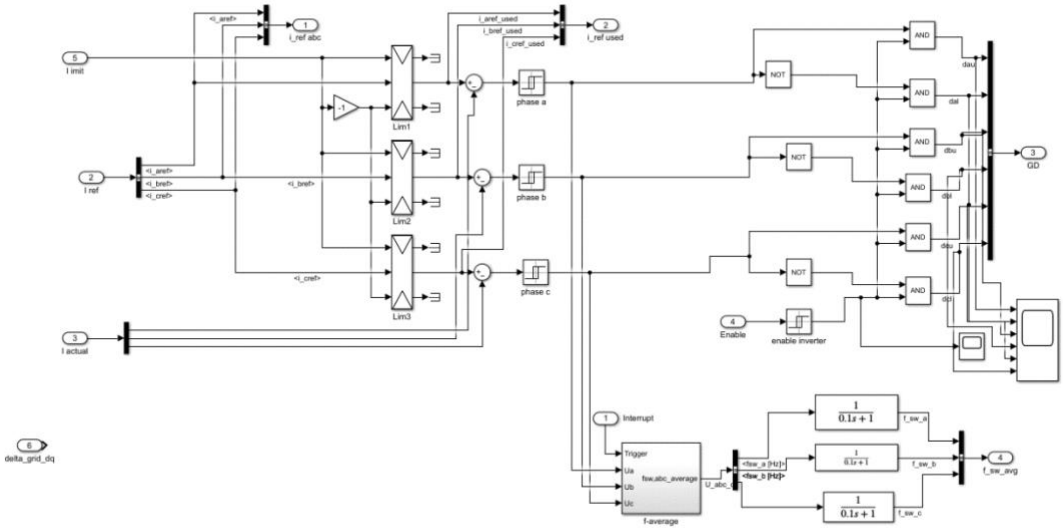

Outer voltage control loop

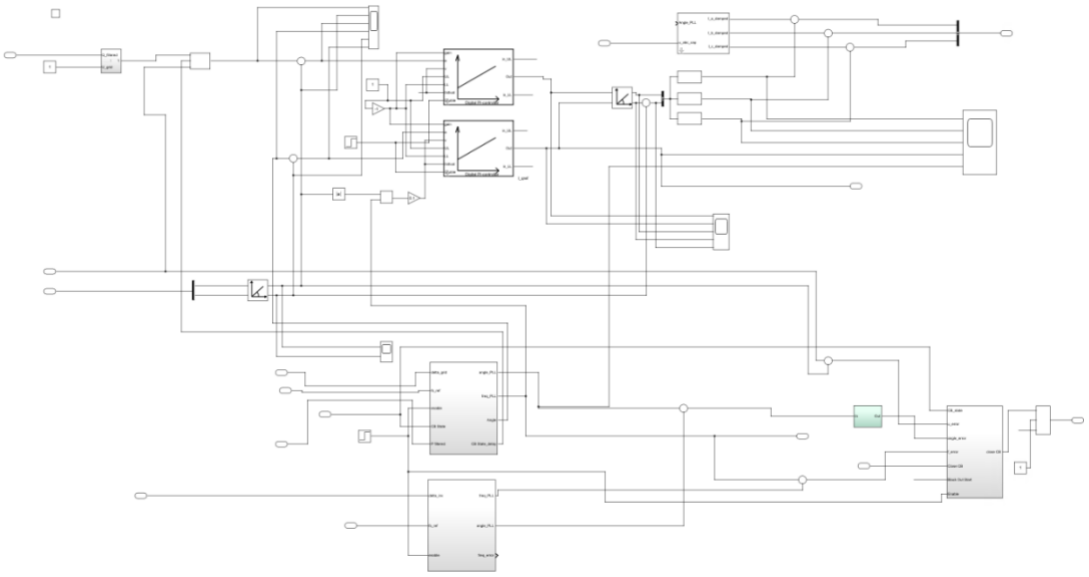

Grid PLL and VISMA synchronization

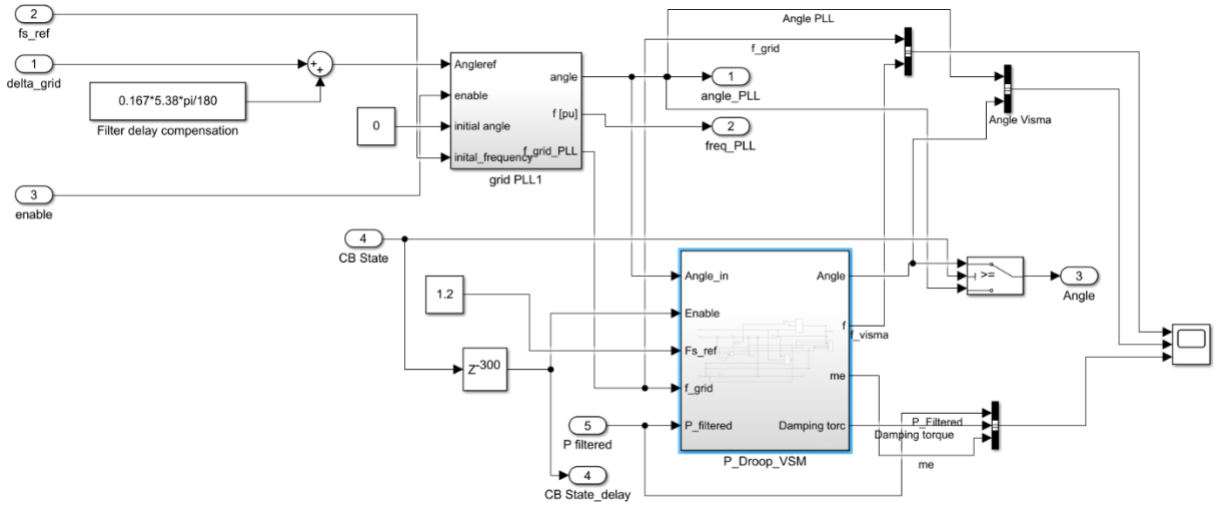

NTNU
Norwegian University of
Science and Technology

MASTER IN RENEWABLE ENERGY IN THE MARINE ENVIRONMENT
REM